ADDITIVELY MANUFACTURED RECONFIGURABLE MICROWAVE COMPONENTS BASED ON MICROFLUIDICS FOR WIRELESS SENSING AND INTERNET-OF-THINGS APPLICATIONS

A Dissertation
Presented to
The Academic Faculty

By

Wenjing Su

In Partial Fulfillment
of the Requirements for the Degree
Doctor of Philosophy in the
School of School of Electrical and Computer Engineering

Georgia Institute of Technology

May 2018

ADDITIVELY MANUFACTURED RECONFIGURABLE MICROWAVE COMPONENTS BASED ON MICROFLUIDICS FOR WIRELESS SENSING AND INTERNET-OF-THINGS APPLICATIONS

Approved by:

Dr. Manos M. Tentzeris, Advisor
School of Electrical and Computer Engineering
Georgia Institute of Technology

Dr. A. Fatih Sarioglu
School of Electrical and Computer Engineering
Georgia Institute of Technology

Dr. Andrew F. Peterson
School of Electrical and Computer Engineering
Georgia Institute of Technology

Dr. Luca Roselli
Department of Engineering
University of Perugia

Dr. Jiang Zhu
Hardware
Google Inc.

Dr. Benjamin S. Cook
Kilby Labs
Texas Instruments

Date Approved: Feburary 16, 2018

To my parents,

Ailing Lu and Xuping Su,

my husband, and my cat,

Meng Xu and Gudongdong,

whose unwavering love, support, and encouragement during the ups and downs made this work possible.

ACKNOWLEDGEMENTS

I would like to express my great gratitude to my advisor, Dr. Tentzeris, for his guidance and support during my Ph.D. journey and for the many invaluable opportunities he provides. Without his support and trust, this work would not have been possible. Dr. Tentzeris has allowed me to grow as a creative researcher through encouraging independent thought, self-guidance, and creativity, which are invaluable skills that can benefit my entire career.

I would like to thank my proposal and defense committee members, Dr. Fatih Sarioglu, Dr. Andrew Peterson, Dr. Luca Roselli from the University of Perugia, Dr. Jiang Zhu from Google, and Dr. Benjamin Cook from Texas Instruments for their thoughtful feedback and suggestions on my thesis. I owe the fruitful results in my work largely to the assistance and friendship of all the ATHENA members and friends, in particular, Dr. Benjamin Cook, Dr. James Cooper, Dr. Chiara Mariotti, Dr. Sangkil Kim, Dr. Jo Bito, Bijan Tehrani, Ryan Bahr, Jimmy Hester, Dr. John Kimionis, Dr. Yunnan Fang, Dr. Taoran Le, Soyeon Jeong, Valentina Palazzi, Syed Abdullah Nauroze, Tong-hong Lin, Shicong Wang, Yepu Cui, Ali Alreshaid, and Xuanke He. I also would like to thank Dr. Jiang Zhu and Dr. Liao Huan at Google for their helpful guidance during my internship there.

Finally, I would like to thank my family for always being there for me during my every step, opening so many doors for me, unwaveringly supporting my decisions, and encouraging me to be a better person.

TABLE OF CONTENTS

Acknowledgments iv

List of Tables ix

List of Figures xi

Summary xix

Chapter 1: Introduction 1

1.1 Research Objectives 1

1.2 Thesis Outline 2

Chapter 2: Review of Microfluidics in Microwave and Its Fabrication Process . 3

2.1 Intersection between Microfluidics and Microwave 3

2.1.1 Lab-on-Chip and Wireless Liquid Sensing 4

2.1.2 Reconfigurable Microwave Components 7

2.2 Fabrication Techniques 9

2.2.1 Additive Manufacturing Techniques 9

2.2.2 Electronics Fabrication 15

2.2.3 Microfluidics Fabrication 18

Chapter 3: Additive Manufacturing Processes for Microfluidics and Electronics 22

3.1 Inkjet Printing 22
3.1.1 Inks 23
3.1.2 First Approach: Printing for Electronics and Bonding Microfluidics 26
3.1.3 Second Approach: Printing Electronics and Molding Microfluidics . 29
3.1.4 Third Approach: Fully Inkjet Printing 33
3.1.5 Fully Printed Paper Microfluidics and Electrical Sensor on Filter Paper 39
3.2 3D Printing 45
3.2.1 FDM Printing 45
3.2.2 SLA Printing 47
3.2.3 DLP Printing 50
3.2.4 Selectively 3D Metalization 52
3.3 Summary 55

Chapter 4: RF Sensors and Reconfigurable Microwave Structures Based on Microfluidics 58

4.1 Coplanar Patch Antenna 58
4.2 Loop Antenna with Balun 60
4.3 Slot Waveguide Antenna 63
4.4 Split Ring Resonator 65
4.5 Dual-spiral Slot Resonator 70
4.6 Dual T-resonator 77
4.7 Microstrip Line and Step Impedance Low Pass Filter 80
4.8 Summary 84

Chapter 5: RFID Platforms for Microfluidic Sensing 86

5.1 RFID-based Comprehensive Sensing Platform: Smart Test Strip 86

5.1.1 System Overview 88

5.1.2 Sensor on Strip 92

5.1.3 Wireless Interrogation 97

5.2 Chipless RFID Configuration 101

5.2.1 Frequency Modulation: Encodable Chipless RFID 101

5.2.2 Phase Modulation: Smart Floating Balls 110

5.3 Summary 120

Chapter 6: Origami Antenna Tree Reconfigurable Antennas Based on Liquid Metal Alloy 122

6.1 Initial Prototype of Helical Antenna 124

6.2 Helical and zigzag antenna 126

6.3 Bow-Tie “Chinese Fan” antenna 131

6.4 Summary 136

Chapter 7: Contribution and Publications 138

7.1 Contribution 138

7.1.1 Fabrication Process 138

7.1.2 Microfluidics Sensing 140

7.1.3 Microfluidics-enabled Reconfigurable Electronics 141

7.2 Publications and Patents 142

7.2.1 Refereed Journals 142

7.2.2 Refereed Conference Proceedings 144

7.2.3 Book Chapter 147

7.2.4 Patents 147

References 161

LIST OF TABLES

2.1 Permittivity of different fluids at around 3 GHz and 300 K[16, 17, 18, 19] . 5

3.1 Inks and its printing /curing conditions 23

3.2 Comparison of demonstrated AM processes for microfluidics electronics in Chapter 3 57

4.1 Dimensions of the proof of concept SSR sensor in Figure 4.16a 72

4.2 Extracted parameters for equivalent parallel RLC circuit model for SSR sensor in Figure 4.16a 73

4.3 Dimensions of microfluidic cavities and channels for dual T-resonator in Figure 4.20b 77

4.4 Dimensions of the two embedded-microfluidics liquid-reconfigurable microstrip line prototypes in Figure 4.22b 83

4.5 Comparison of microfluidics-based microwave structures demonstrated in Chapter 4 85

5.1 Conductivity of different sodium chloride (NaCl) aqueous Solutions for Various Concentrations[124] 96

5.2 Dielectric constant of air and three organic fluids at 1 kHz and room temperature[127] 97

5.3 “Code” frequencies for every bit for the proof-of-concept encodable chipless RFID in Figure 5.28 106

6.1 Parameters for the feed line for the helical antenna in Figure 6.1 125

6.2 Critical angle α and height of each segment for the origami zipper tube in Figure 6.4 130

LIST OF FIGURES

2.1 Permittivity-based microwave sensing mechanism. 4

2.2 Breakdown percentages of the industrial sectors using AM. Reprint from [41]. 10

2.3 Working principles of (a) Stereolithography (SLA), (b) digital light processing (DLP) and (c) fused deposition modeling (FDM). Reprint from [42]. (d) Stucture of piezoelectric inkjet printer head. Reprint from [43]. . . 11

2.4 An example shows the influence of polymer molecular weight and concentration on the breakup of a fluid jet. Solvent: (a) glycerol/water (b) 0.3% 100 000 poly(ethylene oxide) (c) 0.1% 300 000 poly(ethylene oxide) (d) 0.05% 1 000 000 poly(ethylene oxide) (e) 0.043% 5 000 000 poly(ethylene oxide). Reprint from [45]. 13

2.5 The working principles of coffee ring effect. Reprint from [47]. 13

2.6 Step-by-step process of (a) single side printed circuit board (PCB) (picture found at [52]), (b) photolithography with lift off process or etch process (picture found at [53]). 16

2.7 Cost and volume comparison for common Lab-on-A-Chip fabrication technologies. Reprint from [58]. 19

2.8 Step-by-step process of (a) soft lithography for microfluidics devices (reprint from [4]), (b) paper microfluidics with photolithography and wax printing (reprint from [59]). 20

3.1 Performance of inkjet-printed SU-8. 25

3.2 Smallest features of inkjet-printed PMMA. (a, b) Photos of “single-drop” test. (c) Measured average heights and widths with error bars of the printed PMMA line prototypes in (a, b). 27

3.3 Performance of inkjet-printed PMMA. (a) Average height and error bar of 1 to 15 printed layers. (b) Cross-sectional profile of the printed PMMA lines in (a). 28

3.4 Step-by-step fabrication process utilized inkjet printed conductor for electronics and polymer for bonding microfluidics. 28

3.5 Step-by-step fabrication process utilized inkjet printed conductor for electronics and polymer for molding microfluidics. 30

3.6 (a) A photo in the cross section view of a microfluidic device by the inkjet printing molding method. (b) A photo of the fabricated prototype with the PDMS sheet (microfluidic part) partially peeled off from the PET sheet (electrical part), to illustrate the "peel-and-replace" capability. (c) Tests of the possible dimensions of the proposed fabrication process.The dots represent successful individual tests. The line in the graph shows the lower limit of the successfully fabricated aspect ratio. The small inserted photograph in the figure gives the reader a glance of the testing matrix. 32

3.7 Step-by-step fabrication process of fully inkjet printed microfluidics and electronics. 34

3.8 SEM images of fully inkjet printed microfluidics. The debris particles shown in the SEM images very likely were SU-8 polymer. 35

3.9 Sketch and prototype of a fully inkjet-printed 3D microfluidics structure. . . 36

3.10 Examples of fully inkjet-printed microfluidics structures. 38

3.11 Inkjet-printed conductive layers on paper. 40

3.12 (a) A drawing of the cross-section view of two types of microfluidics and their transition. (b) Different numbers of inkjet-printed layers of SU-8 rectangular rings for paper-microfluidics. 42

3.13 (a) Two microstrip lines on filter paper to characterize the substrate. (b) A T-resonator working at 2.4 GHz utilized for filter paper calibration. (c) Measured permittivity vs frequency using the two methods in (a) and (b). . . 44

3.14 Photo of a FDM 3D printed microfluidics-enabled helical antenna (a) in a FDM 3D printer and (b) in a bottom view while filled with red-dyed water. . 46

3.15 (a, b) 2 microstrip lines (a) and a T-resonator (b) for FLGR02 material characterization. (c) Relative permittivity and loss tangent characterization results up to 8 GHz. 48

3.16 Photo of the twisted SIW in various states: (a) original (120° twisted); (b) flat (0° twisted); (c) 180° twisted. 49

3.17 Photo of the wavy SIW in various states: (a) original (6.71 cm length); (b) compress (4 cm length); (c) stretched (9 cm length). 50

3.18 Photos of (a) a FDM 3D printed microfluidics mixer, (b) a zigzag channel for zigzag antenna in printing, and (c) the DLP printer used. 51

3.19 Selective 2.5D metallization process with a arbitrary 3D object in a cross-section view. 54

3.20 3D printed comformal stamp. Photos of (a) the stamp for the spherical patch antennas, (b) the stamp for a power splitter utilized in the antenna array, and (c) stamping both stamps for a composite antenna array topology. 56

4.1 A photo (a) and a drawing (b) of the microfluidics-based tunable CPA along with measured and simulated the return loss in (c). 59

4.2 Simulated and measured radiation pattern of the microfluidics-based tunable CPA on E plane (a) and H plane (b). 60

4.3 A photo (a) and a drawing (b) of the microfluidics-based tunable loop antenna with a balun along with measured and simulated the return loss in (c). 61

4.4 (a) The real part and imaginary part of impedance of the microfluidics-based tunable loop antenna in simulation for empty and water-filled channel. (b) Phase difference between two branches of balun in simulation for empty and water-filled channel. 62

4.5 Simulated E plane (a) and H plane (b) radiation patterns of the microfluidics-based tunable CPA for the empty channel and the water-filled channel. . . . 63

4.6 Photo of 3D printed microfluidics sensors. 64

4.7 Diagonal view of 3D printed air core SIW which is cut in half to show the cross-section of the SIW. 64

4.8 S11 of the antenna sensor when different fluids or air filled in channel. . . . 65

4.9 The relation between the resonant frequency shift of the sensor and the permittivity value of the material filled in the channel. The line shows the simulation result, and the triangles are the measurement results for empty, ethanol-filled, and water-filled channels. 66

4.10 Maximum gain of the slot waveguide antenna for the empty channel and the water-filled channel. Due to the dielectric loss of water and impedance mismatching, the maximum gain for a water-filled microfluidics channel is lower than that for an empty channel. 66

4.11 A photo (a) and a drawing (b) of the microfluidics-based tunable SRR bandstop filter. 67

4.12 (a) the equivalent circuit of microfluidics-based tunable SRR. (b) Sensitivity change with different slot in simulation. 68

4.13 (a) Measured and simulated insertion loss (IL) of the SRR for different fluids pumped into the channel. (b) Resonance frequency shift (in percentage) of the SRR due to different fluids in the channel. 69

4.14 Measured resonance frequency shift (in percentage) due to temperature change with empty and water-filled channels for the SRR sensor. 70

4.15 (a) A photo of the fabricated microfluidic dual-spiral slot resonator sensor prototype. (b) A photo demonstrating the attachment of the sensor prototype on the wrist. 71

4.16 (a) A drawing of the microfluidics-based tunable dual-spiral slot bandstop filter. (d) The equivalent circuit of a dual-spiral slot resonator. 72

4.17 Measured and simulated resonant frequency change for fluids with different relative permittivity values: (a) four different pure liquid and air. (b) water-glycerol mixture with different mixing ratio. 74

4.18 Measured and simulated values of the resonant frequency shift for different relative permittivity fluids in the channel of the slot resonator, demonstrating a logarithmic linearity of the sensor prototype. 75

4.19 Photos of mesurement setup for flat sensor (a) and bent sensor (b) along with the measurement result in (c). 76

4.20 A photo (a) and a drawing (b) of the microfluidics-based tunable dual T-resonator bandstop filter along with measured and simulated the return loss in (c) with various fluid in channel. 78

4.21 Measured and simulated resonant frequency change for fluids with different relative permittivity values in only one of the two sensors. (a) Fluids are in sensor 1 while sensor 2 stays empty. (b) Fluids are in sensor 2 while sensor 1 stays empty. 79

4.22 Fully inkjet-printed microfluidics sensors. 81

4.23 Measured and simulated results of the sensors in Figure 4.22. 82

5.1 A block diagram of the smart test strips system-level operation principle. . . 89

5.2 A photo of fabricated smart test strip prototypes working at (a) wireless and (b) near-field communication (NFC) frequencies. 90

5.3 (a) A photo of multiple smart electrical sensors integrated on pH test strips along with an inserted photo (right) of one pH smart strip tested by vinegar confirming the unaffected good performance of the chemical sensor. (b) A drawing of the cross-section view of the smart test strip channel topology. . 91

5.4 (a) A photo of a printed sensor prototype compared to an 1-cent coin. (b) Magnified view of the interdigitated electrode (IDE) structure in the dashed square in (a). (c) Equivalent circuit of the IDE sensors. 93

5.5 (a) Measurement setup for the microfluidic sensor testing. (b) Simulated and measured the average resistance of the sensor for filling liquids with different concentration (resistivity), along with the error bars showing the standard deviations of 20 replicas that were measured ten times each. (c) Simulated and measured average capacitance of the sensor for filling liquids with different dielectric constants, along with the error bars showing the standard deviations of 20 replicas that were measured ten times each. 95

5.6 (a) The schematic of the external circuit to the RFID chip. (b) A photo of the measurement setup of a smart test strip with an NFC RFID reader. . . . 98

5.7 Calculated wireless reading of the smart test strip prototype in an NFC chip configuration along with measured values for sodium chloride aqueous solutions of different concentrations, along with the error bars showing the standard deviations of measuring the sample for 20 times. 99

5.8 Inkjet-printed meander-line dipole antenna on filter paper for wireless smart test strips. 100

5.9 Simulated and measured return loss (S11) of the inkjet-printed dipole antenna on filter paper. 100

5.10 Block diagram of the microfluidics-encodable chipless RFID tag operation principle. 102

5.11 Photo of a prototype of all-inkjet-printed microfluidics-encoded chipless RFID tag including the receiving and the transmitting ultrawideband antennas. 103

5.12 A photo (a) and a drawing (b) of the microfluidics-based tunable chipless RFID encoding module along with two photos of bending in two directions around a dollar coin (13-mm-radius) and a quarter dollar coin (12-mm-radius) in (c). 104

5.13 (a) A side view of how to encode the RFID by pressing the "button". (b) A photo of a realization of the above mentioned method by covering the prototype with a Polydimethylsiloxane (PDMS) sheet and pressing the "button" with a cotton swab. 104

5.14 Simulated and measured insertion loss (a) and phase delay (b) values of the prototype for code "000" and "111" configurations in flat or bent for a 30 mm radius. 105

5.15 Measured the insertion loss values of the prototype with the middle microfluidic channel filled by water glycerol mixtures while other two channels left empty. 106

5.16 Insertion loss of the prototype for various 3-bit code configurations at the coding frequencies of the (a) lowest bit, (b) middle bit and (c) highest bit. . 107

5.17 Photos of fabricated UWB monopole antennas for chipless RFID. (a) Monopole antenna 1. (b) Monopole antenna 2. 108

5.18 The simulated and measured values of S11 of the two ultrabroadband antennas of the chipless tag. 109

5.19 The simulated and measured values of the gain of the two ultrabroadband antennas of the chipless tag in the maximum radiation direction. 110

5.20 Co-polarized and cross-polarized radiation pattern of at 4 GHz, 5 GHz, 6 GHz and 7 GHz. Solid line stands for measured co-polarized radiation pattern; dashed for simulated co-polarized; dash dot for measured cross-polarized; and dot for simulated cross-polarized. 111

5.21 A graph of the smart floating ball and a cross-section photo of a proof-of-concept prototype. 112

5.22 Photos of fabricated prototypes of (a) four spherical patch antennas, (b) a 4×1 patch array around the top hemisphere interconnected with a power splitter on the bottom plane, and (c) a smart floating ball based on the spherical patch antennas floating on water. 113

5.23 Performance of the four antennas on the sphere. Measured and simulated values in air and simulated values in water for (a) return loss of the antenna and coupling between antennas, (b) gain. 114

5.24 Performance of the four antennas on the sphere. Measured and simulated values in air and simulated values in water for normalized radiation pattern (a) in phi=90° and (b) in theta=90°. 115

5.25 Performance of the antenna array on the sphere. Measured and simulated values in air and simulated values in water for (a) return loss of the antenna and coupling between antennas, (b) gain. 116

5.26 Performance of the antenna array on the sphere. Measured and simulated values in air and simulated values in water for normalized radiation pattern (a) in phi=90° and (b) in theta=90°. 117

5.27 (a) A photo of the phase delay line liquid sensor with red dyed water inside the 3D printed microfluidic channel. (b) A cross-section view of the phase delay microstrip line sensor. (c) Measured and simulated phase shift for different permittivity liquids inside the channel. 118

5.28 Circuit schematic of the chipless RFID. 119

6.1 Geometry (a) and photograph of a fabricated prototype (b) of the proposed helical antenna. 124

6.2 Measured and simulated gain value of the helical antenna with different turns of helix filled with LMA. 126

6.3 (a) Measured and simulated return loss value and (b) simulated radiation pattern (Unit: dB) of the helical antenna with different numbers of turns of helix filled with LMA. 127

6.4 A photo of the 3D Printed origami antenna tree. The zigzag antenna and its matching circuit are marked in blue while helical antenna and its matching circuit in yellow. 128

6.5 Top view (a) and side view (b) of the 3D model of the proposed "tree" with dimensions. Certain transparency was added to assist understanding of the structure. 129

6.6 (a) Pattern and parameters of a Miura-ori cell, which is the base for the zipper tube. Reprint from [144]. (b) A photo of a 3D printed zipper-tube in compression. 129

6.7 Measured and simulated S11 of the zigzag antenna (a) and the helical antenna (b) under different folding states. The fabricated wall of microfluidics channel is thinner than that in the 3D model which causes the simulated resonant frequencies to be lower than the measured ones. 132

6.8 Measurement setup for the radiation pattern of the zigzag antenna. A horn antenna and roatation station were used to measure the zigzag antenna. . . . 133

6.9 Measured and simulated normalized radiation pattern of the compressed (a) and of the original (b) zigzag antenna at 3 GHz. 133

6.10 Measured and simulated normalized radiation pattern of the compressed (a) and of the original (b) helical antenna at 5 GHz. 134

6.11 Geometry (a) and photographs of a prototype (b, c) of the proposed "Chinese fan" bow-tie origami antenna. In (a), the red part is the 3D printed origami structure and the blue part stands for the microfluidic channel to contain LMA. In (b), the right fan is in its original state with a 80 degree apex angle and the left fan is compressed by two fingers to achieved a 30 degree apex angle. In (c), the antenna is folded up to show the flexibility. . . 135

6.12 S11 of the bowtie antenna for various apex angles. 136

6.13 The slope, variance of the real part and imaginary part of the antenna input impedance per frequency (Ω/MHz), at the frequency of zero imaginary impedance for various apex angles. 136

SUMMARY

My Ph.D. research interfaces additive manufacturing and microfluidics with microwave and radio frequency (RF) electronics to provide a novel low-cost flexible and reconfigurable solution for Internet-of-Things (IoT). Microfluidics, an emerging technology which allows the precise control of an extremely small amount of liquid with tiny channels, can be used in IoT applications to achieve Lab-on-Chip (LoC) functionality and an extraordinary reconfigurability. Microwave structure is very sensitive to the surrounding environment and thus is excellent to be sensors, while passive radio frequency identification (RFID) provides low-cost zero-power solution to wireless liquid sensing. This work has developed various proof-of-concept disposable wireless liquid sensors and RFID-based sensing platforms for LoC applications. To realize an excellent reconfigurability low-costly and compactly, this research also has studied new reconfigurable RF integration topologies by integrating microfluidic channels and dielectric or conducting liquids. In order to significantly decrease the production time and cost, and thus to enhance the ubiquitous smart items, this research studied additive manufacturing (AM) in IoT applications. This research has been exploring the possibility of replacing the conventional electronics and microfluidics fabrication methods with cost-effective additive manufacturing methods such as inkjet-printing and 3D printing. This work presents first-of-its-kind, cost-effective, rapid, low-temperature, and environmental-friendly AM fabrication methods for various reconfigurable antennas or microwave components, wearable sensors, and sensing platforms. In summary, this research focuses on utilizing new AM fabrication techniques and novel microfluidics topologies to provide a low-cost, flexible, and scalable solution for wireless sensing and IoT applications.

CHAPTER 1
INTRODUCTION

1.1 Research Objectives

Internet-of-Things (IoT) and smart objects under this concept, such as smart environment and smart health, have drawn a lot of attention from the research community and the industry recently and have started utilizing an amazing variety of emerging technologies. The objective of the proposed research is to interface additive manufacturing (AM) and microfluidics with microwave and radio frequency (RF) electronics to provide a novel low-cost flexible and reconfigurable solution for IoT.

Microfluidics, an emerging technology which allows the precise control of a small amount of liquid with small fluidic channels, can be used in IoT applications to achieve Lab-on-Chip (LoC) functionality and extraordinary reconfigurability. On the one hand, this work has developed various proof-of-concept disposable microwave liquid sensors and sensing platforms for LoC applications. On the other hand, new reconfigurable RF integration topologies by integrating microfluidic channels and dielectric or conducting liquids are studied for reconfigurability at low-cost and compact size.

One of the critical requirements of ubiquitous smart items is to enable on-demand production while significantly reducing the production time and cost. Therefore, my research applies additive manufacturing in IoT by exploring the possibility of replacing the conventional electronics and microfluidics fabrication methods with cost-effective on-demand additive manufacturing methods such as inkjet-printing and 3D printing, which results in the first-of-its-kind, cost-effective, rapid, low-temperature, and environmental-friendly AM fabrication methods for various reconfigurable antennas or microwave components, wearable sensors, and sensing platforms.

In summary, this research focuses on utilizing new AM fabrication techniques and novel microfluidics-based microwave topologies to provide a low-cost, flexible, and scalable solution for wireless sensing and IoT applications.

1.2 Thesis Outline

This thesis is organized in the following way:

1. Chapter 2 provides background and comparison to this work by introducing the microfluidics-based microwave structures in prior art and the state-of-art fabrication process for both electronics and microfluidics.

2. Chapter 3 illustrates novel additive manufacturing approaches for electronic devices with microfluidics structures, including inkjet printing and 3D printing.

3. Chapter 4 presents the design and performance of various microwave liquid sensors for smart health and IoT applications based on microfluidics structures along with antennas integrated with microfluidics structures featuring reconfigurability in radiating frequency, gain, and radiation pattern.

4. Chapter 5 discusses the wireless microfluidics-based liquid sensing platforms that utilize RFID and chipless RFID configurations.

5. Chapter 6 demonstrates a reconfigurable antenna integration topology, the origami antenna tree with liquid metal.

CHAPTER 2
REVIEW OF MICROFLUIDICS IN MICROWAVE AND ITS FABRICATION PROCESS

This chapter provides a background of the whole Ph.D. thesis research by firstly introducing the microfluidics-based microwave structures in prior art, usually in the form of liquid sensor or reconfigurable components, and then the state-of-art of both conventional methods and novel AM fabrication processes for microwave electronics and microfluidics.

2.1 Intersection between Microfluidics and Microwave

As a tool to manipulate tiny quantities of liquids, microfluidics technology has been widely used in biomedical sensing, chemical assay, manufacturing control, and other lab-on-chip applications since early 1990s[1, 2]. A lot of research effort can be found in applying microfluidics in chemical/ biological sensing, cell culture [3, 4], drug delivery[5], material synthesis[6], microfabrication[7], and optics[8], because the small liquid amount leads to a reduced cost, faster assays, compact size, less waste, higher data quality, and easy automation. While microfluidics researches on fluid flows and design of components such as conduits, valves, pumps, mixers, interconnects on micrometer length scales, microwave involves electromagnetic wave with a wavelength ranging from meters to millimeters. Due to their ”micro”/compact nature, microwave and microfluidics have been combined recently, for liquid sensing and reconfigurable RF electronics applications. This section provides the background of intersection between microfluidics and microwave in two aspects: liquid sensors and reconfigurable components.

2.1.1 Lab-on-Chip and Wireless Liquid Sensing

Lab-on-chip (LoC) and wireless liquid sensing aim to minimize and simplify the process of liquid analysis to improve the practice of various industries such as distributed healthcare, food quality monitoring, and environmental hazard detection. To fulfill the growing needs of portable and low-cost liquid sensors for liquid analysis and monitoring, various RF and microwave structures have been utilized to sense the electrical properties of the test liquids, accurately, labels-freely, noninvasively, and without contact. With these structures, the liquid content can be detected without any markers or modification; thus, this approach effectively avoids contamination to the samples and saves the testers' time as well as effort. Moreover, as the sensing information is read with a RF/microwave signal which is ready to be sent out, real-time monitoring and wireless sensing can be easily realized with RF/microwave sensors. Furthermore, both microfluidics and microwave structures feature a minuscule approach that excellently fit the concept of Lab-on-Chip: microfluidics ensure the small test volume needed, and microwave structures are in the scale of wavelength (from meters to millimeters).

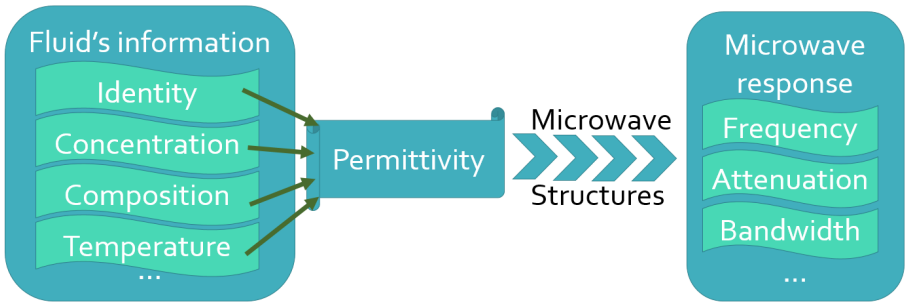

Figure 2.1: Permittivity-based microwave sensing mechanism.

Permittivity-based sensing

Permittivity is one of the most common parameters used in liquid sensing. In the natural environment, liquids have a wide permittivity distribution at microwave frequencies as shown in Table. 2.1. Moreover, by varying mixing ratios, mixtures of two or more fluids can feature a wide range of continuous permittivity change[9, 10]. Similarly, if any solute

is added to the solvent, the permittivity of the solution changes depending on the concentration of the solute[11]. For example, fat content in milk[12] and fermentation of wines[13] can be easily monitored by the permittivity value; contamination of groundwater can be detected by an abnormal imaginary part of complex permittivity value[14]. Furthermore, for various temperature, liquids may have different permittivity values [15]. Thus, if a device is capable of detecting small changes in permittivity values of a liquid solution and its environment, it may deduce a significant amount of information about it.

Table 2.1: Permittivity of different fluids at around 3 GHz and 300 K[16, 17, 18, 19]

Name	Permittivity	
	Real part	Imaginary Part
Cotton oil	2.64	0.175
Hexanol	3	1
Glycerol	4	0.4
Ethanol	6	7
Water	73	8

Microwave structures are sensitive to the permittivity of the dielectric liquids, as phase velocity (V_p) depends on relative permittivity (ϵ_r):

$$V_p = \frac{1}{\sqrt{\mu_0 \mu_r \epsilon_0 \epsilon_r}} \tag{2.1}$$

where μ_o and ϵ_0 are permeability and permittivity of vacuum while μ_r is the relative permeability. In Maxwell's equations, the displacement field (D) is strongly related to the permittivity of the material:

$$D = \epsilon_0 \epsilon_r E \tag{2.2}$$

Thus, in sensor design, the microfluidic channel is favorable to be in a strong E-field to maximize the sensitivity. In the perspective of equivalent circuits of microwave structures, the capacitors can be tuned by changing relative permittivity (ϵ_r) values. For example, in a parallel-plate model:

$$C = \frac{\epsilon_0 \epsilon_r A}{d} \tag{2.3}$$

where A is the plate area and d is the distance between the two plates.

Broadband Permittivity Spectroscopy

Broadband permittivity spectroscopy is usually used in characterizing the material's complex permittivity value which can bring a rich set of information about the liquid over an extensive frequency range. These methods usually use very simple microwave structure such as a coplanar waveguide (CPW) line [20, 21]. However, the two port complex S-parameters need to be measured, which means expensive measurement devices and time-consuming data processing are required, bringing troubles to the real-time monitoring. Therefore, broadband permittivity spectroscopy is mostly used in material characterization instead of sensing applications.

Resonators in sensing

Different kinds of resonators have been applied in characterizing or sensing the permittivity of liquids, because the resonant frequency, peak attenuation, and bandwidth of resonators can adequately reflect the complex permittivity of the materials. Compared to the broadband permittivity spectroscopy method, the resonant frequency shift and the change of Q factor are much easier to observe, and the relation between complex permittivity and these parameters is more straight-forward. For a resonator, the resonant frequency is decided by the effective inductance (L_{eff}) and effective capacitance (C_{eff}) of the equivalent circuit:

$$f = \frac{1}{\sqrt{L_{eff}C_{eff}}} \tag{2.4}$$

Combining with equation 2.3, it's obvious that an increase in relative permittivity will lead to an increase in capacitance and a decrease in resonant frequency. Similarly, a larger imaginary permittivity or loss tangent means the material is lossier which leads to an increased bandwidth (or decreased Q factor) and a smaller maximum attenuation. One thing to mention is that as a increased value of the real part of the complex permittivity leads to a increase in the intensity of the E-field as shown in equation 2.2, so the Q factor increases in this situation. Consequently, the variation in Q factor should be considered comprehen-

sively.

Dielectric cavity resonators and waveguide resonators have been well researched due to their straight-forward designs[22, 23]. But they feature a large size and require a significant amount of liquid, which conflicts with the principle of LoC. Planer resonators, such as split ring resonators (SRR) [24] and stub resonators [25], have been used in microwave sensing recently, which feature much more compact sizes and more accurate detection with a small amount of liquid. Therefore, the planer resonator fits LoC and wireless sensing better.

2.1.2 Reconfigurable Microwave Components

Microwave electronics are key elements in the wireless communication systems based on the electromangnetic wave. As people daily life are highly rely on wireless communication, such as cell phones, microwave components and systems with better performance and lower cost can significantly improve people life quality and shorten the distance between individuals. Base on that, reconfigurable microwave passive components have been investigated heavily recently as they can efficiently adapt to the dynamic environment or varying requirements so that they reduce the number of components needed as well as the area used.

Regular RF-MEMS

Radio Frequency Micro-Electro-Mechanical Systems (RF-MEMS) were first introduced less than 20 years ago but have gained popularity very fast and have already been under a spotlight [26]. Nowadays, most tunable RF designs are based on MEMS devices such as RF-MEMS varactors and RF-MEMS switches[27, 28]. MEMS switches are very promising devices in reconfigurable RF circuits such as antennas [27], filters [28], and metamaterials [29], as they can enable better performance regarding loss, isolation, linearity, power consumption, and compatibility with integrated circuits.

However, MEMS have a fatal “flaw” that they are costly due to the cleanroom-required high-cost fabrication process. MEMS usually feature a minimal size (e.g., nanometer to

micrometer) and can only operate appropriately within nano- or micro- scale. These tiny features in the MEMS require an ultra-high-resolution dust-free fabrication. Silicon-based photolithography, which is known for its high performance and high cost, is still the primary fabrication method to MEMS devices. Besides the cost, the power handling capability of traditional MEMS devices is limited. Moreover, because rigid materials, such as silicon, are used in most cases, these devices are not suitable for flexible design in conformal or wearable applications. Therefore, researchers have been developing various novel reconfigurable components, such as those based on liquid and microfluidics [30], for low-cost IoT applications.

Based on conductive liquid

Liquid metal alloy (LMA) has been used in reconfigurable microwave structures due to its excellent flexibility and its fluid nature. The most popular LMA is Eutectic Gallium-Indium (EGaIn), a non-poison alloy with 75%wt Gallium and 25%wt Indium, which features a 15.5 °C melting point, and a $29.4\times10^{-6}\Omega$·cm resistivity that enables high-performance electronic designs [31]. The bulk viscosity of EGaIn is 1.9910 mPa*s (twice of water, one 4000th of ketchup), which enables trouble-less flowing in the channels.

Unlike all solid materials, liquid metal is stretchable with literally no failure point due to its liquid nature, which is only limited by the channel's / container's stretchability. Thus, LMA devices enable a "never-fail" bending and a constant self-healing even if cracks occur under extreme bending conditions. Based on microfluidics channel and the stretchable property of LMA, stretchable and flexible reconfigurable antennas are reported [32, 33, 34], in which the physical length of the LMA conductor can be tuned by stretching/releasing the structure.

Another approach is adding a channel for the LMA to a specific microwave structure to shorten the original circuit, to couple the EM field, or to change the electrical length [35, 36, 37].One most considerable challenges is that Gallium quickly oxidizes when exposed to air, an effect that could prevent the proper flow of LMA. To dissolve/avoid the oxidation skin of

the EGaIn, a sodium hydroxide (NaOH) solution can be circulated inside the microfluidic channel before it is filling with EGaIn.

Based on dielectric liquid

Besides conductive liquid, dielectric liquids are also used in tuning the microwave devices with two primary approaches. Firstly, as discussed in section 2.1.1, the working frequencies of the microwave structure depend on the dielectric constant of the surrounding area. Therefore, one can build a reconfigurable component by loading/unloading dielectric liquid with different permittivity in a microfluidic channel on a microwave component [38]. Secondly, similar to using LMA for EM coupling, small metal plates/cylinders can be inserted into microfluidic channels and moved by dielectric liquid flows, which enables tuning of the coupling effect [39, 40].

2.2 Fabrication Techniques

To realize the RF/microwave structures for the Internet-of-Things applications as discussed in the former section, various fabrication techniques have been developed to realize reliable and cost-effective manufacturing of those structures.

2.2.1 Additive Manufacturing Techniques

Additive manufacturing (AM) has been massively expanding in industry, as shown in Figure 2.2, and in academia[41], due to its cost-, time-, and effort-effectiveness especially in prototyping three-dimensional (3D) objects. Traditional (subtractive) manufacturing techniques, such as photolithography, deposit a uniform layer of materials and selectively remove part of it. AM techniques, on the other side, deposit patterned material, and no removal is needed. There are countless approaches of AM, and each has its advantages and drawbacks. But the foundational operation principle of all AM techniques is a layer-by-layer selectively deposition and solidification of material, thus here four of the most widely used low-cost AM processes are introduced and classified with the deposition and

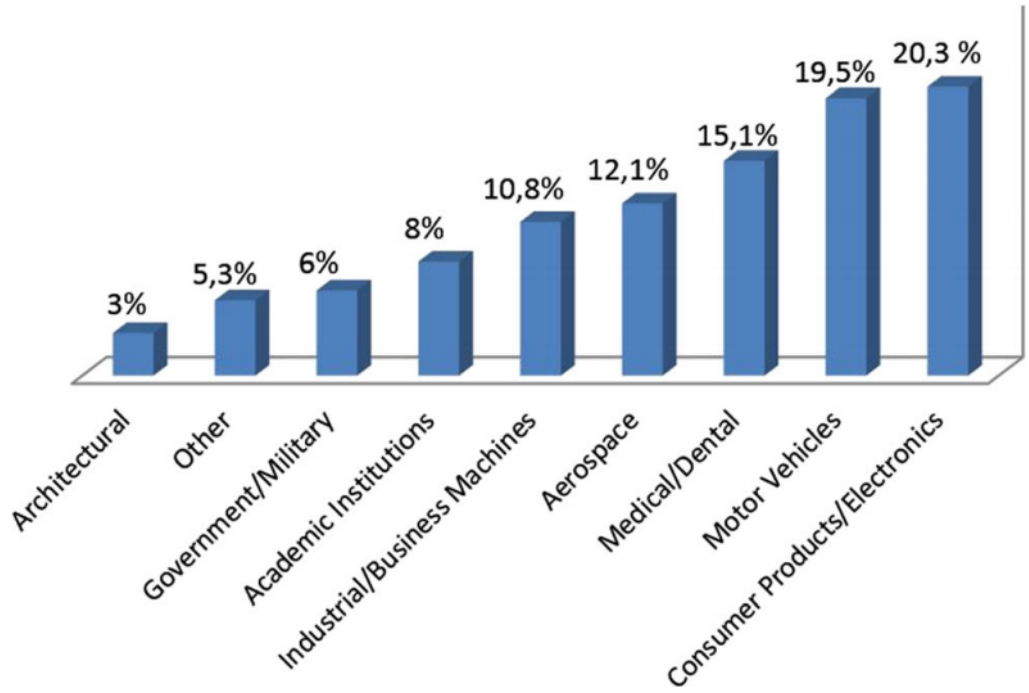

Figure 2.2: Breakdown percentages of the industrial sectors using AM. Reprint from [41].

solidification approaches.

Based on UV curing

Stereolithography (SLA) and digital light processing (DLP) are two techniques using a photosensitive polymer which can be cross-linked and solidified with ultraviolet (UV) exposure. The two process are similar but use different UV sources. They both use a tank of liquid photosensitive monomer resin with a build platform inside of the tank. SLA uses a UV laser beam and a mirror to locally cure the photosensitive polymer, as shown in Figure 2.3a. The laser beam is moving as the mirror rotates and the pattern is drawn with multiple line paths. Figure 2.3b shows that DLP, on the other side, projects a matrix of UV light to the resin and patterns the entire layer simultaneously. As a consequence, DLP usually has a higher printing speed and a lower resolution, compared to SLA.

Based on extrusion

Fused deposition modeling (FDM) is one of the oldest and most commercialized 3D printing techniques. An FDM printer utilizes a movable heated nozzle to deposit molten

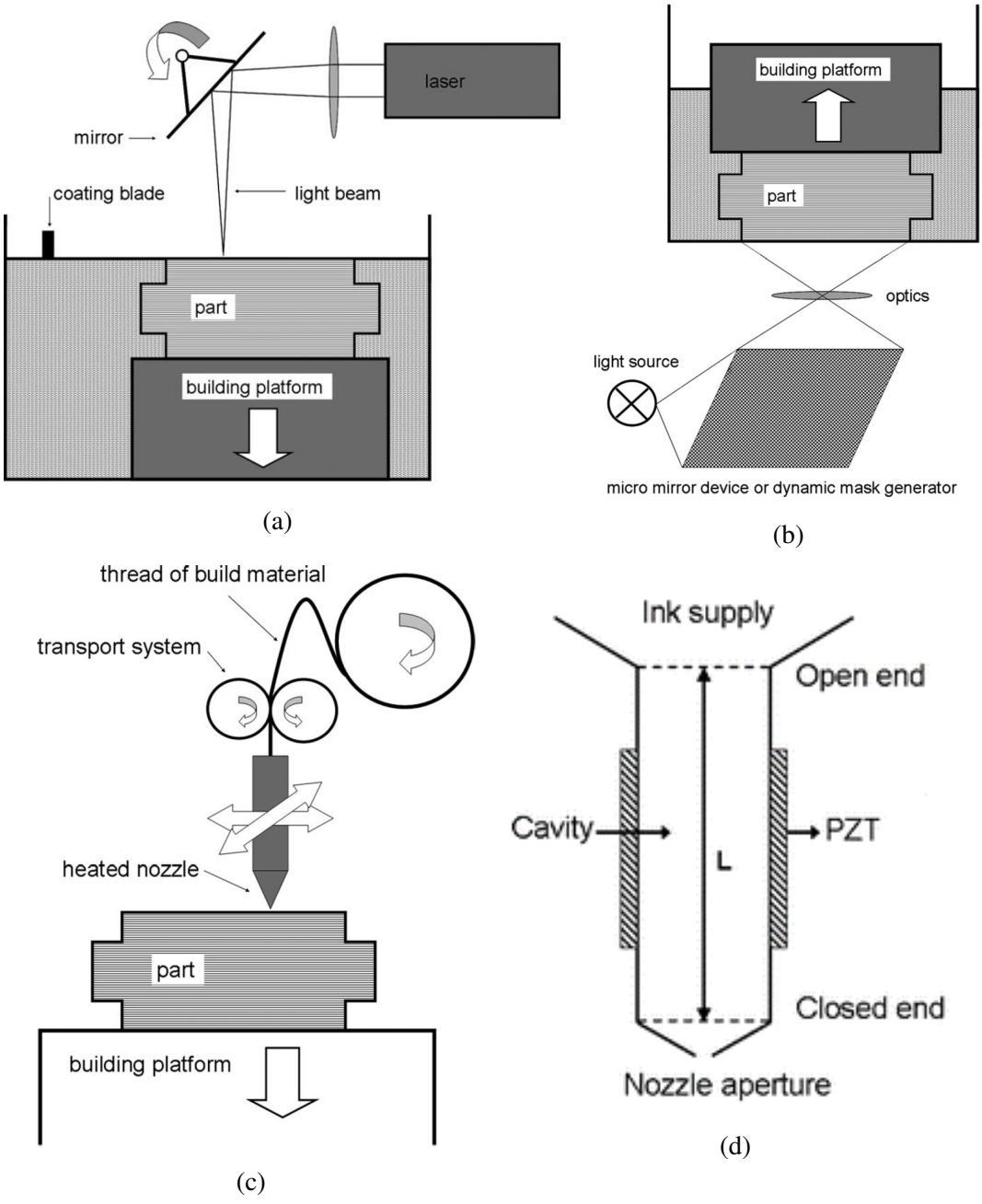

Figure 2.3: Working principles of (a) Stereolithography (SLA), (b) digital light processing (DLP) and (c) fused deposition modeling (FDM). Reprint from [42]. (d) Stucture of piezoelectric inkjet printer head. Reprint from [43].

build material, which is typically thermoplastic in the form of thread, onto the build platform, as shown in Figure 2.3b. After cooling down, the build material solidifies and forms a base for the upper layer.

Based on jetting

Inkjet printing or Multijet modeling (MJM) is based on digitally controlled generation and ejection of drops of liquid inks from a printhead nozzle onto a substrate to fabricate a 2D or 2.5D pattern [43, 44]. Inkjet printing can be realized by two different modes of operation: continuous (CIJ) and drop-on-demand (DOD) printing. Continuous inkjet fires a stream of droplets at a target and recirculates ink that isn't needed. Continuous inkjet printing is potentially fast but mainly suits production lines and bulk printing. Nowadays, the majority of inkjet printers are based on the drop-on-demand (DOD) technology, mainly with a piezoelectric or thermal generation of ink droplets. Figure 2.3d shows a piezoelectric inkjet printer head that uses piezoelectric effect to control the drop on/off with voltage or an electrical signal. Compared to the thermal inkjet printer head, the piezoelectric head is more complicated and expensive but can handle a broader range of inks [43].

A proper drop formation with equally separated droplets is essential to perform accurate printing. Researchers show that the droplet formation is correlated with the rheological properties of the ink, such as concentration, molecule weight, and ink material structure[46]. As shown in Figure 2.4, if the ink formula is not well-designed, a lot of unwanted phenomena would happen in the droplet formation:

1. Droplet tail: a long tail is formed when the droplet leaves the nozzle as shown in Figure 2.4 (a) to (e). This tail usually ends up as time goes by and the droplet jet out with a certain distance from the nozzle.

2. Satellite droplet: in addition to the regular droplet, few small droplets appear in between the regular droplets after the tail end, as shown in Figure 2.4 (a) and (b).

Beside the deposition of the ink droplet, ink curing/solidification is a significant step

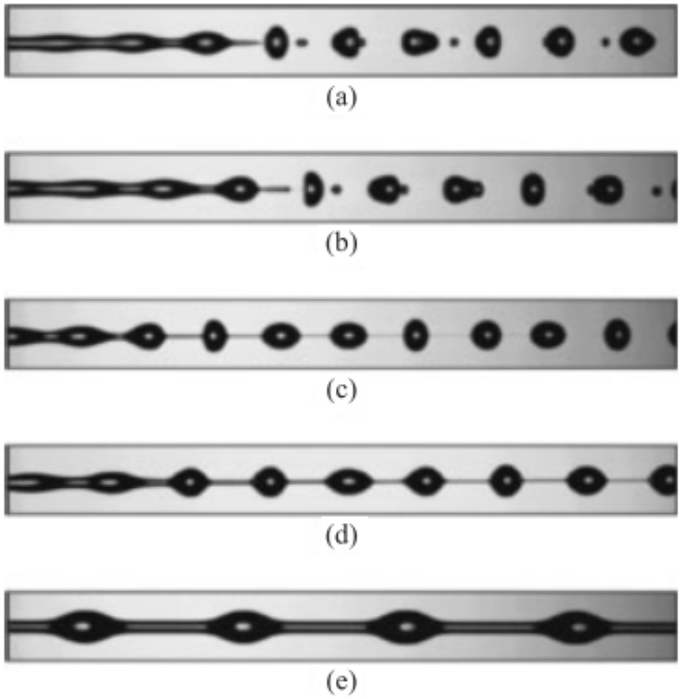

Figure 2.4: An example shows the influence of polymer molecular weight and concentration on the breakup of a fluid jet. Solvent: (a) glycerol/water (b) 0.3% 100 000 poly(ethylene oxide) (c) 0.1% 300 000 poly(ethylene oxide) (d) 0.05% 1 000 000 poly(ethylene oxide) (e) 0.043% 5 000 000 poly(ethylene oxide). Reprint from [45].

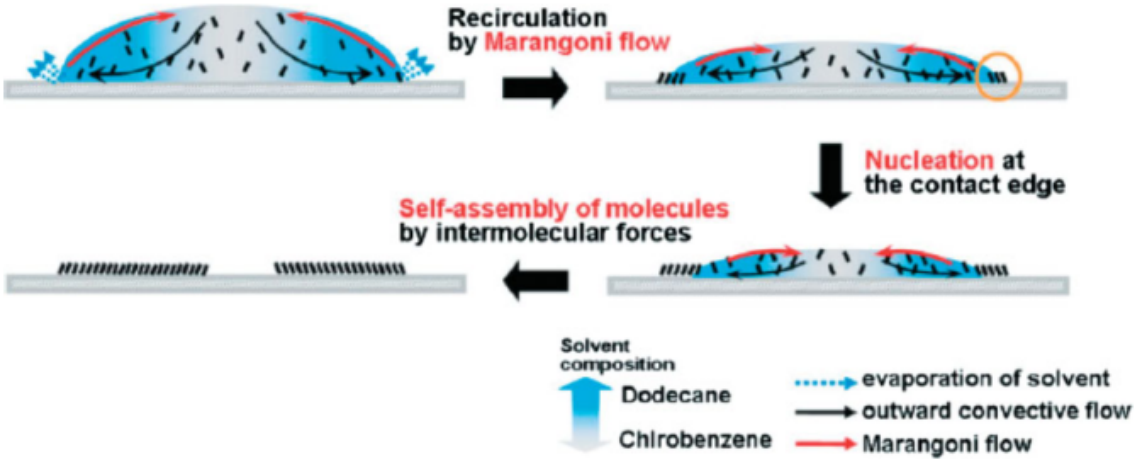

Figure 2.5: The working principles of coffee ring effect. Reprint from [47].

of inkjet-printing. During the curing, liquid evaporating from the edge is replenished by liquid from the interior, as shown in Figure 2.5. Due to a higher surface-volume ratio at the edge, evaporation rates are higher around the edge. The differential evaporation rates across the drop induce a capillary flow that can carry most the dispersed material to the edge, which results in a pattern like a ring after all solvent evaporated and the drop dried. Because this phenomenon was first found in coffee drops, this effect is named the "coffee-ring" effect[47]. The "coffee-ring" effect results from changes in the viscosity of the ink and transport of the solute via motion of the solvent, which may change surface tension interaction between the solvent and the substrate[48]. Therefore, it would leave an uneven distribution of ink material within the drop as shown in Figure 2.5 that could cause many troubles.

Inkjet ink contains several parts: an "ink" material, a liquid solvent (aqueous or organic) and various additives (such as rheology and surface tension modifiers, humectants, binders and defoamers) that enable optimal performance on the printing device and the substrate [49]. The choice of the "ink" material is mainly determined by the required physical properties of the printed pattern, such as conductivity, optical transparency, chemical resistance, and adhesion, by the physicochemical properties of the ink, such as aggregation and stability, and by its compatibility with the printing device [43]. The liquid solvent and additives are carefully chosen to improve/compensate the "ink" material for successful printing such as viscosity, surface tension, wettability and adhesion to the substrate. For example, in the case of piezoelectric print heads, the ink viscosity should be in the range of 8 to 15 cP in general, while thermal print heads usually require viscosity below three cP [43].

Piezoelectric inkjet printing techniques can print various materials including metals, polymers, and nanomaterials. The metal ink can be dispersed nanoparticles (NPs), a dissolved organometallic compound, or a conductive polymer (both dissolved and dispersed)[49]. Large-scale production of dispersions of metal NPs is now enabled by the wet chemical method which is suitable for conductive printing. Therefore, the most commonly

used conductive ink are metal nanoparticles inks, mostly silver NPs inks and gold NPs inks as they are stable in the atmosphere. As silver has a lower cost compared to gold, silver is used as the most regular conducting trace in the inkjet-printed electronics. The metallic NPs ink needs a post-printing process to sinter the separate NPs into a continuous metallic phase with numerous percolation paths within the printed patterns. Nanomaterials, such as carbon nanotubes and graphene sheets, are also very promising in inkjet-printed electronics, due to their unique properties, such as high intrinsic current mobility and conductivity, mechanical flexibility, sensitivity to gas, and their potential for low-cost production [50]. Dielectric ink which usually is a non-conducting polymer suspension or epoxy solution, is involved in inkjet printing to build the non-conducting structural features[51].

2.2.2 Electronics Fabrication

PCB

Most electrical circuits are fabricated on a printed circuit board (PCB) that uses the word "printed" but usually is manufactured by a subtractive or semi-additive process. FR-4, fiberglass-epoxy laminate, with copper cladding via electro/electroless plating is one of the most common substrates used in PCBs. Two different ways can be used to pattern the metal on PCB: direct milling and masking-and-etching. The mask is usually deposited with photolithography or screen printing. The mask approach usually provides higher resolution and accuracy but also higher cost and longer production time due to the mask. A typical single side mask-based PCB process can be found in Figure 2.6a. Overall, PCBs are cost-effective in manufacturing, however, compared to AM processes, it produces a lot of chemical waste and usually is not flexible.

Microelectronics

Microelectronics and Microelectromechanical systems (MEMS) are traditionally manufactured by photolithography based techniques, a conventional planar manufacturing technique utilizing light-sensitive materials (photoresist) and masks. There are two types of

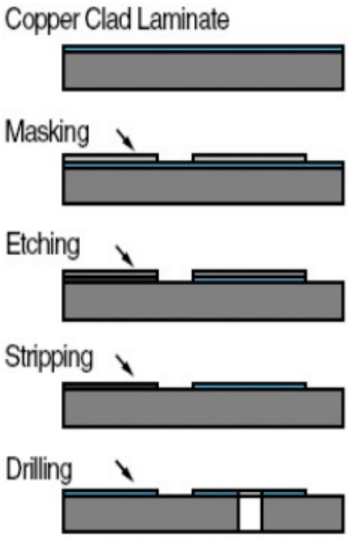

(a)

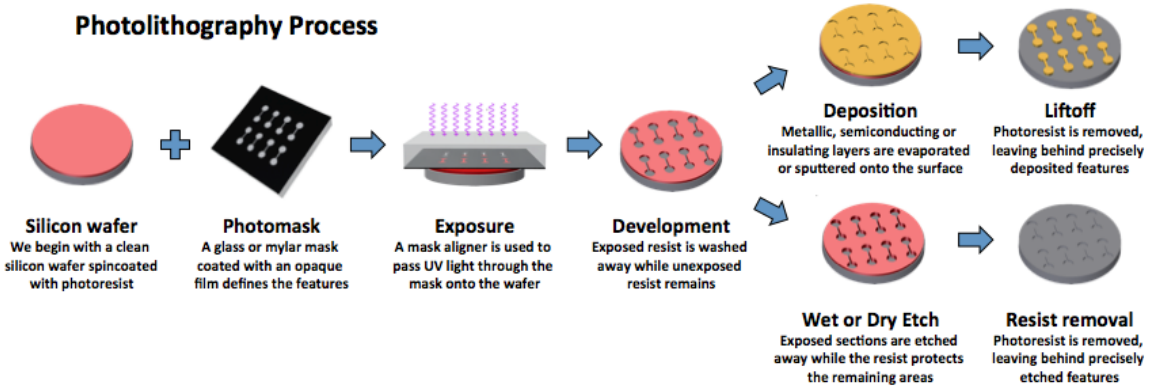

(b)

Figure 2.6: Step-by-step process of (a) single side printed circuit board (PCB) (picture found at [52]), (b) photolithography with lift off process or etch process (picture found at [53]).

photoresist: positive and negative, the former one can be dissolved in the developer only after exposure to light while the latter one can be etched out only without exposure. There are also two ways to use photoresist: lift off and etch out, as shown in Figure 2.6b. Photolithography features an unbeatable high resolution but requires costly equipment and a cleanroom environment. The process is very complicated, has multiple stages, and involves deposition of many layers of different materials. The process also produces a significant amount of chemical waste and thus is environmentally unfriendly. Therefore, though these processes manage to achieve an extremely high resolution, the expenses of these processes are very high, which limits the application of the fabricated devices.

Inkjet printing

The market for printed electronics, which is estimated to exceed $300 billion over the next 20 years [44], requires manufacturing techniques that are faster, cheaper and eco-friendlier compared to traditional production methods. Because inkjet printing is an additively manufacturing method that can pattern various materials including metal, semiconductors, and dielectrics, it is a very attractive technology for cost-effectively manufacturing various electronics including circuit boards, RFID tags, thin film transistors, light emitting devices, solar cells, touch screens, and flexible displays [44, 47, 54, 55]. Cost is one of the most significant concerns in consumer electronics manufacturing. The fact that inkjet printing can fabricate electronics at relatively low cost leads it to be massively involved in electronics manufacturing. Inkjet printing is favorable for automation and enables patterning with relatively high resolution. With industry level inkjet printers, a relatively high resolution and a relatively low cost can be balanced for specific applications. No waste is created in the whole process, and less harmful/aggressive chemicals are involved, which results in a "green" process [56]. Also, inkjet printing is very suitable for manufacturing large area electronics by the roll-to-roll (R2R) technique [44].

Other AM processes

Besides inkjet printing, the most popular 3D printing techniques (e.g., SLA, DLP,

FDM) deal with dielectric materials [41]. However, in electronics, metal is almost unavoidable because high conductivity is the key to reduce power consumption and to improve performance. Recently, many 3D printing methods have also been developed to print metals while the costs of these process are high in general so far. For example, direct metal laser sintering (DMLS), a laser-based additive manufacturing process that is similar to selective laser sintering (SLS) and selective laser melting (SLM), can directly print 3D objects by melting/sintering metal powders with laser beams.

2.2.3 Microfluidics Fabrication

Photolithography

In the early 1990s, microfluidics were first fabricated in silicon and glass using photolithography[57]. As mentioned in former paragraphs (section 2.2.2 and Figure 2.6b), photolithography features a high resolution and accuracy, but is multi-staged, requires high-cost equipment, and uses environmentally undesirable chemicals, which add up and limit the popularity of microfluidics devices. Figure 2.7 shows a comparison of costs and production volumes of different microfluidic fabrication methods [58].

Soft-lithography

At the end of the last century, the soft-lithography technique was invented by pouring a thermosetting material, Polydimethylsiloxane (PDMS), into a replica mold and casting the microfluidics as shown in Figure 2.8a [60, 61]. Soft-lithography features a much lower cost and a much faster production speed compared to old photolithography methods. Moreover, soft-lithography facilitates designs of high flexibility and high optical transmittance, and thus has become the most common microfluidics fabrication process. However, this mold-based method usually needs photolithography to fabricate the mold. Thus, soft-lithography is a semi-cleanroom process which still heavily relies on costly photolithography techniques. Furthermore, because the production quantity needed for each specific microfluidics design usually is very small, the mold-based approach can be very costly and may not

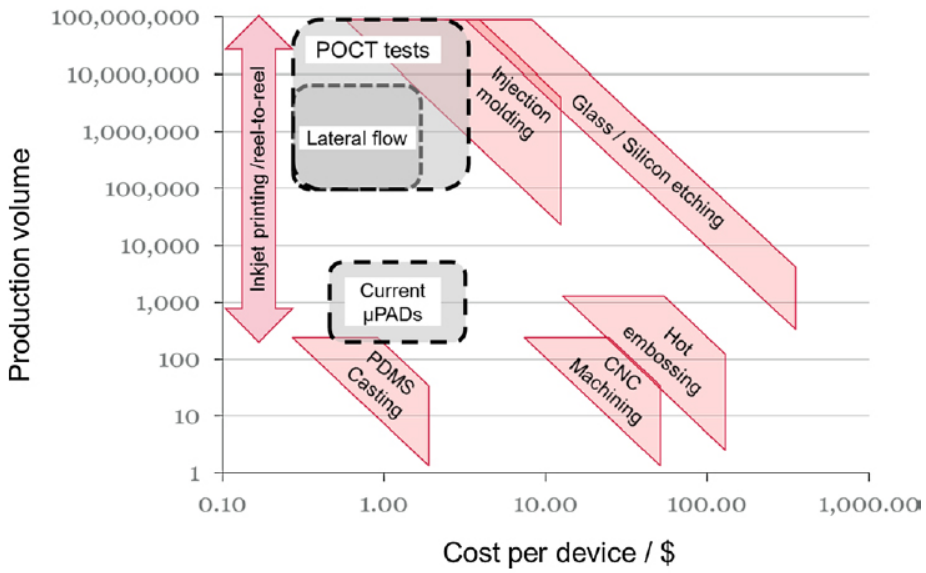

Figure 2.7: Cost and volume comparison for common Lab-on-A-Chip fabrication technologies. Reprint from [58].

be the best option [62].

Based on paper substrate

In 2007, Whitesides and colleagues developed paper-microfluidics [63]. They patterned the channel and divided the paper into different functional areas/channels (chemical sensors), by printing hydrophobic walls on paper, as shown in Figure 2.8b. Since then, paper-microfluidics and paper-based microfluidic analytical devices (uPAD) have been in the spotlight as they enable the integration of multiple chemical tests into a single strip[64, 65, 66] at a very low cost owing to the additive manufacturing methods used[67, 68]. Because of its inherent advantage that the paper fibers in the channel can hold the reagents within themselves, its high information capacity by integrating multiple chemical sensors, and the low-cost fabrication process as well as material used in these devices, paper microfluidics has become an essential subject in microfluidics research.

AM processes

Additive manufacturing (AM) has attracted significant attention in recent years as it can rapidly fabricate structures at a low cost with no waste. Researchers have already tried to

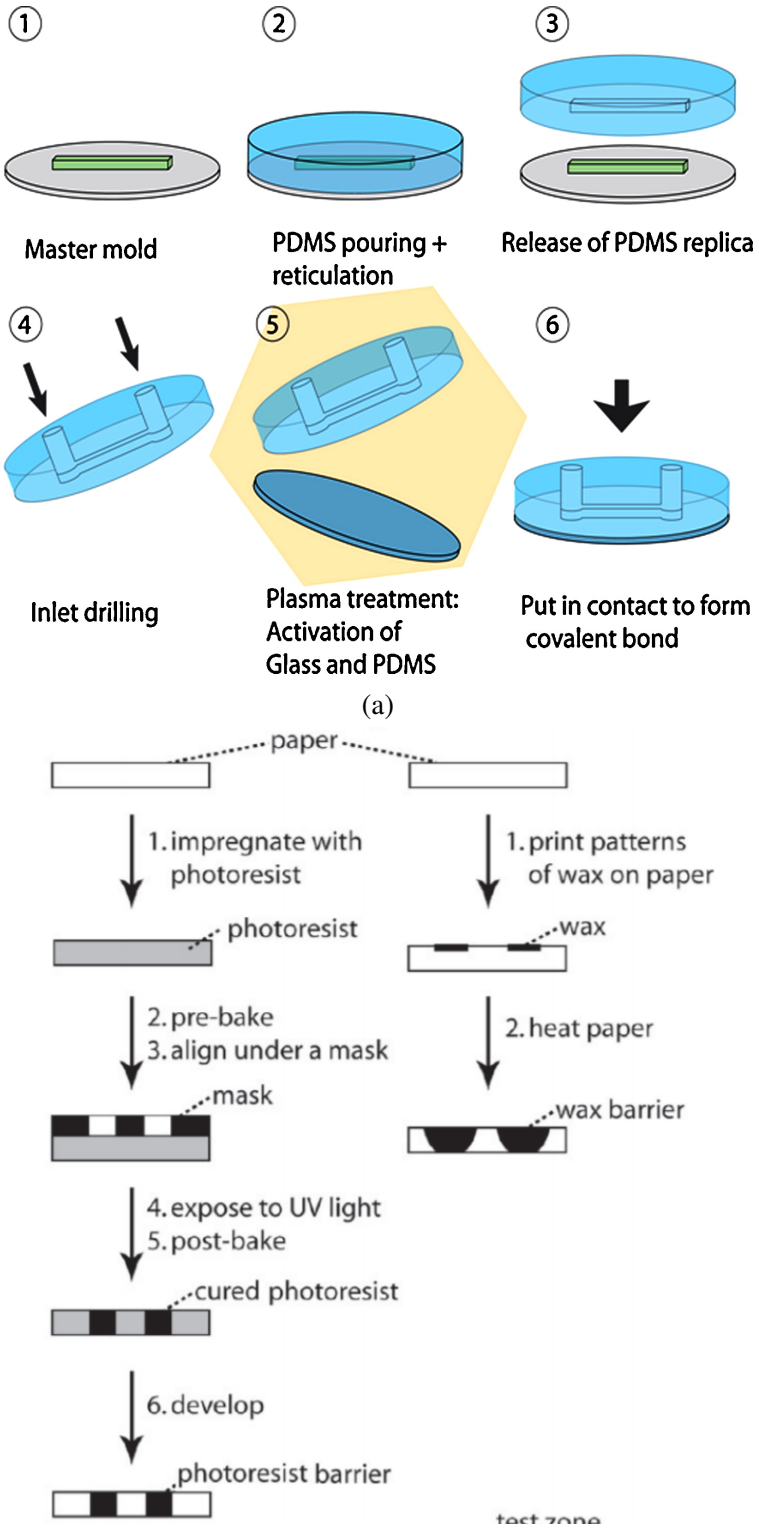

Figure 2.8: Step-by-step process of (a) soft lithography for microfluidics devices (reprint from [4]), (b) paper microfluidics with photolithography and wax printing (reprint from [59]).

utilize numerous 3D printing techniques, the most well-known AM subclass, in microfluidics [62, 69, 70, 71, 72, 73, 74, 75, 76, 77, 78]. Most 3D printing-based approaches only print the mold for casting while still take the mold-based approach of soft-lithography [69, 74], which partially solves the problem of soft-lithography. Other moldless approaches directly print the microfluidics device entirely with various 3D printing techniques, which efficiently enable the rapid prototyping of microfluidics [71, 79, 75, 76, 77]. Another AM technique, inkjet-printing, also has been utilized in microfluidics fabrication including paper microfluidics [80, 63, 81, 58] and many other approaches [82, 83, 84, 85, 86]. However, currently most 3D printers feature low resolutions and large minimal feature sizes [73], which results in a typical large cross-section area of 3D printed microfluidic channels at least on the level of $5 \times 10^4 \mu m^2$ [69, 70, 71, 79, 75, 76].

CHAPTER 3
ADDITIVE MANUFACTURING PROCESSES FOR MICROFLUIDICS AND ELECTRONICS

As discussed in the previous chapter, the state-of-art fabrication processes based on photolithography and other subjective manufacturing techniques have a high cost that limits the fabricated devices in many applications. The need for a cost-, time- and effort-effective fabrication process for smart sensors in Internet-of-Things applications has grown drastically recently. Therefore, in this chapter, several AM-based processes, which are low-cost, easy-to-reconfigure on demand, rapid-prototyping, eco-friendly, low-temperature, and zero-waste, are demonstrated for Internet-of-Things, especially microfluidics-based wireless liquid sensing and microwave tunable components.

3.1 Inkjet Printing

This work investigates, in depth, the inkjet printing not only of conductive electronics but also of multi-layer / 3D structures. All the inkjet printing processes were conducted in a Dimatix DMP-2831 inkjet printer with a 1.5-mL-capacity cartridge and a ten pl drop volume. A 20 μm drop spacing was chosen to balance the printing speed and performance unless specified.

I will first introduce the inks used in section 3.1.1, then the three individual processes utilizing inkjet printing as a tool for bonding, molding, or building a structure directly in section 3.1.2 to 3.1.4, and finally a process to print microfluidic electrical sensors on filter paper in section 3.1.5.

Table 3.1: Inks and its printing /curing conditions

Inks	Constitute or product name	Printing temperature (recommended)	Curing condition (recommended)
SNP	SunTronic EMD5730 or ANP Silver-Jet-55LT-25C	60°C	180°C for 1 hour
SU-8	Microchem SU-8 2002, 2005	25°C	Following the data sheet[87]
PMMA	PMMA, anisole, DMSO	25°C	120°C for 40 mins

3.1.1 Inks

As introduced in section 2.2.1, conductive patterns in electronics can be printed with inks based on metal nano-particles while non-conductive inks such as polymer ink can be printed for structural features. In this section, two silver nanoparticles (SNP) inks and two polymer inks are introduced and utilized in the inkjet-printing of microfluidics and of electronics: SNP, SU-8, and PMMA inks. Table 3.1 summarizes the four inks in this section.

SNP inks

SunTronic EMD5730 Jettable silver nanoparticle (SNP) ink from Sun Chemical Corporation (Parsippany, USA) and Advanced Nano Products (ANP) Silver-Jet-55LT-25C SNP ink is used. High-temperature sintering at 180°C for 1 hour in a thermo scientific oven provides the best conductivity. For a substrate that cannot stand high temperature, excellent conductivity can be achieved by low-temperature sintering at 120°C for 1 hour along with flash curing at 180°C for 5 minutes. In the case that substrate cannot stand high temperature, such as PMMA and many 3D printed materials, locally sintering using a laser beam with appropriate energy is an efficient solution.

SU-8 ink

SU-8 is a well-known epoxy-based negative photoresist. Home-made SU-8 ink is a blend of SU-8 2002 and SU-8 2005 (Microchem Corporation, Westborough, USA). The ratio of two different viscosity SU-8 fluids was carefully tuned for successful printing in

the specific printer. The ink can be cured in a 3-step process: a soft-bake (95 °C), an Ultraviolet (UV) exposure, and a hard bake (95 °C).

As discussed in the section 2.2.1, the "coffee ring" effect can largely influence the shape of the dried ink to be a basin-like topology. The influence of the "coffee ring" effect is related to the area (horizontal dimensions) / height ratio of the pattern: for a small area/height ratio, such as lines and dots, the influence is less obvious; for a large area/height ratio, it is significant. Therefore, both the inkjet-printed "lines" (0.5 mm $\times$ 7 mm) (minimal "coffee ring" effect, Figure 3.1a) and the rectangular "pads" (7 mm $\times$ 7 mm) (significant "coffee ring" effect, Figure 3.1b) were inkjet-printed for different numbers of layers. For "lines" patterns, the height per layer is reliably around 6.8 μm/layer, as shown in Figure 3.1a. For "pads" patterns, heights at the center of the pattern and at the top of "coffee ring" hill (maximum height point) are shown in Figure 3.1b, which demonstrates that the height per layer is around 5.6 μm/layer in the center and 7.1 μm/layer at the "top of hill." When more layers are printed (e.g., 11-12 layers), the resulting solidified SU-8 shapes are closer to "lines." Figure 3.1c show the measured profiles of the inkjet-printed "pads" for different numbers of layers. The two dashed lines in the Figure 3.1c present an almost linear relation of between the "hill" height and the width from the "top of hill" to the edge, which is dominated by both the drying speed and the contact angle of the SU-8 ink on the underlying substrate. The ratio of top-hill trend can be calculated to be 55 μm (height): 1 mm (distance to the edges).

The influence of printing platform temperature is also investigated. Theoretically, the substrate temperature changes the contact angle of the ink and the coffee ring effect, which may lead to different profiles. However, as the temperature of the printing platform is relatively low compared to the temperature of the hot plate used in curing process and printing time is short in most cases, the evaporation during printing is much smaller than the evaporation during the curing process. Therefore, the influence of the temperature of the printing platform is negligible. As a proof, numerous independent samples of 7-layers

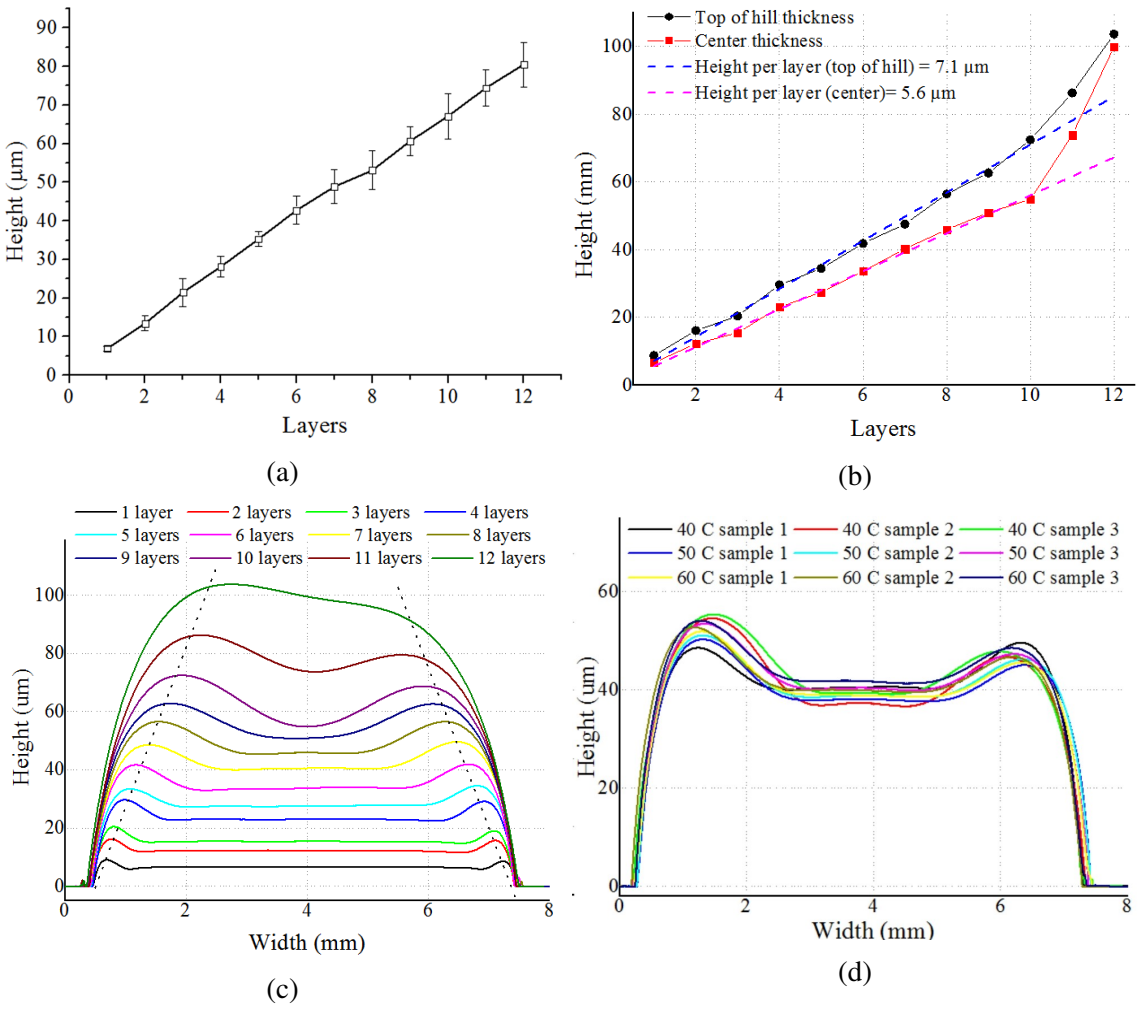

Figure 3.1: Performance of inkjet-printed SU-8.
(a) Height of the printed "lines" for 1 to 12 layers of print. (b) Height of the printed "pads" in the center and in the top of the hills for 1 to 12 layers of print. (c) The profile of the printed "pads" for a different numbers of layers with two dotted lines marking the coffee ring hill-top trend. (d) The profile of the inkjet-printed rectangular pad prototypes at various printing platform temperatures (40°C, 50°C and 60°C; 3 samples at each temperature).

"pad" patterns were inkjet-printed at 40°C, 50°C and 60°C, respectively and no correlation between the temperature and the outcome shapes of the printed prototypes were observed as shown in Figure 3.1d.

PMMA ink

Poly(methyl methacrylate) (PMMA) ink can be made by dissolving PMMA powder into a mixture of anisole and dimethyl sulfoxide (DMSO) (Sigma-Aldrich Corporation, St. Louis, USA). Anisole can dissolve the PMMA powder, and DMSO can optimize the ink drops surface tension and viscosity. The ink can be cured by heating at 120°C for up to 40 mins to evaporate all the solvent.

To find out minimal feature size of inkjet printed PMMA traces, various single-drop line (consecutive single drops in one direction/line) prototypes were printed with different drop spacings. The line prototypes are 5 mm long and a subsection is shown in Figure 3.2a and 3.2b. Figure 3.2c shows the realized height and width values of these prototypes, which demonstrates that a larger drop spacing means less deposited material per unit area, so it results in thinner lines, because the surface tension, instead of the pre-set pattern, is the critical factor of the shape of formed lines. However, for drop spacings larger than 40 μm, line breakages happen, which is random and should be avoided. Therefore, the smallest/thinnest inkjet-printed PMMA line is 60 μm wide and 0.8 μm high with a 40 μm drop spacing. The relation between trace height and the number of layers was investigated by printing numerous 7 mm $\times$ 0.6 mm lines 1 to 15 layers. Figure 3.3a shows that the average layer height is reliably around 4.6 μm with less than 0.4 μm variation. Due to the liquid nature of the ink, the cross-section of the printed trace features a semi-elliptical shape as shown in Figure 3.3b.

3.1.2 First Approach: Printing for Electronics and Bonding Microfluidics

Fig 3.4 shows the inkjet printing for bonding process that combines inkjet-printing and laser-etching techniques to provide a simple and low-cost solution to fabricate microflu-

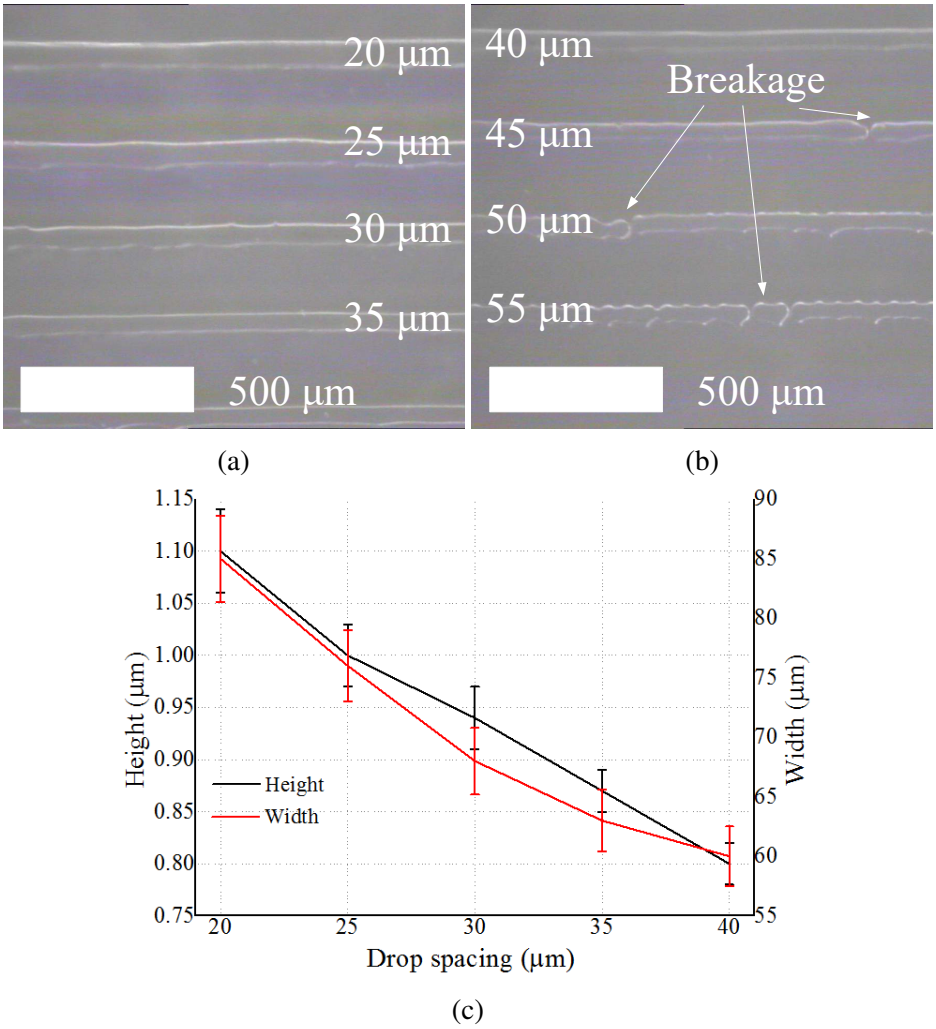

Figure 3.2: Smallest features of inkjet-printed PMMA. (a, b) Photos of "single-drop" test. (c) Measured average heights and widths with error bars of the printed PMMA line prototypes in (a, b).

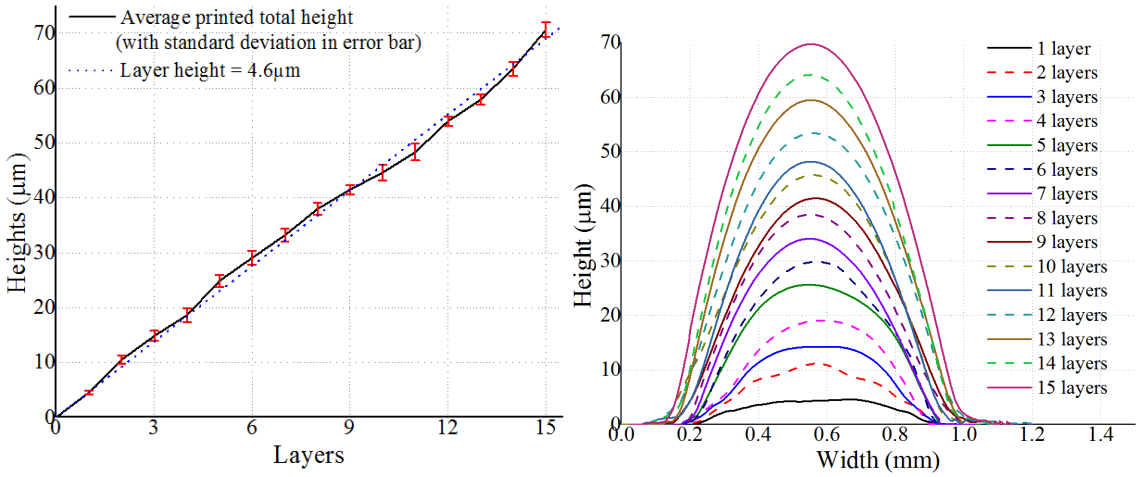

(a) (b)

Figure 3.3: Performance of inkjet-printed PMMA. (a) Average height and error bar of 1 to 15 printed layers. (b) Cross-sectional profile of the printed PMMA lines in (a).

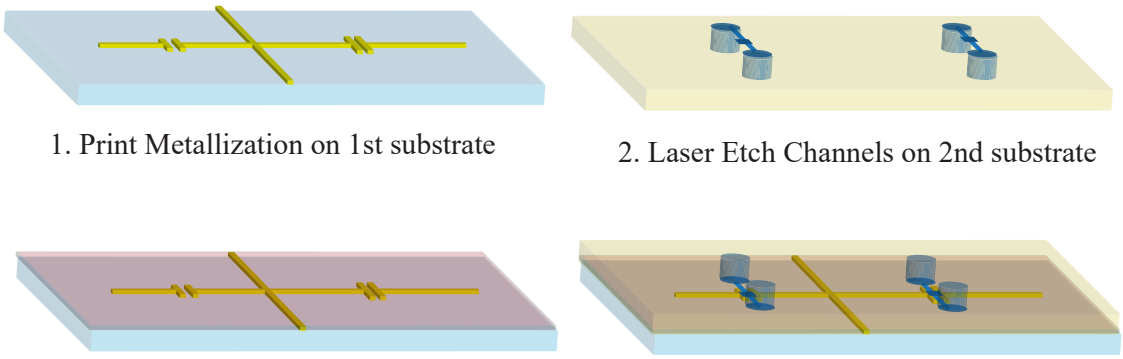

1. Print Metallization on 1st substrate

2. Laser Etch Channels on 2nd substrate

3. Print Bonding Layer on 1st substrate

4. Bond two substrates

Figure 3.4: Step-by-step fabrication process utilized inkjet printed conductor for electronics and polymer for bonding microfluidics.

idics sensors. In this process, a 2-μm-thick layer of conductive traces was printed on the first substrate with SNP ink while the second substrate was laser etched to obtain notches for microfluidic channels. Then a 14-28 μm layer of SU-8 was printed on the first substrate. Two substrates were pressed together and cured of printed SU-8 on a hot plate with 10 N weight. Because of SU-8's epoxy nature, it can bond the two substrates and seal the microfluidics channel without blocking the channel. In the meanwhile, the SU-8 polymer layer can separate the liquid in the microfluidic channel from the metalization/first substrate so that a proper isolation is achieved simultaneously. To prove of concept, the first substrates used are papers[88, 89] or PMMA sheets[90, 91] while a PMMA sheet is the second substrate. Paper is a low-cost substrate with an excellent wetting capability which is widely used in inkjet-printing and PMMA is an inexpensive polymer with excellent transparency. Papers used are 230 μm Kodak photographic papers (Office Depot, Atlanta, GA, USA) and the PMMA sheets used are 1.5 mm thick from McMaster-Carr, Atlanta, GA, USA.

Fence printing was explored for the situation when the surface tension of the substrate is not optimal and the ink spreads out. For example, ANP Silver nanoparticles ink have a higher surface tension than the surface energy of a PMMA sheet, so the ink spreads out and cannot maintain its shape after deposition. A 7-μm-high fence can be printed with SU-8 ink before printing the ANP SNP ink, which helps to constrain the ANP SNP ink and maintain the pattern.

3.1.3 Second Approach: Printing Electronics and Molding Microfluidics

The second fabrication process replaces all the subtractive photolithography steps in the soft-lithography process (introduced in section 2.2.3) with the additive inkjet-printing, resulting in a much lower cost and a sufficiently high resolution. This method can be used to mount "on demand" microfluidics, taking full advantage of the microfluidics capabilities in packaging and liquid-reconfigurable electronics. The materials used for the proof-of-

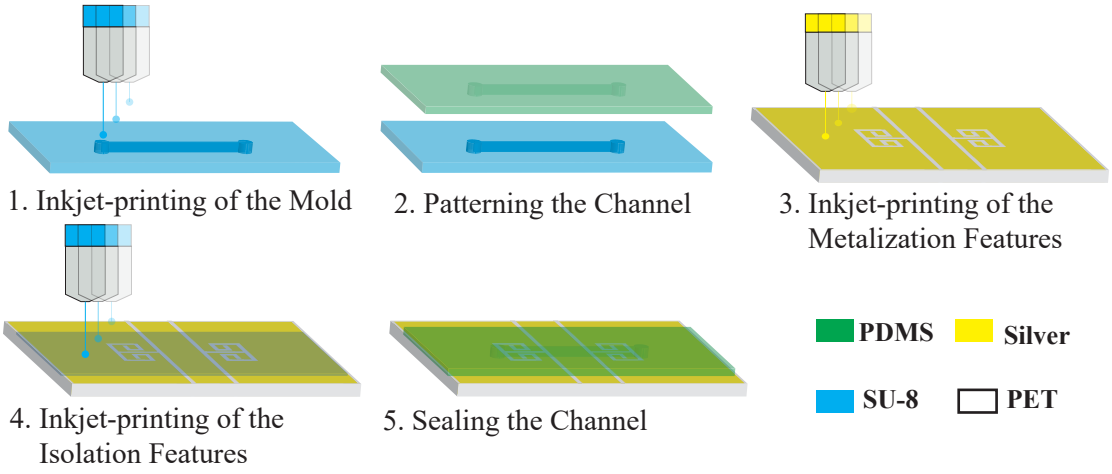

Figure 3.5: Step-by-step fabrication process utilized inkjet printed conductor for electronics and polymer for molding microfluidics.

concept prototype were the Sylgard 182 Silicone Elastomer Kit (Dow Corning Corporation, Midland, MI, USA), the raw material of PDMS, for the construction of the microfluidic channel, and a sheet of 0.127-mm-thick polyethylene terephthalate (PET) (DuPont Teijin Films, Chester, VA, USA).

The five-step fabrication process is shown in Fig 3.5. The first step covers the inkjet printing of a microfluidics mold, while in traditional soft-lithography processes for the microfluidics fabrication, the fabrication of the mold is carried out by photolithography in the cleanroom environment. In this method, SU-8 lines are inkjet-printed on a glass substrate, which serves as a mold and defines the shape of the fluid channel. The characterization of SU-8 lines is shown in Figure 3.1a, which illustrates a 6.8 μm vertical resolution. In the second step, similar to traditional soft-lithography, the raw PDMS material is poured into a container until overflow and is degassed with vacuum for three rounds. To transfer the pattern from the inkjet-printed channel to PDMS, the glass substrate is then flipped and squeezed to cover the container as a lid with the SU-8 pattern on the bottom side. To cure PDMS, the container was heated at 100°C in a Thermo Scientific oven for 75 minutes.

After fabricating the microfluidic device with inkjet printing and soft-lithography, the electronics part can be inkjet printed with SNP inks on a flexible substrate such as PET,

following by a inkjet-printed isolation SU-8 layer to separate the tested fluid and the electronics pattern and smooth the surface simultaneously. Sealing of the PDMS microfluidic channel and PET substrates was conducted by Van Der Waals force: simply applying a force to hold the PDMS device and PET substrate together can successfully bond the two parts together. Figure 3.6a shows the cross-section view of a fabricated device; an arch-like structure without sharp corners is achieved for the channel due to the circular mold shape as the mold is printed by ink in the liquid phase. Figure 3.6b shows the "peel-and-replace" reconfigurable capability due to reversible sealing. On the one hand, this reversible sealing features a strong enough bonding to prevent fluid leakage and to handle the pressure in the capillary action. On the other hand, reversible sealing gives the prototype a unique "peel-and-replace" capability. The microfluidic part can be easily peeled off from the electrical part if needed, as shown in Fig. 3.6b, thus making sensitivity switching possible, as microfluidic parts with different channel designs can be easily attached to the same RF pattern/structure (electrical parts). Various combinations of microfluidic and electrical parts can enable a significant degree of reconfigurability and functionality of the RF system. Moreover, reversible sealing also simplifies the cleaning process between two consecutive uses, and thus allows reusability. The prototype can be demounted and cleaned part-by-part to remove any leftovers from the latest test.

Various channel sizes were fabricated and tested to explore the limits of the proposed channel fabrication process. The line in Fig 3.6c presents the minimum aspect ratio (width value/height value) of 7, which is limited by the contact angle between the contact surface and the ink solution. The smallest feature achieved had the width of 100 μm and the height of 6 μm. Various tests were performed by repeating steps 1, 2, and 5 for different widths or heights to fabricate the testing matrices and by filling them with food color dyed water and ethanol, as shown in the inserted photograph in Fig 3.6c.

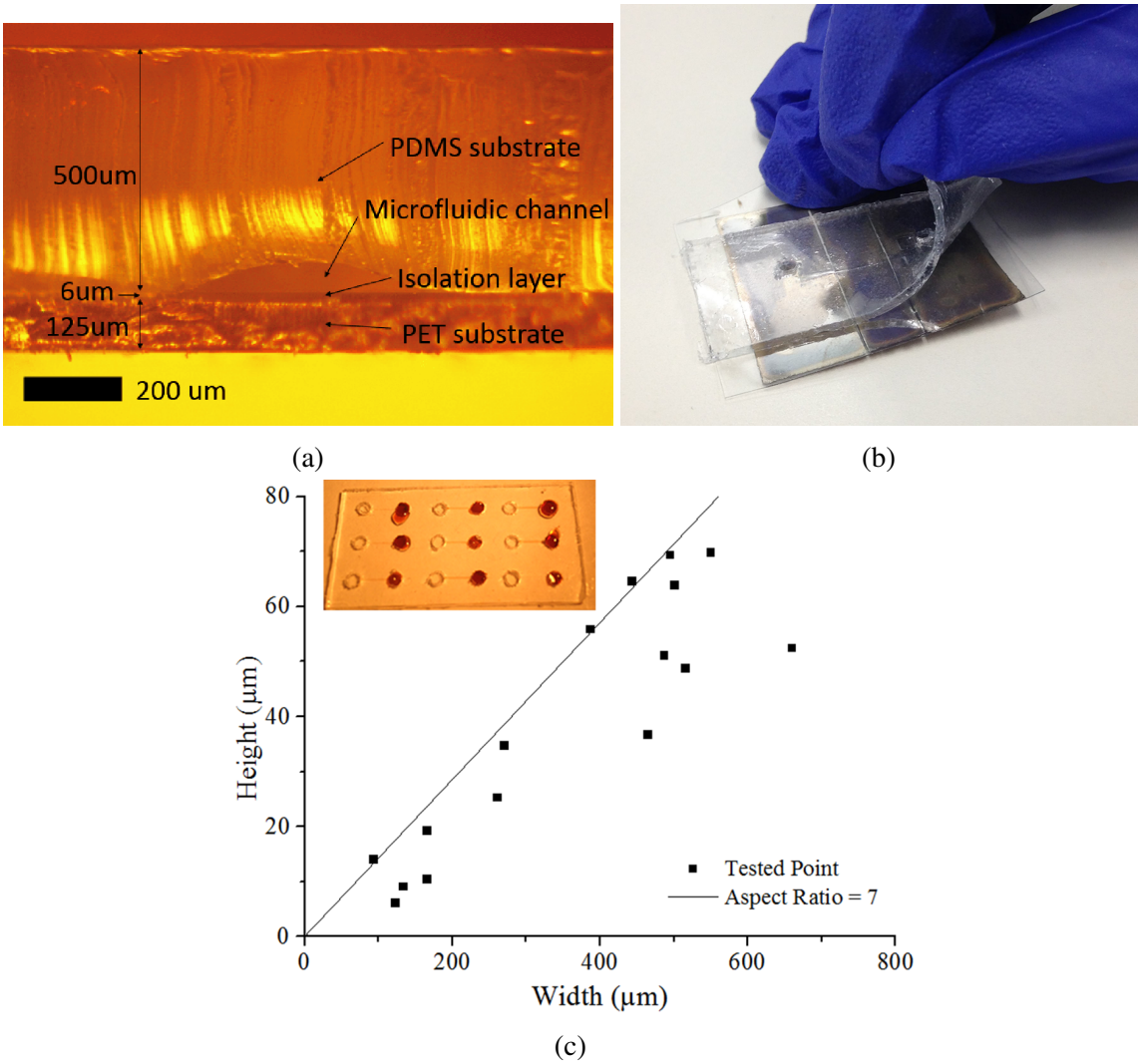

Figure 3.6: (a) A photo in the cross section view of a microfluidic device by the inkjet printing molding method. (b) A photo of the fabricated prototype with the PDMS sheet (microfluidic part) partially peeled off from the PET sheet (electrical part), to illustrate the "peel-and-replace" capability. (c) Tests of the possible dimensions of the proposed fabrication process.The dots represent successful individual tests. The line in the graph shows the lower limit of the successfully fabricated aspect ratio. The small inserted photograph in the figure gives the reader a glance of the testing matrix.

3.1.4 Third Approach: Fully Inkjet Printing

This section shows the first fully inkjet-printed microfluidics. Unlike the two processes introduced above, this process relies only on inkjet-printing technology and enables rapid fabrication of complex microfluidics networks with 3D configurations on virtually any substrate at an extremely low cost. Besides paper microfluidics which prints only the barriers, inkjet-printing has also been used in various steps in microfluidics fabrication process including sealing the channel[84]; building the mold for PDMS replication[85, 83]; patterning the mask for channel etching[82]; printing the sidewall between two substrates.[86]. It's easy to notice that these approaches still require co-fabrication with other fabrication techniques, such as laser etching[92], 3D printing[84], wet etching[82] or soft-lithography[85, 83], which complicates the fabrication process flow and may increase the cost significantly.

In the proposed approach, 3D microfluidics devices are fabricated by inkjet-printing different materials level-by-level as shown in Figure 3.7. Two different polymer inks are involved: the SU-8, which constructs the microfluidic channel, and the PMMA, which supports the SU-8 structure during curing and is washed out afterward. Due to its high chemical resistance, SU-8 can remain almost intact during etching and after interaction with most organic and inorganic solvents under test inside the channel. PMMA, on the other side, is easy to wash out with organic chemical solvents such as Anisole. Because PMMA ink is always printed on SU-8, no matter what substrate is used and how many levels the structure has, a great consistency and excellent control of the channel shape can be achieved.

The printing process can be represented by the flow of the four steps in Figure 3.7. Firstly, a thin level of SU-8 ink was printed on a substrate to isolate the substrate from the fluids in the microfluidic channel. For applications such as contactless electrical sensing, this isolation can eliminate the unwanted contact of metals/conductors (if any) with the fluids under test. For porous substrates such as papers and corks, the isolation layer can fill small substrate holes/voids and provide a water-proof channel. For substrates with

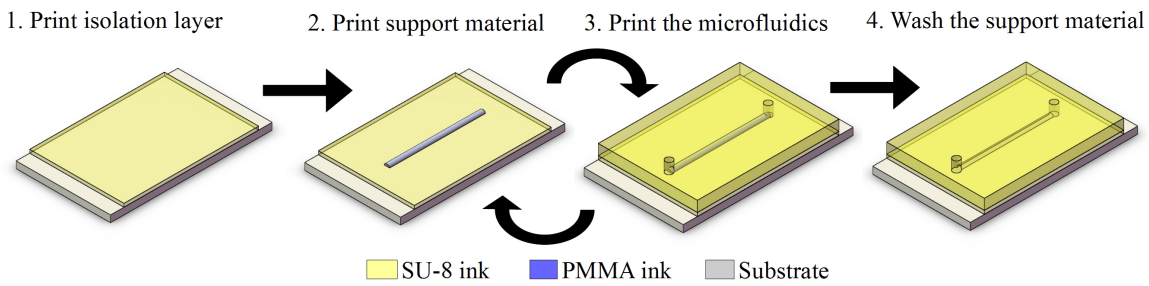

Figure 3.7: Step-by-step fabrication process of fully inkjet printed microfluidics and electronics.

slightly uneven surfaces, this printing approach can smooth out the undesired roughness. This isolation printing is a preparatory step in the cases of problematic substrates, and thus it can be eliminated otherwise. Because of this step and the additive nature of inkjet-printing, this process enables building 3D microfluidic structures on virtually any substrates or devices including but not limited to glass, paper, silicon wafers, metal, plastic, and other existing microfluidics chips as well as packaging structures. This feature enables adding a microfluidic structure to any existing original design and fabrication process and thus makes this process one of the best candidates in microfluidics monitoring, sensing, and cooling. Secondly, a patterned PMMA trace was deposited as a placeholder for the microfluidic channel topology, which would support all the materials deposited on top of the channel in the following steps. Consequentially, this printed pattern is same as the designated microfluidics channel pattern. Thirdly, a thick SU-8 layer was printed which constitutes the microfluidic channel walls at the end of the process. The openings (inlet and outlet) of the microfluidic channel are preserved by the pattern file printed. As the SU-8 ink is in the liquid phase, it would even out the surface including the printed PMMA traces if enough amount is deposited, resulting in a flat surface of the device. Finally, after all the levels are printed, the removal of the PMMA support material is carried out by an anisole solution bath, although several other alternative organic solvents could work as well. As etching relied on the diffusion of the etching solvent, we found that the etching time, which strongly depended on how narrow and long (e.g., cross-section area/length

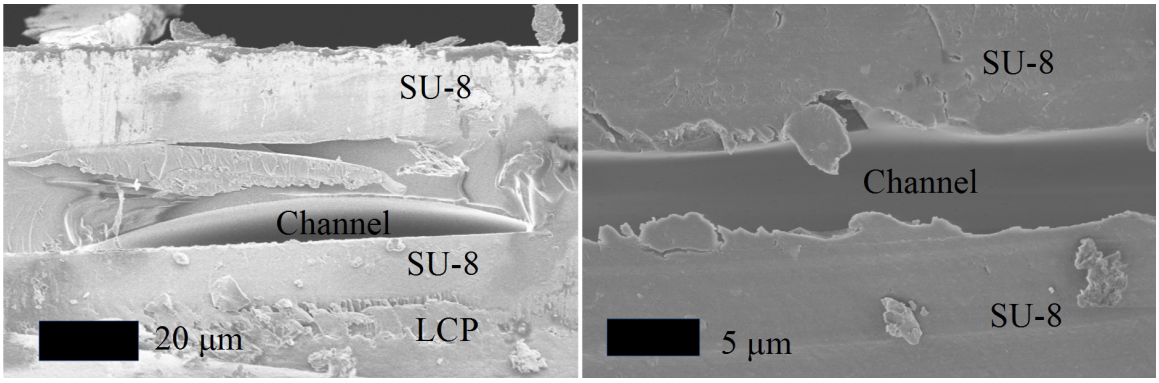

Figure 3.8: SEM images of fully inkjet printed microfluidics. The debris particles shown in the SEM images very likely were SU-8 polymer.

ratio) the channel was, can be significantly decreased by applying an ultrasonic bath. After the removal of the support material in the channel, a hollow channel embedded within the SU-8 polymer can be observed with the same shape as the printed PMMA pattern as shown in Figure 3.8. And scanning electron microscope (SEM) photos of the cross-section of proof-of-concept channel prototypes are shown in Figure 3.8.

The proposed fabrication process can be used to fabricate 3D microfluidics structures by repeating the second and third steps in the process in Figure 3.7 with a level-by-level mechanism. Every channel that is on top of another channel is defined as a new level as it needs to be printed after the completion of the bottom level. Each level is pretty independent in terms of printing, which means not only there are no limitations on what pattern is printed, but also each level can be fabricated with a different level height/thickness without any extra effort (such as the first, second and third levels in Figure 3.9a that feature three different level heights). For the printing of each level, the fabrication process is the same as described above, except that instead of printing on the isolation level, the pattern is printed directly on the underlying layer, thus leading to 3D microfluidics configurations constructed of numerous single-level ones. In this way, the whole microfluidics structure is still constructed using the same material, SU-8. This feature differentiates the proposed inkjet-printing method from the other level-by-level approaches, such as stacking single layer 2D microfluidics structures by inserting adhesive layers. An example of two fully

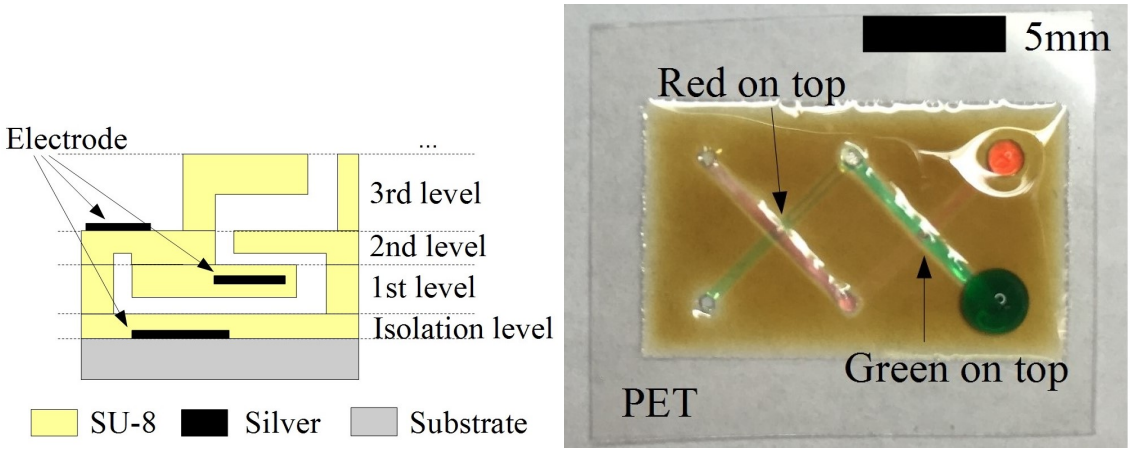

(a) (b)

Figure 3.9: Sketch and prototype of a fully inkjet-printed 3D microfluidics structure. (a) Sketch of the side view of an arbitrary fully inkjet-printed 3D microfluidics structure with integrated conductors. (b) A photo of two fully inkjet-printed twisted 2-level 3D microfluidic channels. Due to the capillary effect, one channel is filled with red dyed water, and the other is filled with green dyed water. The two channels are twisted to each other: The green one is on top of the red one in the right half and is beneath the red one in the left half.

inkjet-printed twisted 2-level microfluidic channel prototypes can be found in Figure 3.9b, which demonstrates the excellent capability for the fabrication of complex 3D microfluidics topologies.

Basic and flexible microfluidics structures, such as a straight channel (Figure 3.10a), a T-junction (Figure 3.10b), a Y-junction (Figure 3.10c), a meander line (Figure 3.10d) and a mixer (Figure 3.10e) can be easily fabricated. Microfluidics devices fabricated with the proposed approach feature a very promising pressure handling and endurance. Water has been continuously pumped through the fabricated channels at 0.1 mL/min for over 10 hours, which shows a long-term water exposure capability. The printed microfluidic channels can operate at relatively high throughputs, such as up to 2 mL/min for a 0.03 mm^2 cross-section area channel, which demonstrates an excellent pressure handling capability. As the sizes (cross-section areas) of the fabricated channels are typically in the range of 38 to 6×10^4 μm^2, many microfluidics physical phenomena, such as the capillary effect (e.g. Figure 3.9b and Figure 3.10a) and the laminar flow (e.g. Figure 3.10c), can be observed

with fabricated devices.

Five proof-of-concept substrates, namely PET (poly(ethylene terephthalate)) (Figure 3.9b) and Figure 3.10a, e), Kapton (polyimide film) (Figure 3.10b), Glass (Figure 3.10c), LCP (Liquid Crystal Polymer) (Figure 3.8) and copper cladded LCP substrate (Figure 3.10d, g), are utilized respectively, demonstrating the wide compatibility to virtually every substrate. Among them, PET, Kapton, and LCP are flexible polymer sheets, and the microfluidics devices fabricated on them exhibit outstanding flexibility in both bending directions as shown in Figure 3.10d, e. As a proof-of-concept demonstration, a microfluidics channel printed on 184μm-thick copper cladded LCP substrate was tested with a TestResources four-point bend tester as shown in Figure 3.10g. Minimal bending radii achieved without damage are 7 mm in tension and 6 mm in compression. The microfluidic device was bent to a radius of 1 cm for 1000 times in tension and 1000 times in compression (2000 times in total) without any damage. It has to be stressed that the process is not limited to the substrate while the flexibility largely depends on the substrate flexibility and thickness. For the same microfluidics structure, a better bending capability may be achieved by using a more flexible and thinner substrate. When detached from the substrate, the printed microfluidics devices can be bent down to at least 0.5 mm bending radius, as shown in Figure 3.10f. However, as the detached microfluidics devices are extremely thin, they could be very fragile and hard to handle. Overall, the fully inkjet-printed microfluidics show excellent flexibility for applications such as wearable sensors.

The microfluidic devices are constructed using a single material, SU-8, which is an excellent material for microfluidics[93]. SU-8 features an outstanding chemical resistance and biocompatibility[94] which enables numerous chemical and biomedical applications. The high optical transmittance of SU-8 also enables transparent microfluidics devices for easier channel observation and optical applications[95]. The transparency of the SU-8 thin film is above 90% at visible light range[87]. Caution needs to be paid in the exposure amount in the step of crosslinking the SU-8 as over-exposed SU-8 usually features a brown

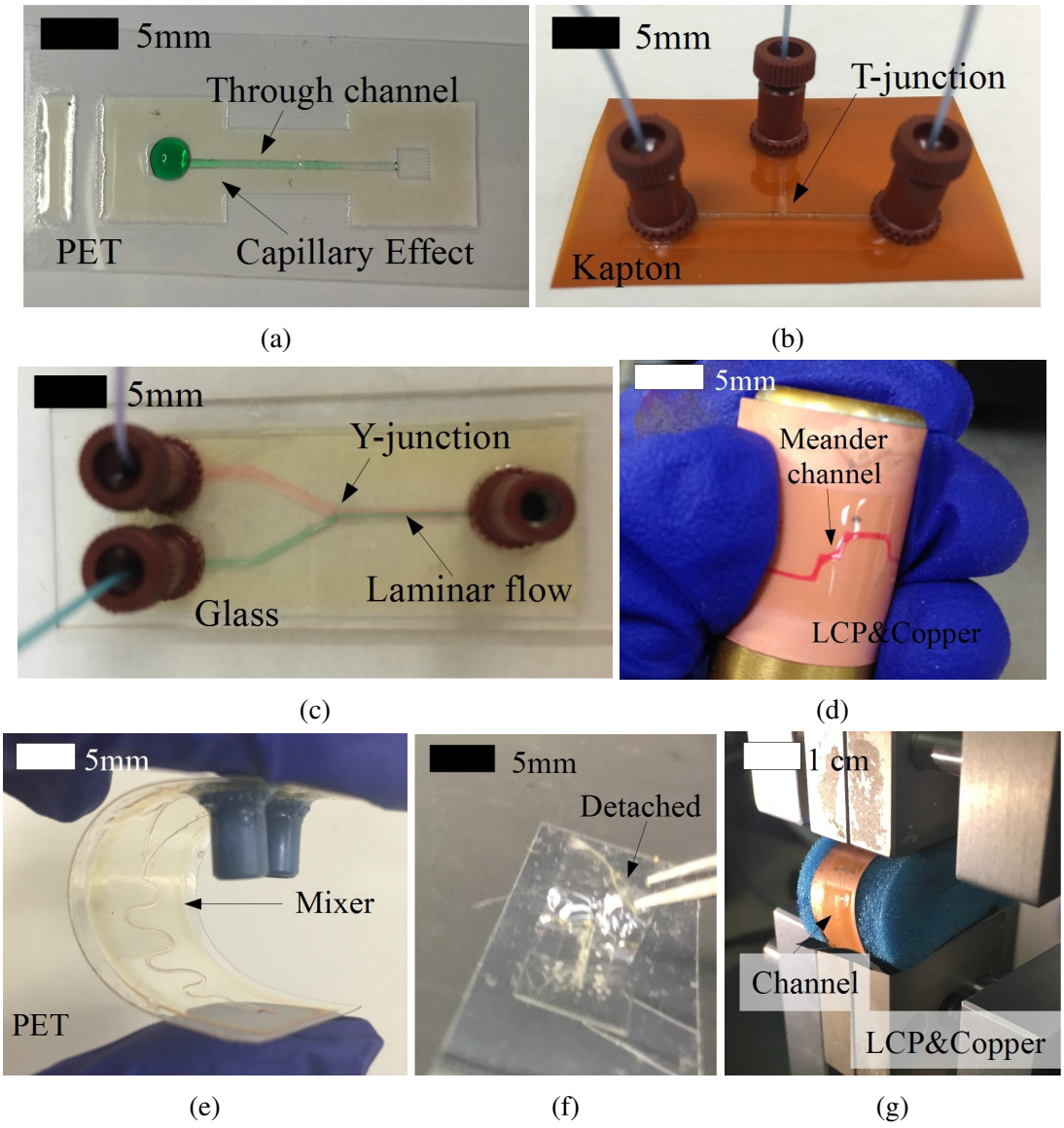

Figure 3.10: Examples of fully inkjet-printed microfluidics structures.
(a) A straight microchannel on PET substrate. A drop of green-dyed water was dripped on one of the two channel openings, and the capillary effect drove the water to enter the channel. (b) A T-junction and three microfluidic channels along with three installed connectors on Kapton substrate. (c) A Y-junction and three microfluidic channels along with three installed connectors on the glass. One of the two inlets was fed with green-dyed water, and another inlet was fed with red-dyed water. A laminar flow appeared when the two different color-dyed flows merged. (d) A meander microchannel on LCP substrate (coated by copper) bent in tension around a 14-mm-diameter rod with red-dyed water filling the channel. (e) A fully inkjet-printed microfluidics mixer on PET substrate bent in compression between two fingers. (f) A microfluidic device was detached from the substrate and was bent by a tweezer for a radius down to 0.5 mm. (g) A microfluidic device was bent by a TestResources four-point bend tester for a radius of 1 cm.

color as shown in Figure 3.9(b), which may affect its transparency. Due to the hydrophobic property of the SU-8, the microfluidic performance of fluid (water-based) is very similar to the PDMS channels.

3.1.5 Fully Printed Paper Microfluidics and Electrical Sensor on Filter Paper

Electronics on filter paper

Inkjet-printing has been already extensively utilized in fabricating electronics such as antennas and passive elements[54, 96, 97, 98, 99]. By inkjet-printing conductive nanoparticles, conductive traces which typically enable electrical sensing can be easily fabricated. However, printing on porous substrates, such as paper, can be challenging as the ink will flow into the substrate, instead of remaining on the top of it[100]. Therefore, as shown in Figure 3.11b and 3.11d, ink deposited on one side can be clearly seen from the other side and spreads out randomly along the paper fibers, which limits the resolution of the printing. Printing conductive nanoparticles can be even more troublesome as nanoparticles may be separated by paper fibers during sintering, which leads to a decrease in the conductivity. In Figure 3.11e, the sheet resistance of the directly printed conductive traces on filter paper or PH strip is over ten times larger than those printed on smooth non-porous surfaces.

There are two ways to resolve this issue. The "passive" way involves the deposition of an increasing number of layers until the saturation of the substrate so that any additional ink will start accumulating on the top of the paper. In Figure 3.11e, an acceptable sheet resistance of 0.1 Ω/square is achieved when more than seven and five layers of ink have been deposited on the filter paper and the PH strip, respectively. The "active" way is the inkjet-printing of a thick layer of SU-8, which will fill the porous space and form a smooth surface, followed by the inkjet-printing of a silver nanoparticle ink on top of the SU-8, resulting in a much better resolution compared to direct printing on paper. A very high conductivity (0.01 Ω/square sheet resistance) can be reached with only three layers of silver nanoparticles ink with sufficient SU-8 deposited and cured first, which is comparable to

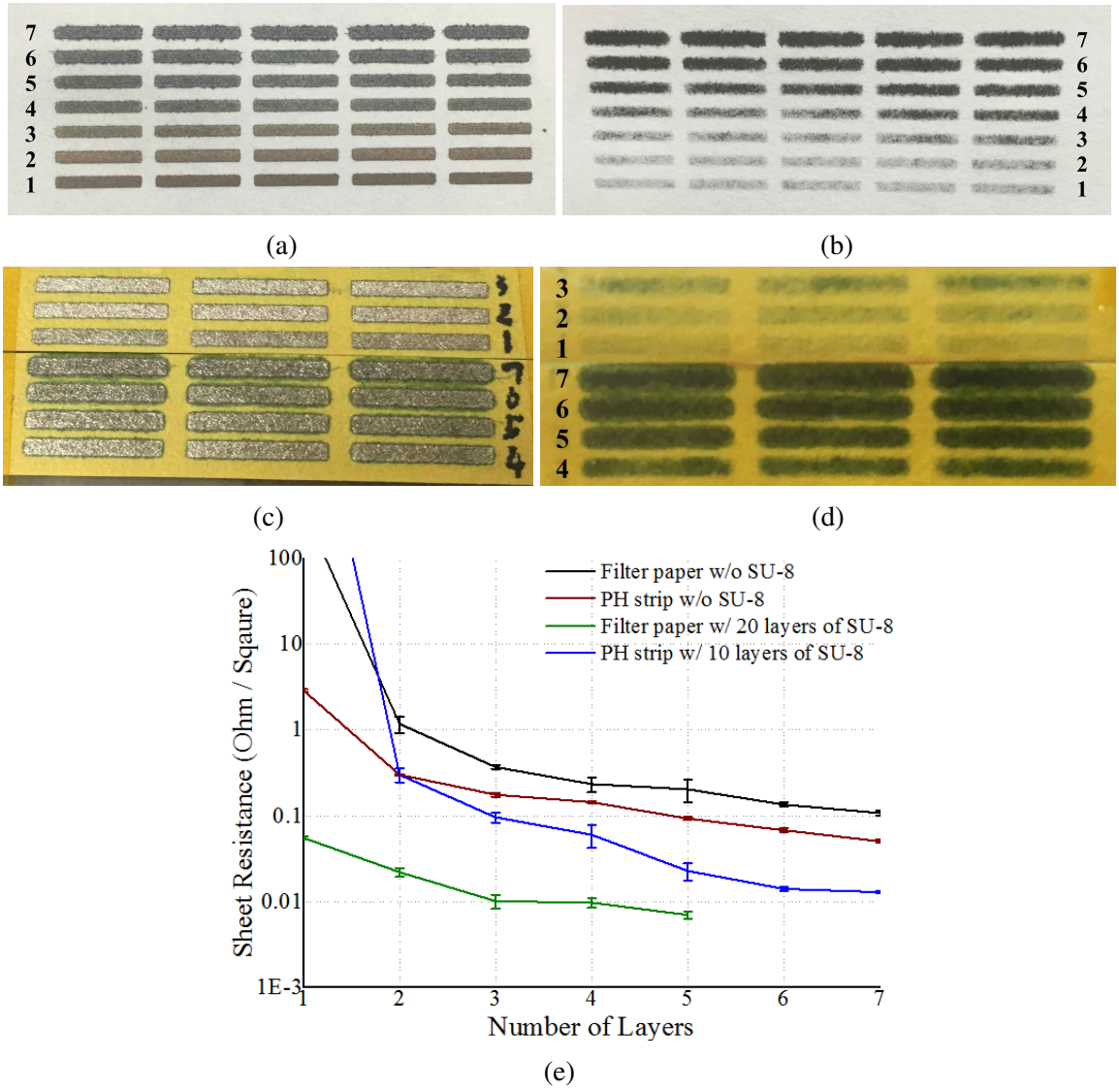

Figure 3.11: Inkjet-printed conductive layers on paper.
(a, b, c, d) Photos of front (ink deposited side) (a, c) and back (b, d) of different number of layers of silver traces printed on the filter paper (a, b) and PH strip (c, d). (e) Average measured sheet resistance for different number of layers of silver printed on filter papers and PH strips with and without printed SU-8 isolation layers, along with the error bars showing the standard deviations of 20 replicas that were measured 10 times each.

the case of regular smooth non-porous substrates. In Figure 5.2a, the sensors were printed on SU-8 to maximize the printing resolution while the antenna and routing were printed directly on the filter paper to simplify the process, while in Figure 5.2b, all conductive parts were printed on 20 layers of SU-8 to achieve the best resolution.

Microfluidics on filter paper

As shown in Figure 3.12a, two different microfluidics can be printed on filter paper: paper-microfluidics, which use paper as a propagation medium (”in-the-paper”) and only have two sidewalls to constrain the liquid, and regular stand-alone microfluidics, in which the channel is on top of the substrate (”on-the-paper”) and is fully sealed in all four directions. Paper microfluidics is the reason why microfluidics and electronics on filter paper are especially attractive. For paper-microfluidics, wax printing is one of the most common fabrication methods[67]. As an alternative, other hydrophobic materials such as SU-8, have been deposited and patterned by photolithography to fabricate paper-microfluidics[101]. Here, we propose inkjet-printing SU-8 to fabricate the paper-microfluidics, an approach that features much lower cost than the photo-lithography method and a better resolution compared to wax printing. Figure 3.12b shows the liquid-proof performance for different numbers of printed SU-8 layers demonstrating that ten layers of SU-8 are sufficient for water while 20 layers are needed for ethanol. The leftmost column was tested with red-dyed water drops, and the other two columns were tested with blue-dyed ethanol drops. Water leakage occurred for five layers of printed SU-8, while ethanol leakage can be found in the case of less than 20 layers printed.

Furthermore, not “in-the-paper” but “on-the-paper” stand-alone microfluidics can be easily fabricated by inkjet-printing, which feature a better control of the volume of liquid inside the channel that plays a very significant role in electrical sensing. I adapt the inkjet-printing method introduced in section 3.1.4 to fabricate stand-alone microfluidics structure on porous substrates, such as filter paper. 15 layers of SU-8 were printed to isolate the stand-alone microfluidics from the paper, followed by ten layers (about 45 μm) of PMMA

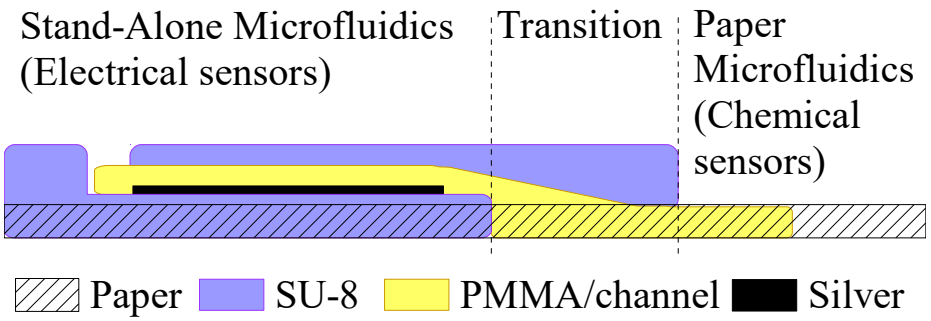

(a)

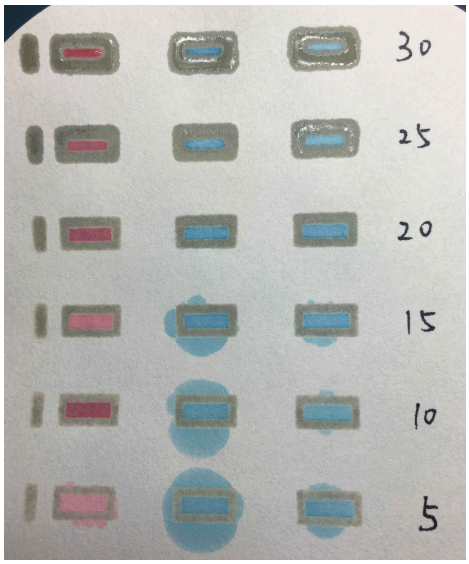

(b)

Figure 3.12: (a) A drawing of the cross-section view of two types of microfluidics and their transition. (b) Different numbers of inkjet-printed layers of SU-8 rectangular rings for paper-microfluidics.

printed as a support material to effectively define the channel position and configuration. Then, an additional 15 layers (about 90 μm) of SU-8 were printed on top and cured, with the fabrication finalized by the PMMA being washed out by anisole bath.

For the transition between the two types of microfluidics, a 2-mm-length PMMA trace directly on paper and a 1-mm-length SU-8 layer to partially cover the PMMA trace are inkjet printed. In this case, the opening of the stand-alone microfluidics channel would be in contact with paper, as shown in Figure 3.12a, and due to the liquid nature of the ink, a gentle and smooth slope would be formed automatically over the step, which efficiently leads the flowing liquid to the paper while not blocking the fluid into paper-microfluidics. To have a smooth transition between the paper-microfluidics channel and the stand-alone microfluidics channel, the PMMA configuration was chosen to be consistent with the stand-alone channels, while the SU-8 configuration was similar to the one used in the paper-microfluidics structures.

Filter paper electrical characterization

To successfully design antennas on the strip, the material properties of the filter paper were characterized up to the wireless frequency ranges with the T-resonator method[102] and the two transmission lines method[103]. Firstly, the "through" propagation phase difference between the two different-length microstrip lines on a 5-layer-stacked filter paper (Fig. 3.13a) was measured with a R& H VNA, which was used in calculating the permittivity over a wide frequency range based on the equations in [103]. Moreover, a T-resonator, as shown in Fig. 3.13b, was characterized around 2.4 GHz to calculate the permittivity and the loss tangent of the filter paper based on [102]. The permittivity of the paper is shown in Fig. 3.13c while the loss tangent was calculated to be 0.036 at 2.4 GHz. Both values are obviously low compared to other paper types (e.g., photo papers) characterized over the same frequencies[104, 105, 96] that feature permittivity values above 3 and loss tangent values above 0.06, which is very likely due to air filling in the porous structure of the filter paper.

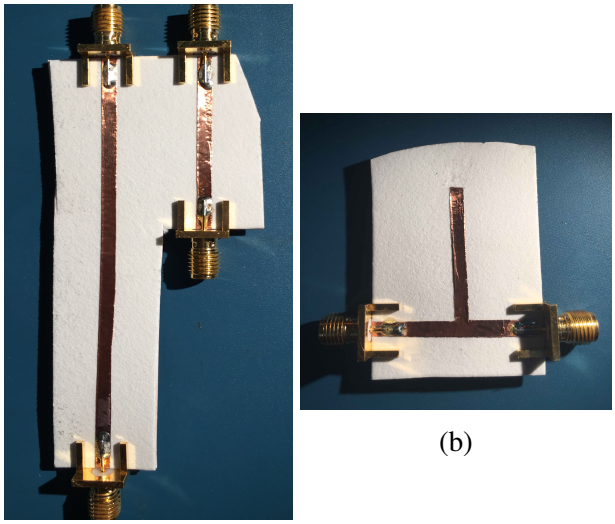

(a) (b)

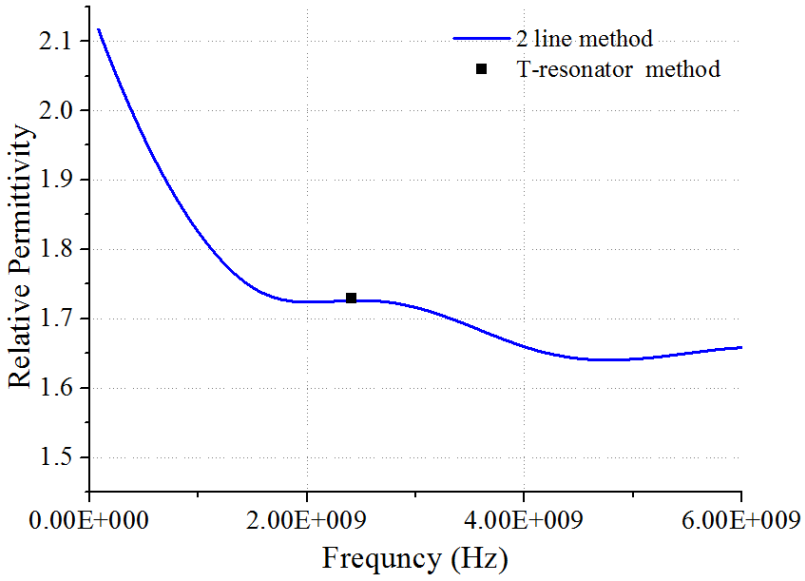

(c)

Figure 3.13: (a) Two microstrip lines on filter paper to characterize the substrate. (b) A T-resonator working at 2.4 GHz utilized for filter paper calibration. (c) Measured permittivity vs frequency using the two methods in (a) and (b).

3.2 3D Printing

In the recent decades, 3D printing has attracted an increasing amount of attention, as it can create complex 3D objects directly from computer-aided design (CAD) files without any need for assembly saving production time and cost[106]. Under this concept, different printing technologies have been developed, including fused deposition modeling (FDM), stereolithography (SLA), and Selective Laser Sintering (SLS), all with their own advantages and disadvantages in different applications. In this chapter, I explored FDM printing, SLA printing, and DLP printing for direct printing microfluidics-integrated electronics along with several selective or massive metalization approaches.

3.2.1 FDM Printing

FDM, the most accessible and economical printing method is chosen for its ability to fabricate water-tight microfluidic channels without any support structure[107]. A $399 Printrbot Play was used, allowing high-resolution prints with 100-μm layer height and 0.4 mm minimum feature sizes out of the box. In order to reduce z-axis artifacts with FDM printing, it is best to print at a layer that is a multiple of the full-step size of the stepper motor (1.8 degree motor step angle, 16 micro steps to full step) in relation to the pitch of the z-axis threaded rod (1.5875 mm for 1/4" Acme rod), resulting in a minimum layer height of .127 mm for 1 full step. Supports for prints can be printed using multi-material printers with a dissolvable material, or single material printers can generate support structures, but both support structure can be hard to remove from small cavities and channels. Therefore, a microfluidics device without support material was printed with low overhang angles and short bridges.

To make the print water-tight, over-extrusion is exploited to create a non-porous print in addition to printing at higher temperatures to increase layer-to-layer adhesion. The printing was set with an extrusion multiplier of 1.15 (15% additional material per calculated

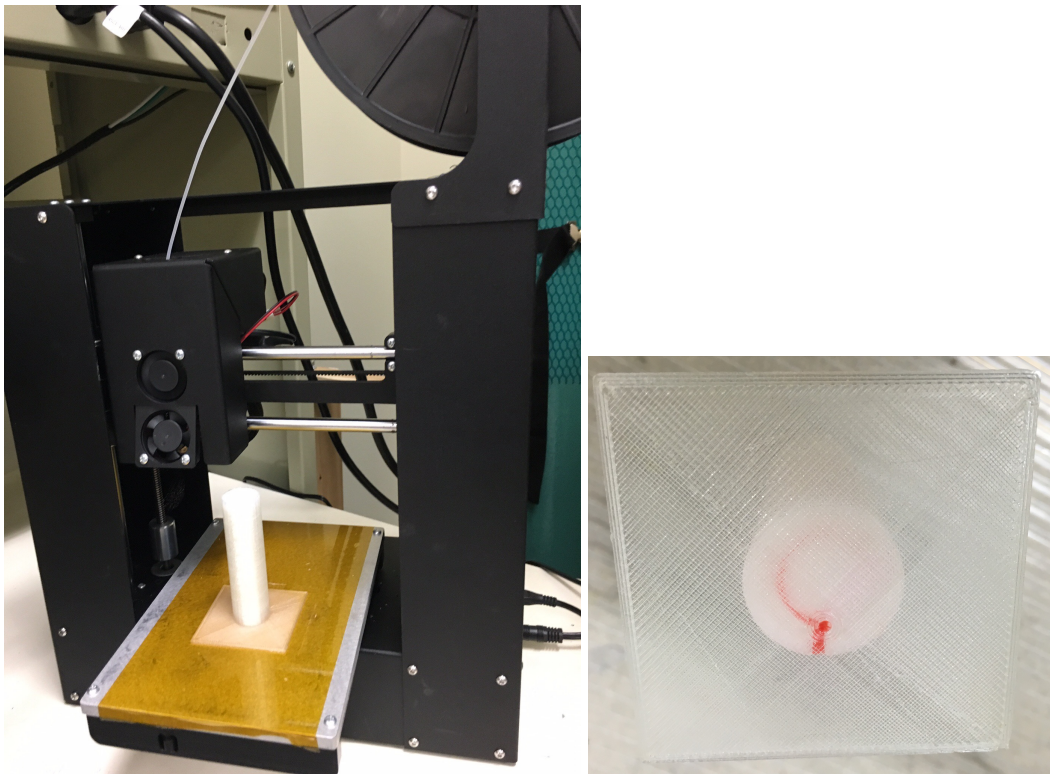

(a) (b)

Figure 3.14: Photo of a FDM 3D printed microfluidics-enabled helical antenna (a) in a FDM 3D printer and (b) in a bottom view while filled with red-dyed water.

volume of material needed) at 235°C while normal suggested print temperature range is 210-220°C). With these parameters, a low-cost microfluid structures can be printed rapidly. The transparent NinjaFlex filament was chosen because its excellent flexibility and transparency when printing thin objects and great waterproof performance when printing thicker layers, but the similar setup likely applicable to a variety of FDM thermoplastic materials. NinjaFlex features a 3.0 dielectric permittivity and 0.06 loss tangent[107]. Figure 3.14a shows a microfluidics-enabled helical antenna was printed on a Printrbot FDM 3D printer. Texture, which is one of the well-known FDM printing drawbacks, can be easily observed in Figure 3.14b. The red-dyed water in Figure 3.14b also shows the device achieves an acceptable water-proof capability.

3.2.2 SLA Printing

A stereolithography (SLA) 3D printer, FormLabs form 2, which features 50 μm spacial resolution, was used to print 3D microfluidics channels. SLA printing technology is using a moving ultraviolet (UV) laser beam to selectively cure/solidify photo-polymer patterns layer by layer. The 3D model was defined by a 3D CAD STereoLithography file (.stl) with support structure added. According to the .stl file, the SLA printer can cross-link the photopolymer resin with a 140-μm-beam-width (FWHM) and 250-mW-intensity laser. After printing, the printed prototype was immersed in the isopropyl alcohol (IPA) for several minutes to remove any uncured resin, following by a UV exposure with bath in water to thoroughly cured the structure.

For flexible design, FormLabs flexible resin (FLGR02), a black rubber-like photopolymer featuring 80% elongation, was an excellent candidate and was characterized with both the two line method (Figure 3.15a) and the T-resonator method (Figure 3.15b). A permittivity around 2.8 with loss tangent around 0.06 from 1 to 8 GHz can be found in Figure 3.15c.

Flexible 3D SIW transmission line

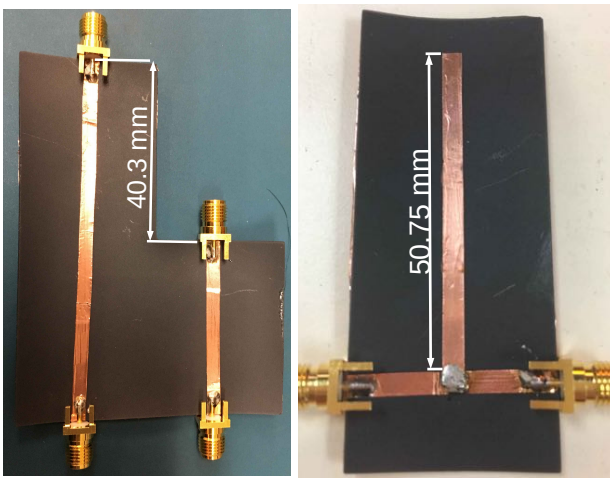

(a) (b)

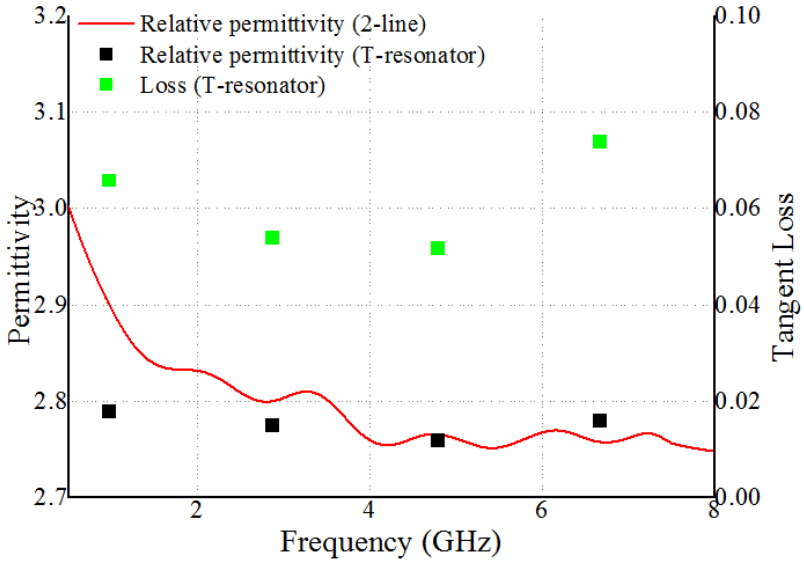

(c)

Figure 3.15: (a, b) 2 microstrip lines (a) and a T-resonator (b) for FLGR02 material characterization. (c) Relative permittivity and loss tangent characterization results up to 8 GHz.

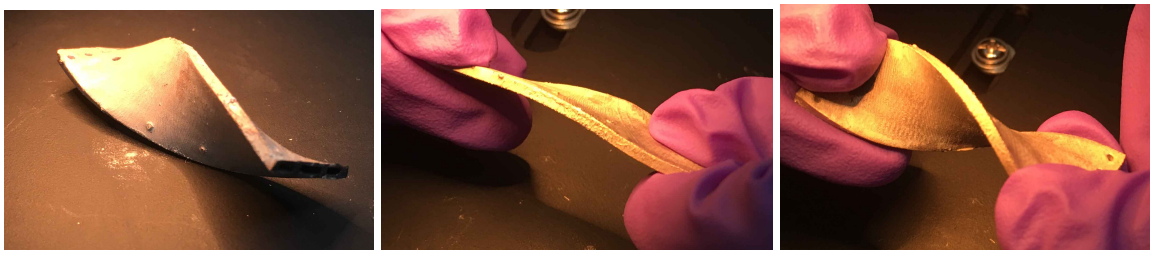

(a) (b) (c)

Figure 3.16: Photo of the twisted SIW in various states: (a) original (120° twisted); (b) flat (0° twisted); (c) 180° twisted.

Abnormal and complex shape 3D objects can be easily printed by 3D printing techniques. An excellent use case is wearable devices in which on-demand customized capability is highly preferable. By printing flexible materials in optimized 3D configurations, the resulting devices can achieve excellent stretchability and twist-ability. For example, 3D printed customized substrate integrated waveguide (SIW) structures for flexible and high-performance wearable designs are shown in Figure 3.16 and Figure 3.17. Figure 3.16 shows a twisted SIW transmission line prototype enabling 0° to 180° twisting without any damage, demonstrating the great flexibility of the design. In Figure 3.17, a wave-like SIW can be compressed to less than 4 cm and be stretched to more than 9 cm without cracks, featuring excellent stretchability/compressibility. SIW or dielectric-filled waveguide structures are known for high performance in higher frequencies as they can eliminate the radiation loss, provide perfect electromagnetic isolation from the environment and feature a relatively stable performance during bending, thus becoming an excellent candidate to construct wearable microwave devices. Details of the SIW structure can be found in chapter 4.3. The SIW prototype was SLA 3D printed with flexible resin and then coated with silver using a simple "bath-and-bake" approach: bath in silver nanoparticle (SNP) ink and bake at 120°C for an hour in the oven. This "bath-and-bake" approach can massively metalize the exterior surface of the 3D object, while selective metalization methods are discussed in section 3.2.4.

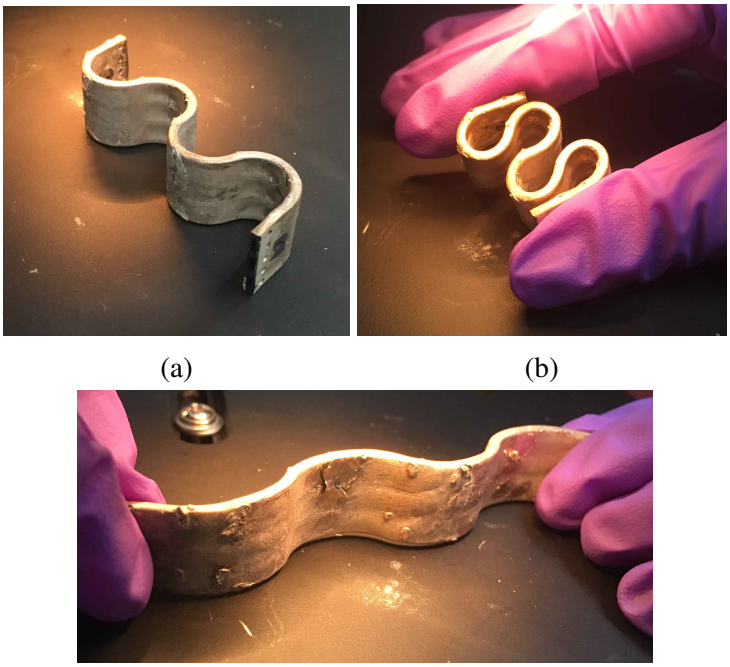

(a) (b)

(c)

Figure 3.17: Photo of the wavy SIW in various states: (a) original (6.71 cm length); (b) compress (4 cm length); (c) stretched (9 cm length).

3.2.3 DLP Printing

Similar to SLA printing, digital light processing (DLP) 3D printing can be used in printing similar structure with higher speed. A Little RP printer with the projector was used as shown in Figure 3.18c. The printer features 60 mm$\times$40 mm$\times$100 mm(height) build volume and approximate 2 minutes/mm printing speed. The projector used is a Viewsonic PJD7820HD featuring 1920$\times$1080 resolution. DLP printing uses the projector to project the light pattern of a layer at once. On the one side, this approach leads to high printing speed comparing to SLA printing. On the other side, due to the lens in the projector, while the center of build plate is in focus, the edge of build plate might be out of focus, which might lead to a blurry boundary of the pattern and uncured due to less exposure energy. Moreover, due to the limited resolution of the projector, the maximum build size is resolution times pixel size. Thus the DLP printer might have either a small building volume or a large pixel size. For SLA and DLP transparent resin, one crucial thing to keep in mind is

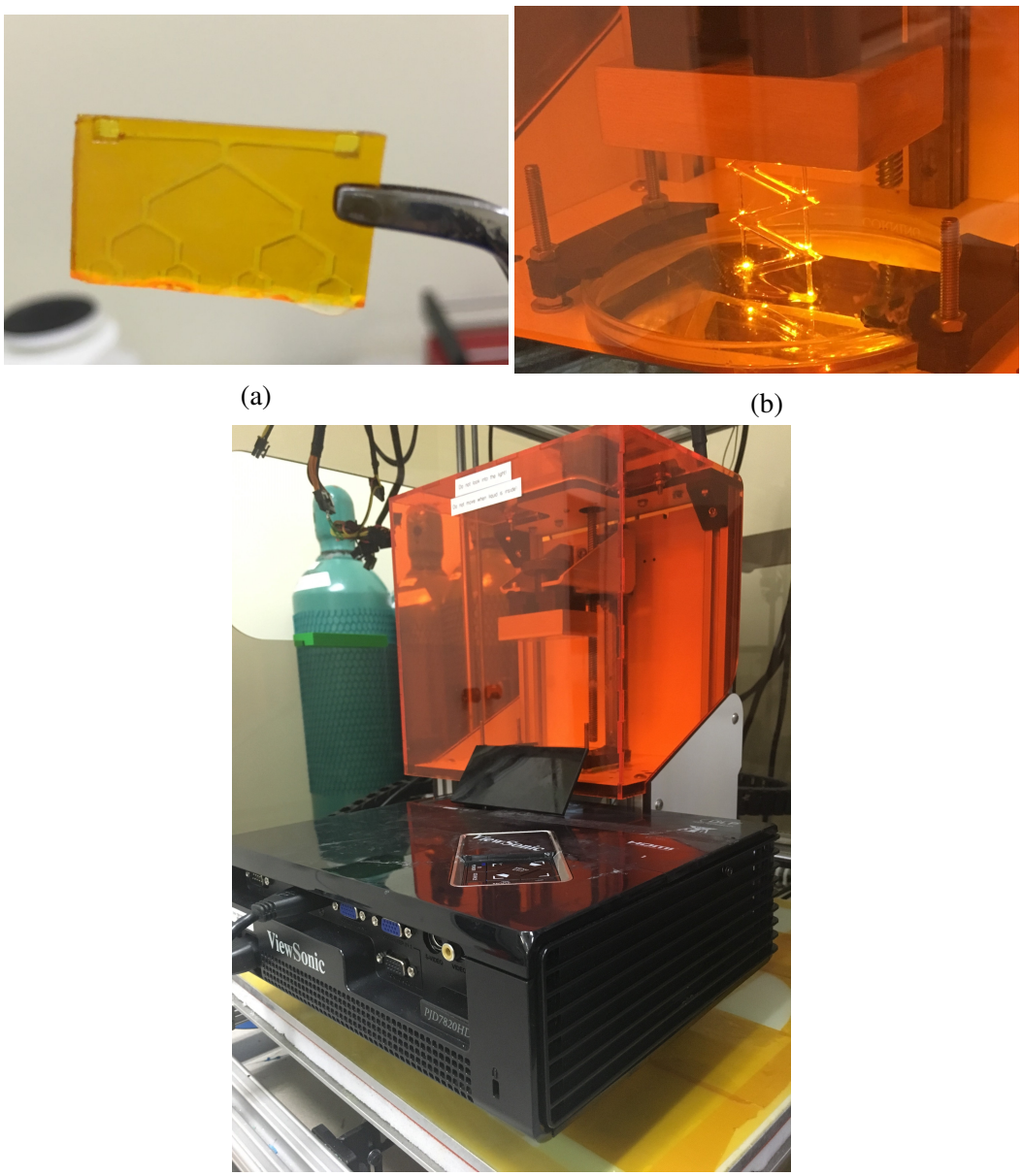

(a) (b)

(c)

Figure 3.18: Photos of (a) a FDM 3D printed microfluidics mixer, (b) a zigzag channel for zigzag antenna in printing, and (c) the DLP printer used.

that, due to the transparency of the resin, UV light used to cure the bottom layer may pass through the bottom layer and partially cure the upper layers that should be cured, which might lead to a thicker bottom layer than the designed one. Regarding microfluidics, this over-cure effect usually results in a channel with correct x and y dimension, but smaller z dimension (height) or correct z dimension but a troublesome resin cleaning process as the resin in the microfluidic channel is partially cured. A solution of this issue could be designing the z dimension with the consideration of overcured and using UV blocker to change the UV absorption curve.

3.2.4 Selectively 3D Metalization

Due to its simplicity in printing light-weight complex-shape 3D objects, 3D printing, especially low-cost dielectric 3D printing, has been involved in the fabrication of antennas and microwave components recently. However, due to the challenge of selectively metalizing the dielectric 3D objects, most prior efforts have focused on structures that are fully coated with a metal such as horn antennas and waveguides. With the three different selective metallization techniques discussed below, more interesting complex shape 3D microwave components and systems with a larger amount of variety can be fabricated.

Liquid metal alloy

Liquid metal alloy (LMA), especially Eutectic Gallium-Indium (EGaIn), features a great potential in reconfigurable electronics due to its non-poisonous, high-conductivity, flow-able and stretchable properties [31]. With the help of microfluidics, a tool that allows the manipulation of small amounts of liquids, LMA can be transferred within structures of various shapes [108, 109]. Furthermore, unlike all solid materials, due to its liquid nature, LMA ensures a “never-fail” bending and self-healing even if cracks occur under extreme folding conditions, which facilitates the realization of rugged flexible/compressible LMA antennas.

The LMA used is EGaIn (Sigma-Aldrich, 495425), an alloy with 75%wt Gallium and

25%wt Indium, which features a 15.5 °C melting point and a $29.4 \times 10^{-6}\Omega\times$cm resistivity that enables high-performance electronic designs [31]. The bulk viscosity of EGaIn is 1.9910 mPa*s (twice of water, one 4000th of ketchup), which enabling trouble-less flowing in the channels. Moreover, unlike mercury, EGaIn is non-toxic and very healthy. The only concern of EGaIn is that Gallium quickly oxidizes when exposed to air, an effect that could prevent the proper flow of LMA and might affect the conductivity of the LMA. To dissolve/avoid the oxidation skin of the EGaIn, a sodium hydroxide (NaOH) solution was circulated inside the microfluidic channel before the filling with EGaIn. To accurately control the flow of LMA, microfluidics pumps are needed to inject and withdraw LMA to/from the channels.

Chapter 6 discusses in detail the microwave designs and examples utilizing liquid metal alloy in 3D printed objects.

Semi-additive process

A semi-additive process (SAP), which is widely used in packaging and Print Circuit Board (PCB) fabrication, was adjusted for additive manufacturing to selectively metalize the 3D printed prototypes, as shown in Figure 3.19. Firstly, the prototypes were sputter coated using a thin layer of Titanium as the bonding layer and then a 400 nm copper layer as the electroplating seed. Then, instead of photolithography in a traditional SAP process, inkjet-printing, an additive manufacturing process, was used to deposit a 20 μm Poly(methyl methacrylate) (PMMA) mask to prevent the contact of the electrolyte and the seed layer at the specific areas where copper should be prevented from forming during electroplating. The shape of the mask is designed to be the projection of the negative of the pattern in the printing direction. Multiple prints at different angles can efficiently pattern any outer surface of any 3D prototype. After the mask is deposited on the different faces of the 3D printed object, the prototype is soaked in a copper salt solution with a negative charge which results in copper growth only on areas that are conductive. Approximately 5 μm ofthick copper is deposited in 40 minutes. After that, the PMMA mask is removed via

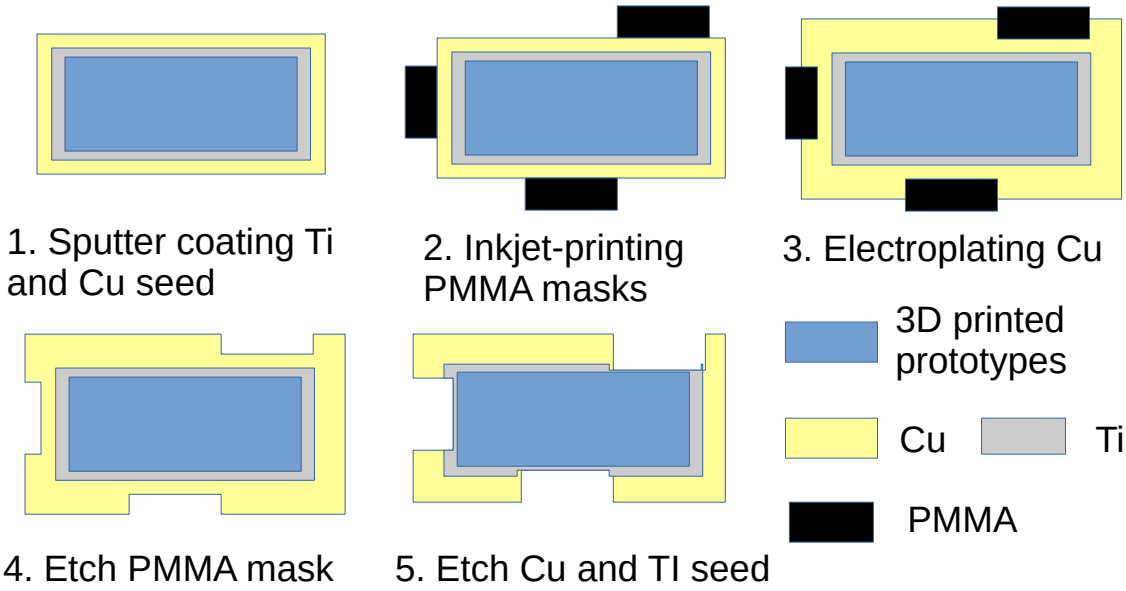

Figure 3.19: Selective 2.5D metallization process with a arbitrary 3D object in a cross-section view.

an acetone bath, and then the copper seed below is etched with the copper etchant in a carefully controlled time to prevent over-etching of the electroplated copper. Compared to the "bath-and-bake" processes discussed in section 3.2.2, besides the capability to selectively metalize, this approach features a much better uniformity of the conductivity, and a much better bonding strength between prototype and the conductor, which is very important for flexible devices. Within the three selectively metalization methods discussed in this section, this approach features the best resolution but also requires extra equipment such as an inkjet printer,a sputtering machine, and an electroplating equipment.

3D conformal stamp

The metallization can also be realized by using a 3D printed conformal stamp. The 3D printed flexible material, such as Formlabs Flexible resin, can provide a soft surface with great wettability that would be necessary for high-quality stamping. The pattern to be stamped is 1mm higher than the unpatterned section of the stamp and 0.1 mm higher on the dielectric structure so that the pattern with ink can be easily transformed from the stamp to the dielectric without touching the unpatterned surface. Compared to regular stamps, this

3D printed stamp can be made conformal to any surface, including curved surfaces and corners as shown in Figure 3.20, which enables metalization on any arbitrary 3D object surface.

Figure 3.20a and Figure 3.20b show the stamps for a spherical patch antenna and a power divider, respectively. Rectangular posts are printed on the dielectric spherical structure for proper alignment as shown in Figure 3.20c. The proof-of-concept ink used for the stamp is LPKF proconduct paste. However, any conductive ink can be used for stamping. The interior of the top hemisphere and the phase delay lines were fabricated by simply depositing and coating with the same silver paste as no pattern is needed. The ink was cured at 80°C for 1 hour, and 0.06 Ohm/square was achieved. The fabrication of both the 3D dielectric object to be metalized and the metallization stamp is carried out by the same 3D printer, which can largely simplify the process and decrease the cost. Compared to the other two methods in this section, this approach is excellent for the low-cost production of a significant amount of pattern on curved surfaces.

3.3 Summary

This chapter introduces the AM fabrication process for microfluidics electronics by characterizing the ink used in inkjet printing, discussing three inkjet-printing processes for microfluidics electronics and a special process for filter paper, and demonstrating three dielectric 3D printing techniques adopted for microfluidics electronics and three selectively metalization methods to metalize the 3D printed objects. With these AM process, microfluidics electronics, especially microfluidics sensors and liquid reconfigurable microwave components can be fabricated at a low cost on demand, which enables numerous wireless liquid sensing and IoT applications. The fabrication process introduced in this chapter are compared in Table 3.2.

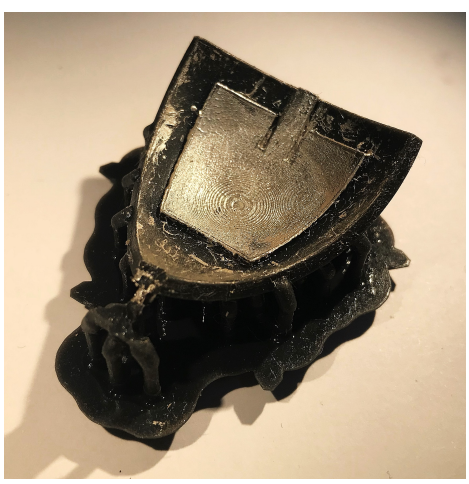

(a)

(b)

(c)

Figure 3.20: 3D printed comformal stamp. Photos of (a) the stamp for the spherical patch antennas, (b) the stamp for a power splitter utilized in the antenna array, and (c) stamping both stamps for a composite antenna array topology.

Table 3.2: Comparison of demonstrated AM processes for microfluidics electronics in Chapter 3

Process	Inkjet Printing			3D Printing		
	Bonding	Molding	Fully printing	FDM	SLA	DLP
Printing setups						
Printer	Fujifilm Dimatix DMP-2831			Printrbot	Formlabs 2	Little RP
Assistant techniques	Laser etching	soft-lithography	None	Metallization methods (e.g. LMA, SAP, stamp)		
Microfluidic channel						
3D	Possible	Possible	Yes			
Height	0.5 mm	>14 μm	>0.8 μm	2 mm	1 mm	1 mm
Width	0.3-1.4 mm	>0.1 mm	>60 μm	2 mm	1 mm	1 mm
Materials	PMMA, SU-8	PDMS, SU-8	SU-8	NinjaFlex	Photopolymer	
Sealing	irreversible	reversible	Not applicable			
Prototypes						
Flexible	Possible	Yes	Yes	Limited	Yes	Yes
Time	1-2 hrs	1-2 hrs	3-4 hrs	2-5 hrs	2-7 hrs	0.5-4 hrs
Examples (section #)	4.1, 4.2, 4.4, 4.6	4.5	4.7, 5.1, 5.2.1	6.1	4.3, 5.2.2, 6.2, 6.3	-

CHAPTER 4
RF SENSORS AND RECONFIGURABLE MICROWAVE STRUCTURES BASED ON MICROFLUIDICS

In order to realize reconfigurable RF sensors and microwave components, different microwave structures with embedded microfluidics including patch antenna, loop antenna, slot waveguide antenna, split ring resonator, dual-spiral slot resonator, dual T-resonator, microstrip line, and step impedance low pass filter, are studied in this chapter.

4.1 Coplanar Patch Antenna

The patch antenna is chosen due to its strong E field in the gap between patch and ground so that the resonant frequency of the patch is very sensitive to the permittivity change in the gap, which is excellent for embedding microfluidics. A coplanar patch antenna (CPA) fed by a CPW line is designed, while the microfluidic cavity is set between one of the radiation edges and the ground plane, as shown in Figure 4.1a. Even though CPA has a structure similar to the loop slot antennas, the electric field analysis of CPA demonstrates a behavior closer to the microstrip patch antennas [110]. The phase of the electrical field is the same on the top and bottom slots, while there is a phase change of 180 degrees between the left and right slots, indicating that similar to microstrip patch antennas, CPAs have two radiating edges and two non-radiating edges. The microfluidic cavity is placed on top of the of the front radiation edge (Figure 4.1b), thus changing the working frequency according to the fluid permittivity. In Figure 4.1c, the antenna operating frequency shifts as different liquids fill the microfluidic channel, showing a tuning range of 500 MHz for permittivity changes from empty to water. The simulated and measured radiation pattern results can be found in Figure 4.2, which remain nearly constant over the entire tunable range.

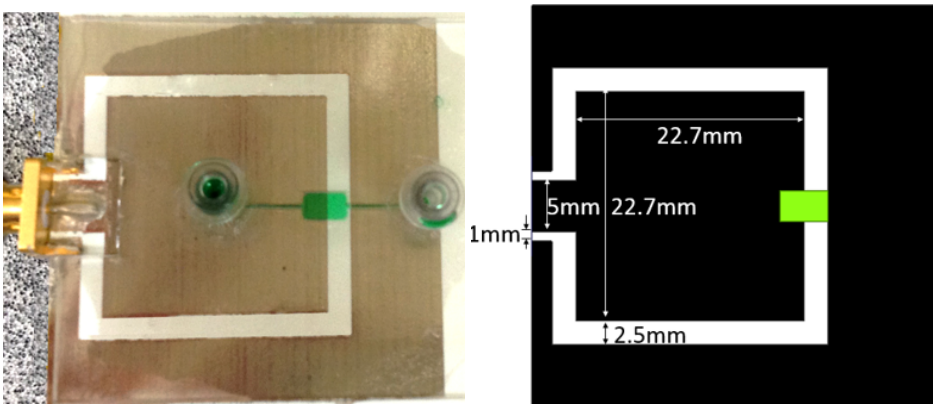

(a) (b)

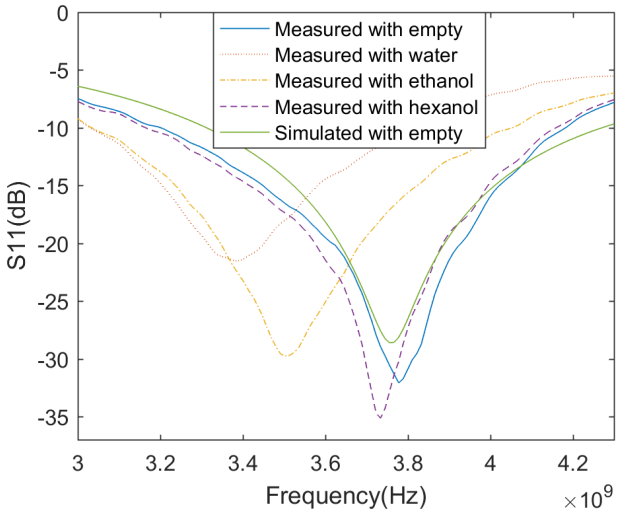

(c)

Figure 4.1: A photo (a) and a drawing (b) of the microfluidics-based tunable CPA along with measured and simulated the return loss in (c).

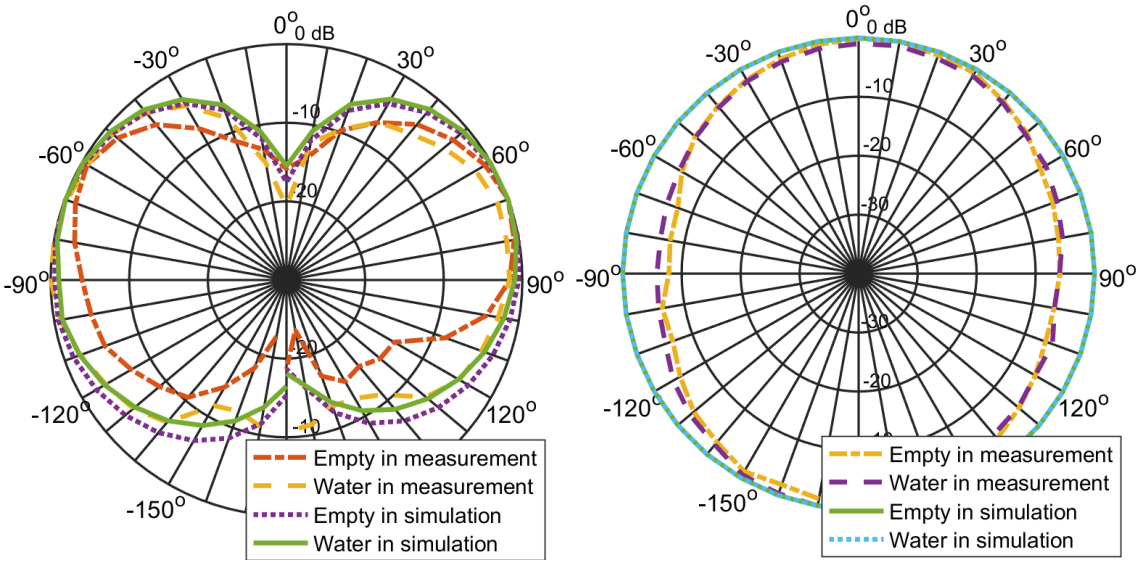

Figure 4.2: Simulated and measured radiation pattern of the microfluidics-based tunable CPA on E plane (a) and H plane (b).

4.2 Loop Antenna with Balun

Loop antenna is a simple wire antenna which doesn't have a strong E field, however, when different fluids fill the channel, the permittivity of the liquids can control the electrical length of the loop, and thus will determine the resonating frequency of the loop. Figure 4.3a shows a square loop designed with a microfluidic channel located right on the top of the loop. A balun is designed to feed the loop antenna with a coaxial cable, which constitutes a power divider and two microstrip lines with a 180-degree phase difference. The microfluidic channel is also placed right on top of the electrically longer transmission line. In Figure 4.4a, the zero imaginary part frequency shift from 2.4 to 2.3 GHz while real parts are around 100 Ohm at zero imaginary part frequencies. Similar to the loop, the permittivity change in the microfluidic channel will lead to a working frequency shift of the balun. The phase difference between two branches is optimized to obtain the same phase difference when liquid filled, as shown in Figure 4.4b. The simulated return loss and radiation patterns are shown in Figure 4.3c and Figure 4.5, respectively. Due to the

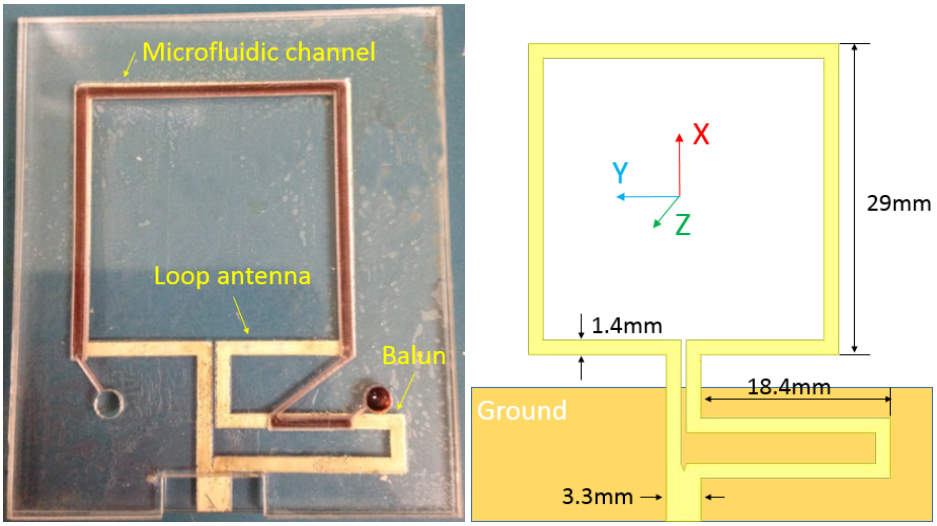

(a) (b)

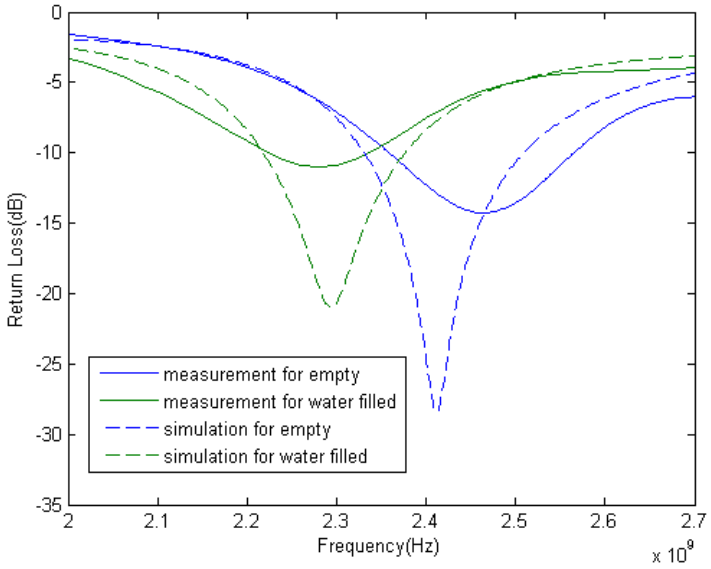

(c)

Figure 4.3: A photo (a) and a drawing (b) of the microfluidics-based tunable loop antenna with a balun along with measured and simulated the return loss in (c).

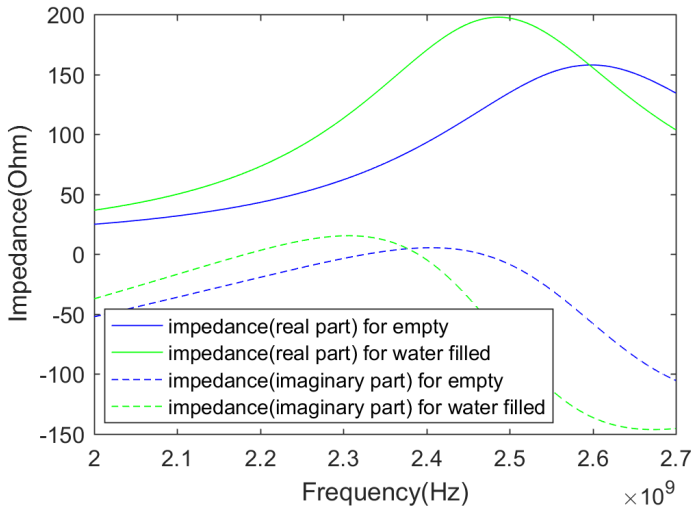

(a)

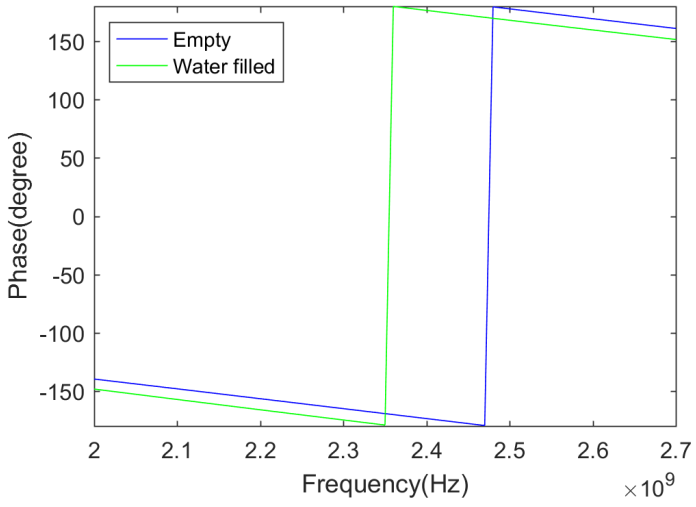

(b)

Figure 4.4: (a) The real part and imaginary part of impedance of the microfluidics-based tunable loop antenna in simulation for empty and water-filled channel. (b) Phase difference between two branches of balun in simulation for empty and water-filled channel.

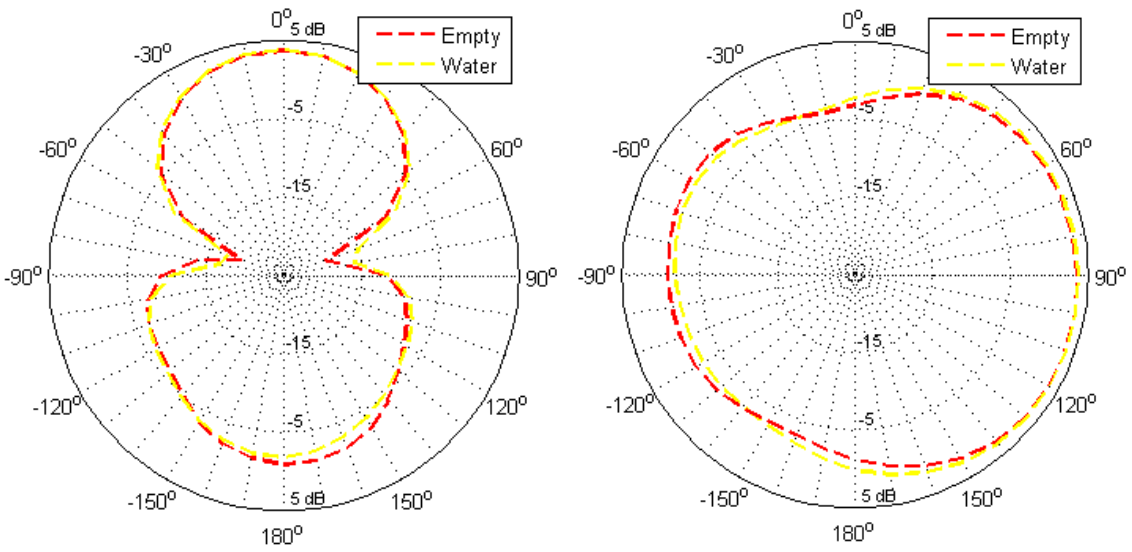

Figure 4.5: Simulated E plane (a) and H plane (b) radiation patterns of the microfluidics-based tunable CPA for the empty channel and the water-filled channel.

influence of the ground plane in the feed circuit, radiation patterns lean up in the E plane and lean to the right in the H plane compare to an ideal large circular loop. A frequency shift from 2.45 GHz (empty channel) to 2.28 GHz (water-filled channel) can be observed, which shows a good agreement with simulation results. This design takes advantage of the relation between phase velocity and permittivity. As this influence is not as strong as slot capacitance and permittivity, the sensitivity is smaller than antenna structures with slots.

4.3 Slot Waveguide Antenna

A slot waveguide structure was used with a microfluidics channel right underneath the slot as shown in Figure 4.6. For different fluids inside the channel, the electrical length of the slot is changing. This sensor is designed for wearable applications: the material used in very flexible so that it can be bent to be conformal to the body and the SIW structure can effectively prevent interference between the human body and the RF signal. The permittivity value of the fluids is varying for different solution contents inside the microfluidic channel, which would potentially provide useful information about the user's health status.

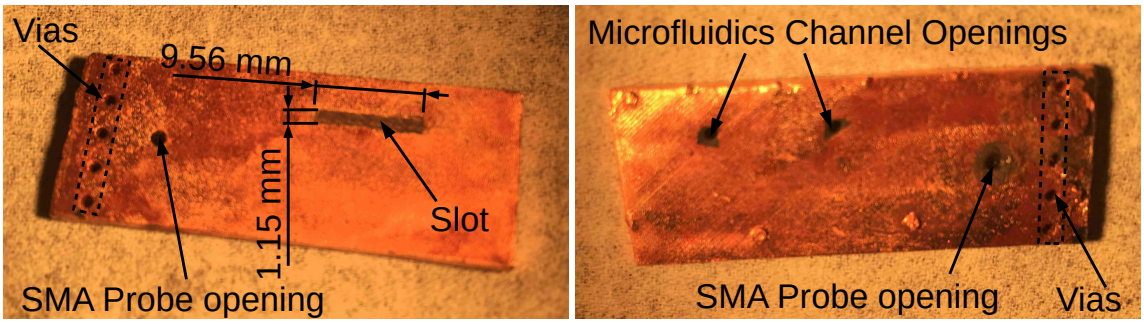

(a) (b)

Figure 4.6: Photo of 3D printed microfluidics sensors.

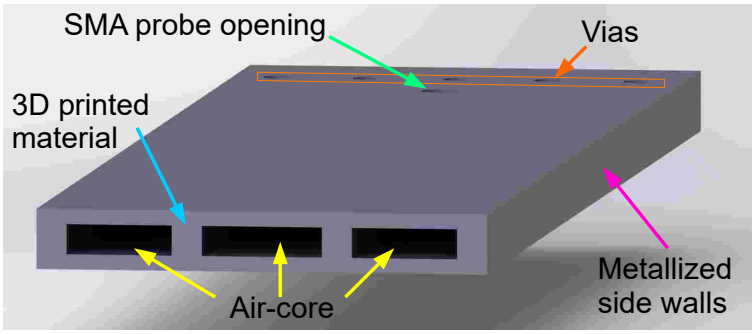

Figure 4.7: Diagonal view of 3D printed air core SIW which is cut in half to show the cross-section of the SIW.

In general, photopolymers feature a high dielectric loss, which would significantly affect the performance. Thus the SIW was designed to have an air core inside, which also decreases the stress of the material when bent and facilitates better flexibility. The presented SIW transmission line uses side walls on both sides to reduce the radiation loss. However, due to the 3D printing constraints, the resin trapped inside the cavity needs to have an opening so that it can flow out. Thus vias are applied to the two ends of the SIW to replace the side walls. The SIW cross-section shown in Figure 4.7 is 2 mm thick in total with a 1-mm-thick air core, and has 15 mm width for 50 Ω impedance matching. Two 1 mm width supportive walls are designed to be located at the 1/3 and 2/3 width positions, effectively preventing the deformation of the structure during bending.

The sensor was measured with an Anritsu VNA for air, ethanol, and water inside the channel. Observing S11 in Figure 4.8, it's easy to notice the resonant frequency is shifted

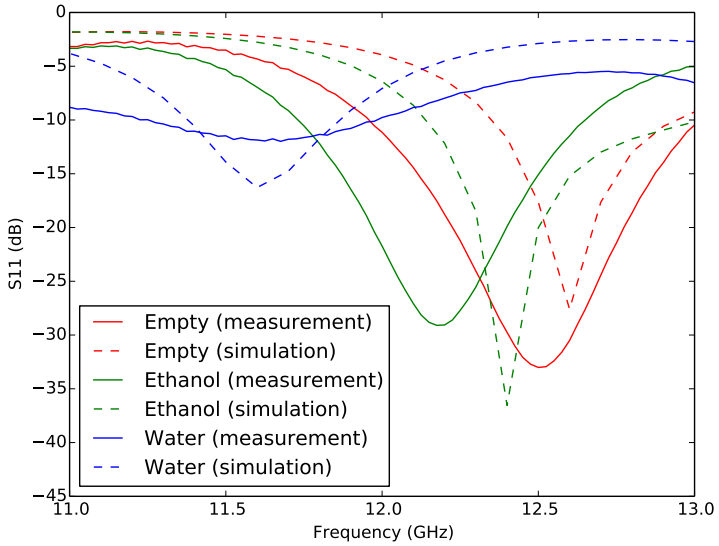

Figure 4.8: S11 of the antenna sensor when different fluids or air filled in channel.

with permittivity while the loss of fluids affects the bandwidth/Q-factor of the antenna. Good linearity can be seen for the sensor as shown in Figure 4.9, and the ethanol variance from simulation and measurement may be due to impurities in the ethanol solution used. In Figure 4.10, the frequency with the maximum slot waveguide gain is also shifted to a lower frequency when filling the underlying microfluidic channel with water, showing that the operation frequency of the antenna was shifted accordingly for different contents of the channel.

4.4 Split Ring Resonator

A tunable band-stop filter, as shown in Figure 4.11a, is designed based on the split ring resonator (SRR), which is a commonly used metasurface unit cell. The SRR unit cell can be modeled as an R-L-C circuit as shown in Figure 4.12a, where R represents a parasitic loss, L is the loop inductance, and C is the gap capacitance. A microfluidic channel can be easily run over the gap in the SRR. When liquids of different permittivity are present over the gap, the capacitance of the gap changes due to changes in the displacement field strength, which leads to a change in the resonant frequency of the SRR. By closely coupling

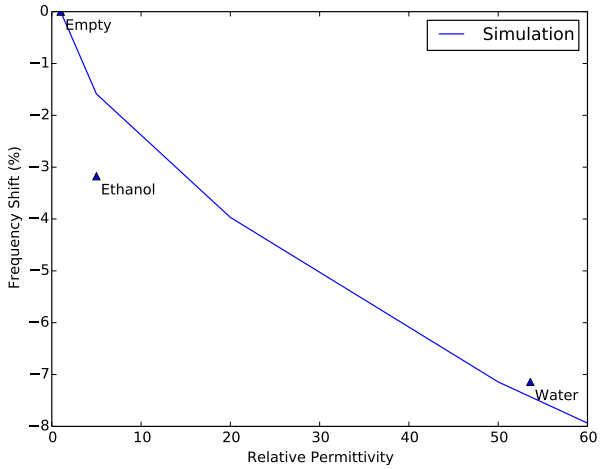

Figure 4.9: The relation between the resonant frequency shift of the sensor and the permittivity value of the material filled in the channel. The line shows the simulation result, and the triangles are the measurement results for empty, ethanol-filled, and water-filled channels.

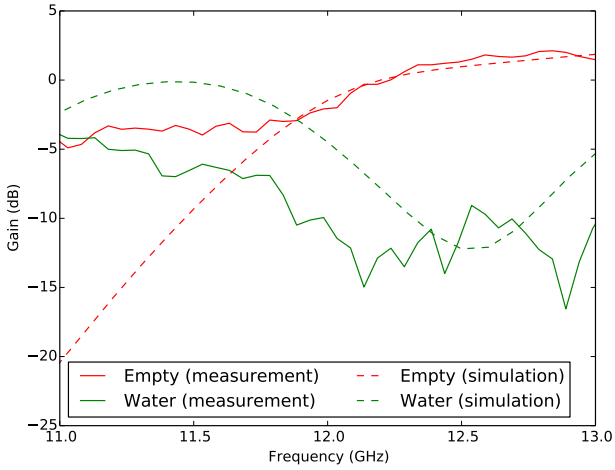

Figure 4.10: Maximum gain of the slot waveguide antenna for the empty channel and the water-filled channel. Due to the dielectric loss of water and impedance mismatching, the maximum gain for a water-filled microfluidics channel is lower than that for an empty channel.

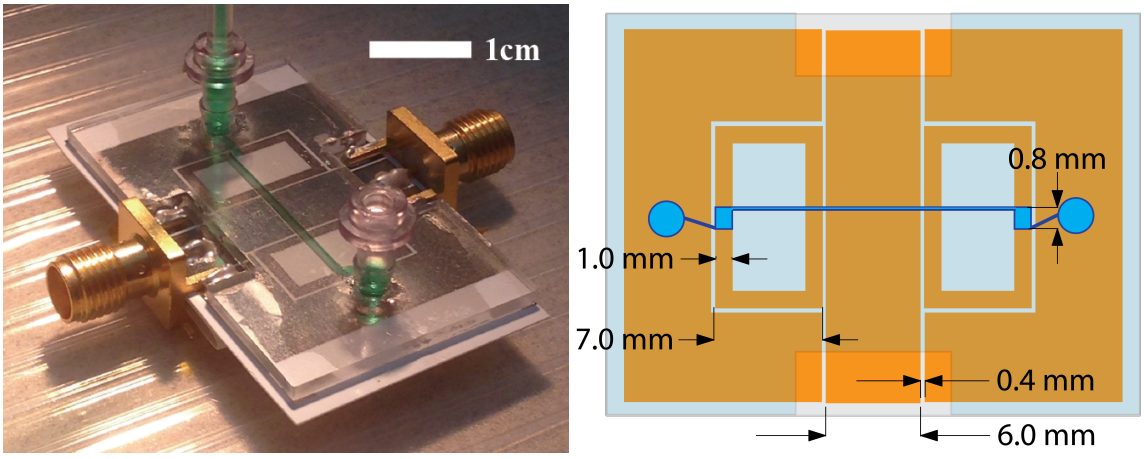

(a) (b)

Figure 4.11: A photo (a) and a drawing (b) of the microfluidics-based tunable SRR band-stop filter.

the SRR to the CPW line, as shown in Figure 4.11b, energy transfer occurs from the line to the resonator near the resonant frequency, which causes a band-stop effect. For the sake of investigating suitable sensitivity, a different slot size is simulated. As shown in Figure 4.12b, sensitivity grows with b, while the strength of resonance is decreasing. The best sensitivity in Figure 4.12b is $0.8\,\%/\varepsilon_r$ when b is $5\,$mm. But the insertion loss for b=5 with water filling is only -6 dB, which shows a limited tunable range. This set of simulations demonstrates the possibility of developing a super sensitive sensor for low permittivity fluid. However, a large sensitive range is needed, since water is the most common fluid and has a relatively high permittivity. Therefore, a $1\,$mm slot length is chosen for fabrication and measured for superior bandstop ability.

Figure 4.13a shows the comparison between simulated and measured insertion loss (IL) of the band-stop filter for the various fluids. When the channel is filled with air, the resonant frequency of the filter is $2.4\,$GHz which is in good agreement with the simulation results. The pass-band is above -2 dB both below and above the resonant frequency. As higher permittivity fluids are introduced, the resonant frequency of the filter decreases all the way to 1.74 GHz with the introduction of water from 2.4 GHz for the empty channel, which is

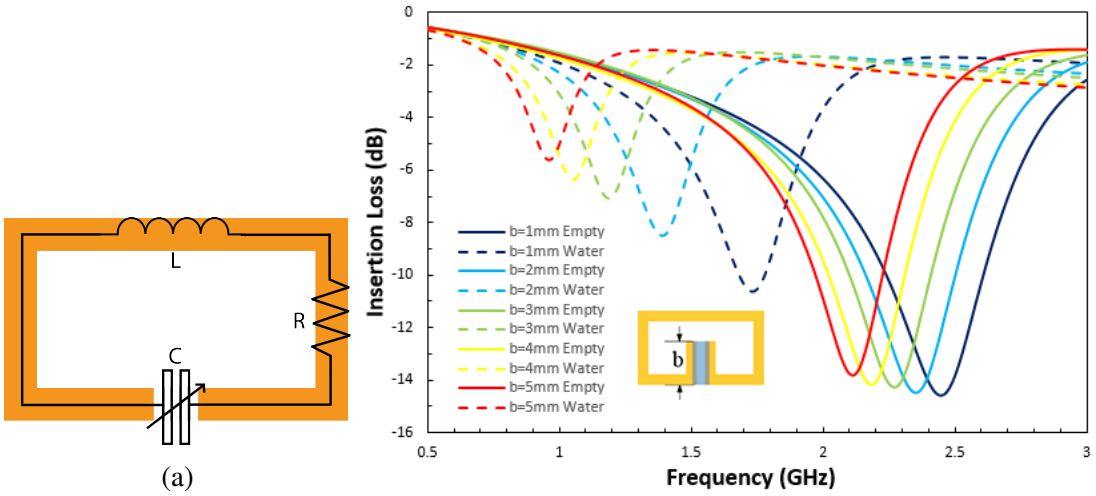

(a) (b)

Figure 4.12: (a) the equivalent circuit of microfluidics-based tunable SRR. (b) Sensitivity change with different slot in simulation.

a $28\,\%$ change in resonant frequency, or approximately $0.4\,\%/\varepsilon_r$. The $3\,$dB bandwidth of the filter ranging from empty, to filled with hexanol, glycerol and water are $8.3\,\%$, $8.5\,\%$, $13\,\%$, and $12.6\,\%$, respectively.

Typical devices have a temperature range in which they optimally perform. In the case of disposable microfluidic RF devices, it is vital to quantify stability versus variation in temperature. This is even more important in fluid-tunable or sensing systems as there will not only be temperature variation of the system itself, but typical fluids experience a drastic change in permittivity over temperature [15]. As a calibration, the system is initially filled with air, and the temperature of the test chamber is raised from room temperature, or $297\,$K, to $332\,$K (23 to $60\,^{\circ}$C). The S-parameters of the filter are recorded along with the steady state temperature within the chamber. The results of the calibration test, displayed in Figure 4.14, show that the resonant frequency of the system experiences less than $1\,\%$ variance over a temperature range of $297\,$K to $332\,$K. Upon returning to room temperature, the resonant frequency returns to its initial value as well. Therefore, this variance can be calibrated out of the final measurement result in practical systems. To measure the temperature's influence on the bandstop filter, the microfluidic channel is filled with water,

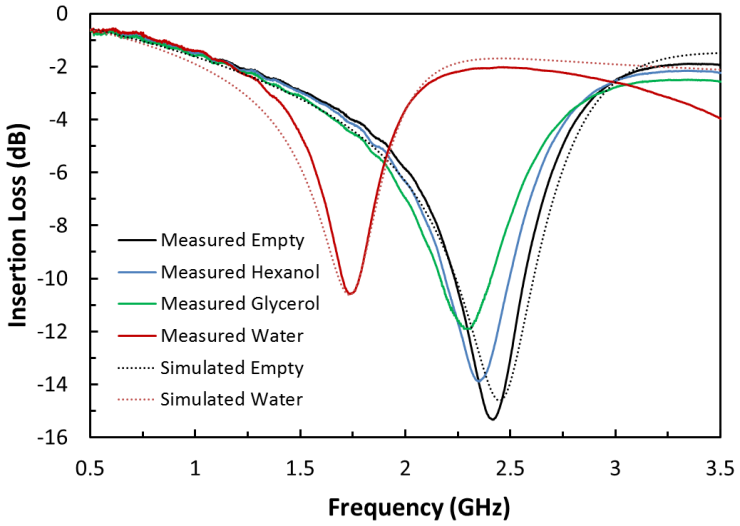

(a)

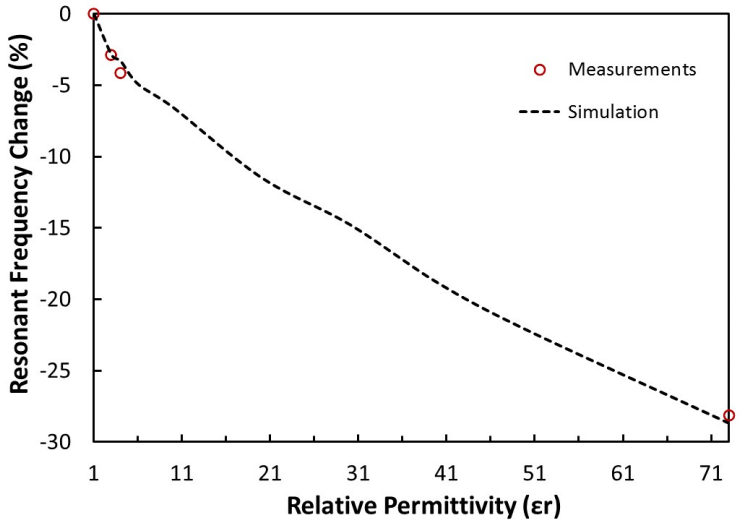

(b)

Figure 4.13: (a) Measured and simulated insertion loss (IL) of the SRR for different fluids pumped into the channel. (b) Resonance frequency shift (in percentage) of the SRR due to different fluids in the channel.

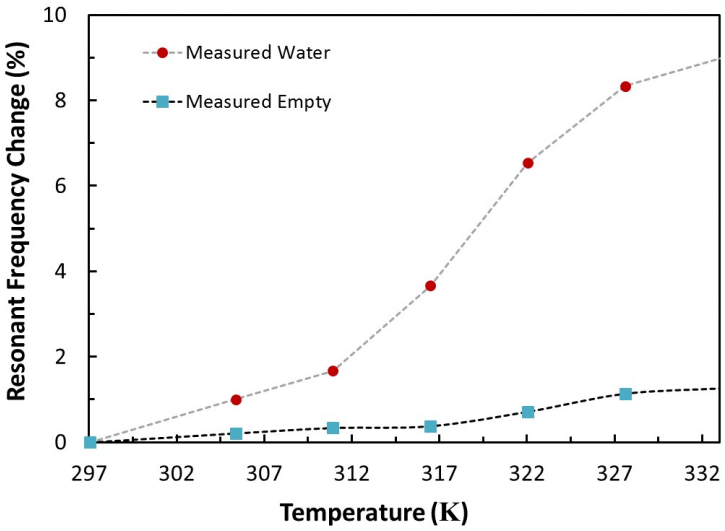

Figure 4.14: Measured resonance frequency shift (in percentage) due to temperature change with empty and water-filled channels for the SRR sensor.

and the temperature is then raised from 297 K, to 332 K, allowing the device to reach steady state before moving to the next temperature. Water is known to have a significant change in permittivity over temperature. Catenaccio reports a decrease of 21% in permittivity from 297 K, to 332 K [15]. It can be seen in Figure 4.14 that the resonant frequency shift when the resonator is loaded with water increases approximately $9\,\%$ over the temperature range due to the decrease in permittivity of the water. Using the results from the sensitivity measurement in Figure 4.13b, which yields a change of $0.4\,\%/\varepsilon_r$, along with the reported $21\,\%$ change in permittivity of water over the measured temperature range, an $8.4\,\%$ change is expected which matches very closely with the measured $9\,\%$ change. These extremely promising results show that the device can not only be used as a tunable filter, but also a temperature sensor. Again, the resonant frequency returns to its original value when the device returns to room temperature.

4.5 Dual-spiral Slot Resonator

Slot structures are very appropriate for microfluidics-based sensing as the permittivity value changes in the slot will drastically change its capacitance, which results in a shift of its res-

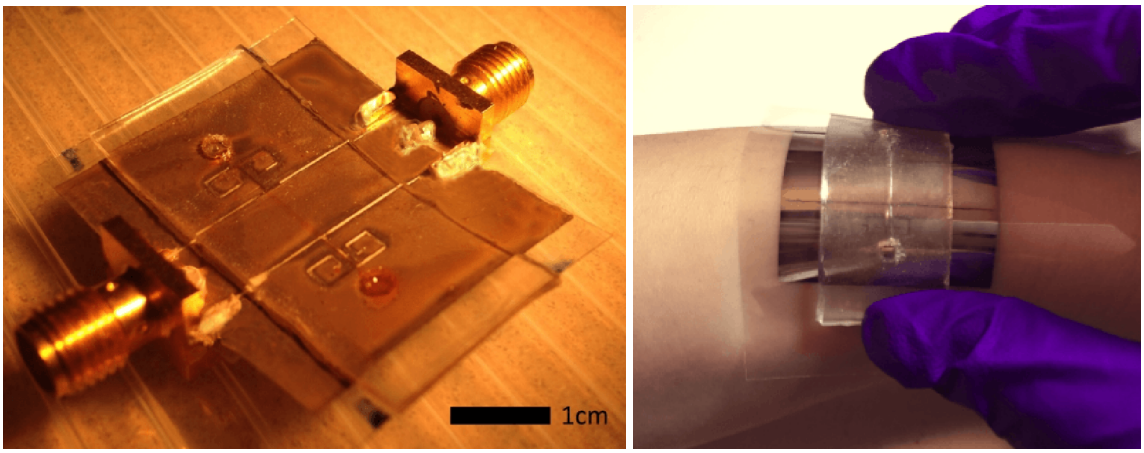

(a) (b)

Figure 4.15: (a) A photo of the fabricated microfluidic dual-spiral slot resonator sensor prototype. (b) A photo demonstrating the attachment of the sensor prototype on the wrist.

onant frequency and thus makes it an RF parameter. A dual-spiral-shaped slot resonator topology, as shown in Figure 4.15a, features a relatively high Q-factor while being a simple structure. The device is very flexible and can be worn on the wrist as shown in Figure 4.15b. The microfluidic channel is placed right on top of the longest slot to achieve a better sensitivity due to the locally stronger E-field. Two dual-spiral slot resonators are embedded in the two ground planes of a coplanar waveguide (CPW) so that the transmitted energy over this line would be trapped in the resonator at frequencies near the resonating frequency leading to an easy-to-detect bandstop characteristic.

The dual-spiral slot resonator structure can be modeled using lumped elements, as shown in Figure4.16b. Based on the transmission line theory and the spectral domain approach [111], the circuit can be simplified to the parallel RLC circuit [112] and the parameters can be extracted using the following equations:

$$R = 2Z_0 \left(\frac{1}{S_{21} \mid_{f=f_0}} - 1 \right) \tag{4.1}$$

$$C = \frac{\sqrt{a^2(R+2Z_0)^2 - 4Z_0^2}}{4\pi Z_0 R \Delta f \sqrt{1-a^2}} \tag{4.2}$$

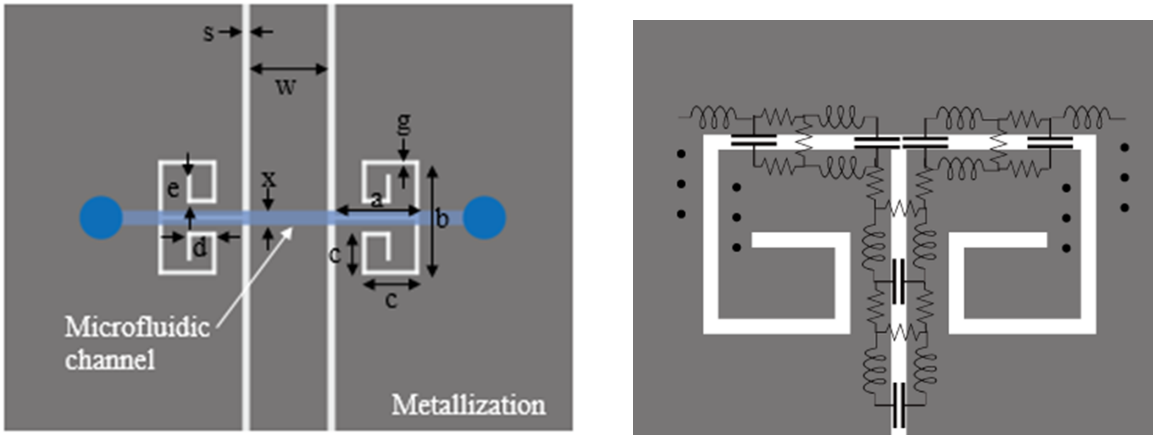

(a) (b)

Figure 4.16: (a) A drawing of the microfluidics-based tunable dual-spiral slot bandstop filter. (d) The equivalent circuit of a dual-spiral slot resonator.

$$L = \frac{1}{4(\pi f_0)^2 C} \tag{4.3}$$

where f_0 is the resonant frequency, Z_0 is the 50 Ω characteristic impedance of the coplanar waveguide, $S_{21}\mid_{f=f_0}$ is the numerical value of the insertion loss at the resonant frequency, a is the numerical value of the insertion loss at -6 dB cutoff frequencies, and Δf is the bandwidth between two -6 dB cutoff frequencies. Based on the measurements, the values of the equivalent lumped elements for both empty channel, and water-filled channel configurations were extracted through the use of the equations above and are shown in Table 4.2.

Table 4.1: Dimensions of the proof of concept SSR sensor in Figure 4.16a

Name	Dimension (mm)	Name	Dimension (mm)	Name	Dimension (mm)
a	4	b	6	c	2.4
d	1.6	e	1.2	g	0.1
w	6.4	s	0.3	x	0.55

To characterize the performance of the proposed sensor, a droplet of each different fluids under test was dripped to one of the two openings of the microfluidic channel. Due to the small size of the channel, the capillary action happens: when a dry channel opening

Table 4.2: Extracted parameters for equivalent parallel RLC circuit model for SSR sensor in Figure 4.16a

State of microfluidic channel	Empty Channel	Water-filled channel
Resistance R (Ω)	767.34	275.22
Capacitance C (pF)	0.80	1.68
Inductance L (nH)	2.10	3.13

is brought into contact with a liquid, it will imbibe the liquid at a rate which decreases with time. As the channel has the same size all the way between the two openings and the device prototype is placed horizontally to make sure that gravity's effect is negligible, the liquid would flow into the channel and fill the channel automatically. In this way, no microfluidic connector, pump or tube is needed but only a droplet of the fluid, thus simplifying the system while saving the bulk of the fluids under test. Due to the hydrophobic property of SU-8 and PDMS, the electrical and microfluidic parts were treated separately for 5 min in a UVO cleaner before filling water into the channel. Between consecutive tests with the same or different liquids, the two parts were demounted, cleaned by dry and cool air flow and mounted together again. A Rhode and Schwartz ZVA-8 VNA was used to measure the S-parameters of the device prototype under various fluids and bending conditions.

The sensitivity of the proposed device prototype is tested by several different fluids or fluid mixtures: water, ethanol, glycerol, hexanol, and water-glycerol mixtures with three different mixing ratios. The simulated and measured values of the insertion loss of the proposed resonator for different fluids in the channel can be found in Figure 4.17. A very significant frequency shift when replacing hexanol (ϵ_r = 3) with glycerol (ϵ_r = 4) can be observed, though the relative permittivity difference is barely 1 and the cross-section of the proposed sensing channel is as small as $5.4 \times 10^{-6} \times \lambda_0^2$. The variance of the stopband attenuation and the bandwidth for different fluids filled channel is due to the dielectric loss of various fluids and the mismatches as the frequency shifted largely. In Figure 4.18, a good logarithmic linearity can be observed in both simulations and measurements at around $-24\%/log(\epsilon_r)$. Due to the tiny size of the channel, only 0.6358 μL fluid is needed to fill the

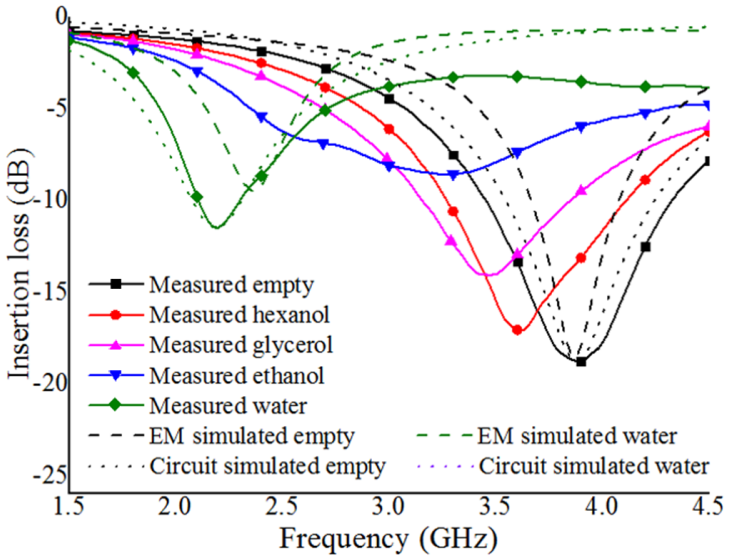

(a)

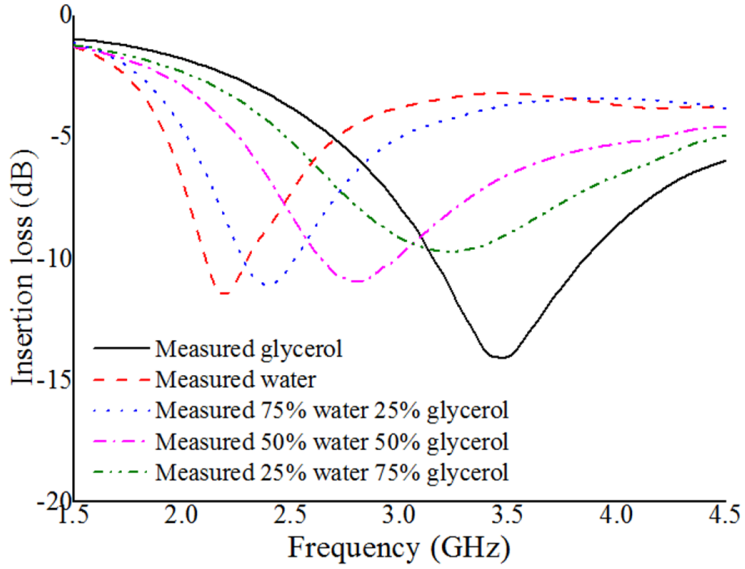

(b)

Figure 4.17: Measured and simulated resonant frequency change for fluids with different relative permittivity values: (a) four different pure liquid and air. (b) water-glycerol mixture with different mixing ratio.

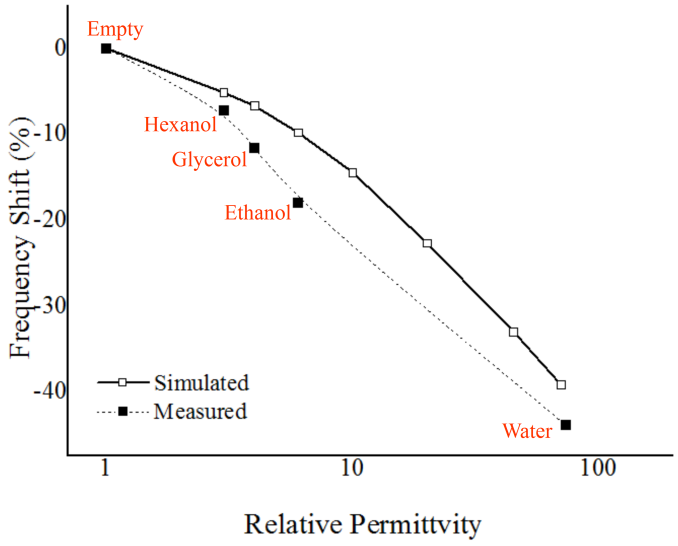

Figure 4.18: Measured and simulated values of the resonant frequency shift for different relative permittivity fluids in the channel of the slot resonator, demonstrating a logarithmic linearity of the sensor prototype.

channel, which results in a sensitivity around $37\%/log(\epsilon_r)/uL$. Any 0.4 log(ϵ_r) change will lead to a frequency shift larger than one 3dB bandwidth (10% for low-loss fluids), while the sensor resolution heavily relies on the system's resolution. The higher resolution of the analog to digital converter, the smaller frequency sweep step, and the lower noise source, the better the sensor resolution. The resonant frequency of the bandstop filter shifts by 43.8% in Figure 4.17a, from 3.9 GHz to 2.19 GHz when an empty channel is replaced with a water-filled channel. The sensor prototype was held above the ground to minimize the ground interference effects and to ensure the same measurement configuration for different liquids under test as shown in Figure 4.19a.

In addition to a good sensitivity, endurance and stable performance for different bending conditions are essential. To test the performance under bending status, the sensor prototype is measured flat (Figure 4.19a) and bent around four low-dielectric ($\epsilon_r < 2$) cylinders with four different radii: 7 mm, 10 mm (Figure 4.19b), 27 mm, 35 mm. An example of an experimental setup for a bent configuration with a 10mm radius is shown in Figure 4.19b while the flat configuration is shown in Figure 4.19a. The comparison between the in-

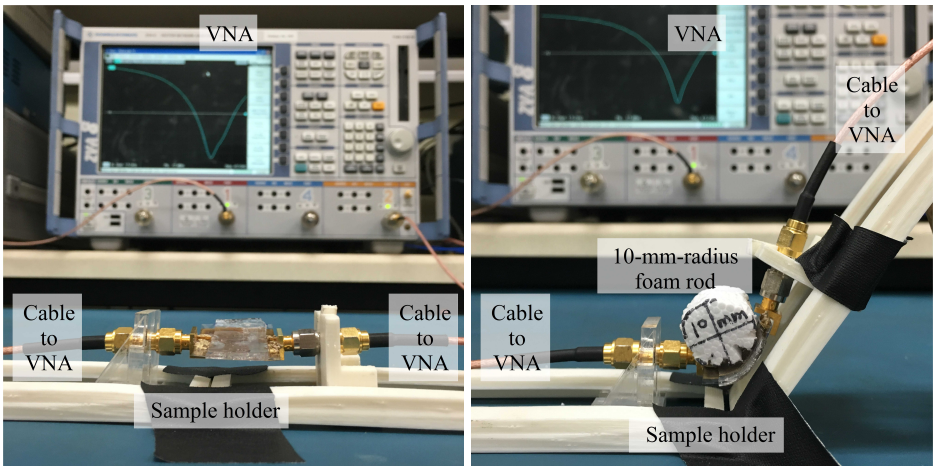

(a) (b)

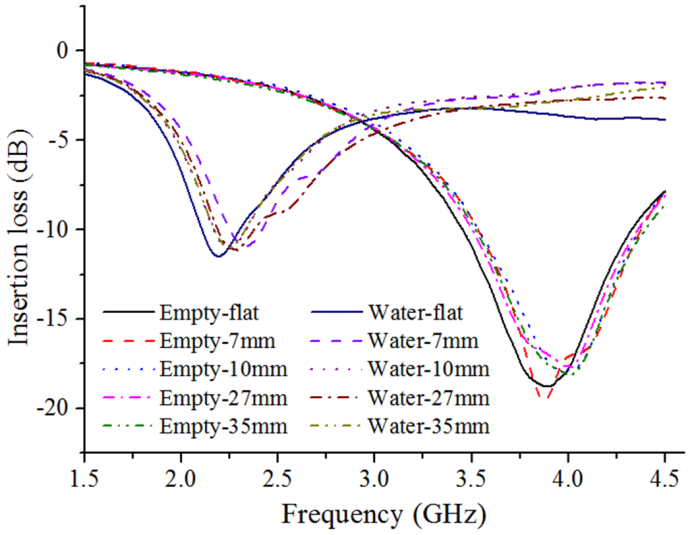

(c)

Figure 4.19: Photos of mesurement setup for flat sensor (a) and bent sensor (b) along with the measurement result in (c).

sertion loss values for the configurations of an empty channel ($\epsilon_r = 1$) and a water-filled channel ($\epsilon_r = 73$) for the four different cylinders and the flat configuration is shown in Figure 4.19c. Less than 130 MHz resonant frequency shifts and a smaller than 1.1 dB insertion loss variation are observed verifying a reliable performance for both bent and flat mounting conditions. After bending for 30 times, the insertion loss of the sensor prototype in the flat configuration was measured again and was very close to the initial measurements demonstrating good reusability and reliability between pre-/post-bending performance.

4.6 Dual T-resonator

Two T-resonators in parallel, as shown in Figure 4.20a, are integrated with fluid-tunable varactors. These two T-resonators, with their different physical sizes, resonate at different frequencies: the larger one (sensor 2) is 1.5 times larger than the smaller sensor (sensor 1), as shown in Figure 4.20b, so that the resonance of the sensors without any fluid is around 6 GHz (sensor 1) and 4 GHz (sensor 2), respectively. The microfluidics varactors operate based on a capacitor and a microfluidic cavity is placed over the capacitive gap to shift the effective permittivity between the plates and thus the capacitance. To obtain similar sensitivity, sensor 1 and sensor 2 have a ratio of 3:2 for the gap width in the varactors and the cavity size, as presented in Table 4.3. As the two T-resonators are in parallel, and resonant at different frequencies, the frequency shift of each sensor can be read independently.

Table 4.3: Dimensions of microfluidic cavities and channels for dual T-resonator in Figure 4.20b

Name	Dimensions (mm)		
	Length	Width	Height
Cavity in sensor 1	3	1.6	0.5
Cavity in sensor 2	4.5	1.4	0.5
Channels(each)	0.5	1	0.75

In Figure 4.20c, from an empty to a water-filled cavity, resonant frequencies shift 42.8% and 39.4% for two sensors respectively, which provides a sensitivity over $21\%/log(r)$ for

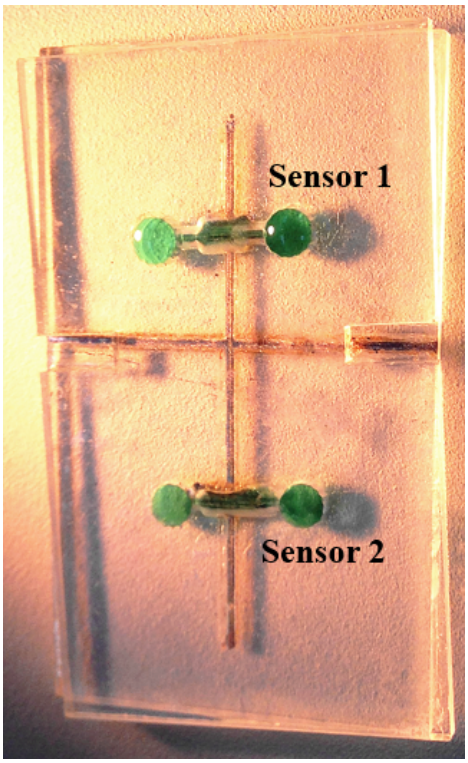

(a)

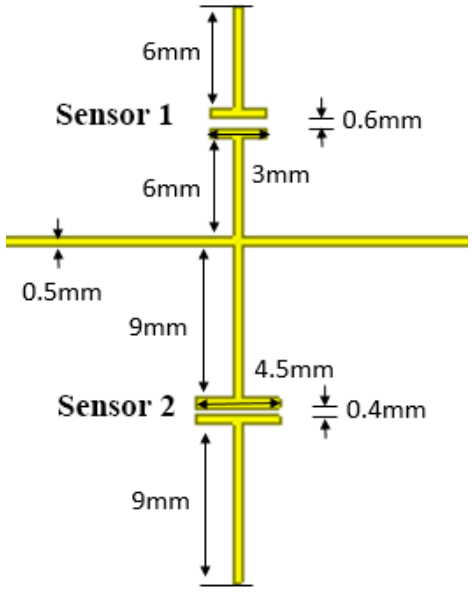

(b)

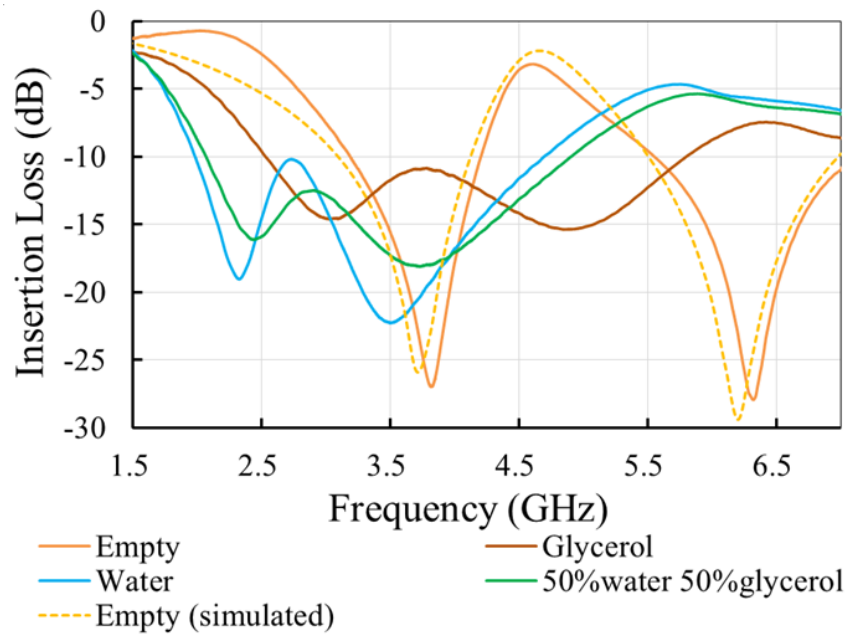

(c)

Figure 4.20: A photo (a) and a drawing (b) of the microfluidics-based tunable dual T-resonator bandstop filter along with measured and simulated the return loss in (c) with various fluid in channel.

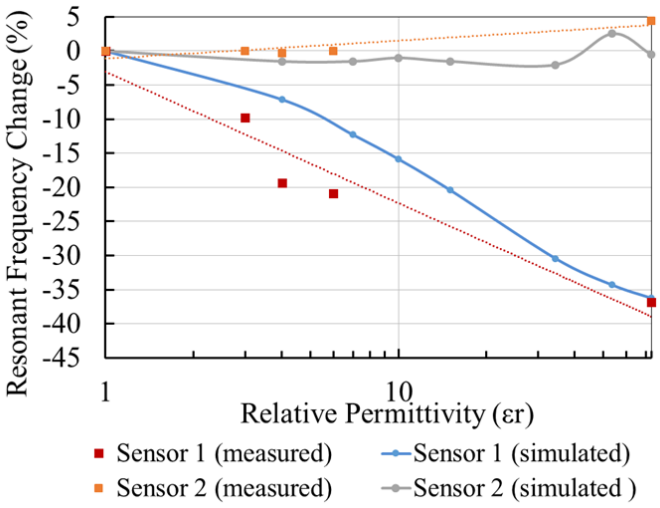

(a)

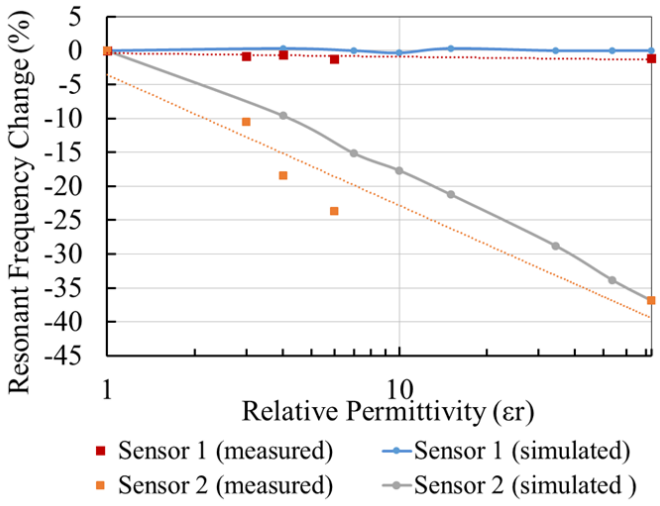

(b)

Figure 4.21: Measured and simulated resonant frequency change for fluids with different relative permittivity values in only one of the two sensors. (a) Fluids are in sensor 1 while sensor 2 stays empty. (b) Fluids are in sensor 2 while sensor 1 stays empty.

both sensors. The independence of the two sensors is demonstrated by filling one channel with fluids while keeping the other one empty. In Figure 4.21, the resonant frequency of the empty-cavity sensor stays almost constant while the sensor filled with different fluids has a frequency shift similar to Figure 4.20c, where both sensors are filled with fluids. In Figure 4.21a, sensor 2's small positive shift when the relative permittivity in sensor 1 is more than 40 is due to the influence of sensor 1's shifted resonance as the two sensors have very close resonant frequencies in this situation. Considering the situation of calibrating two similar fluids, the relative permittivity difference of two fluids is much less than 40 in most cases; overall this calibration system has a high independence between two sensors. Besides, good logarithmic linearity with a similar slope can be found for two sensors. Based on the resonant frequency shift in one sensor, the shift in another sensor for same fluid can be calculated, indicating that the two independent sensors can work together as a calibration and measurement set.

4.7 Microstrip Line and Step Impedance Low Pass Filter

The microstrip line is one of the most widely used transmission line structures in microwave systems, which constitutes a signal line, a dielectric substrate, and a ground plane. By embedding microfluidic channels into the substrate as shown in Figure 4.22b, a liquid-reconfigurable microstrip line can be easily designed. These microstrip lines can be modeled with the equivalent circuit in Figure 4.22a, in which the capacitance value is changing as a function of the permittivity values of the liquids filling the channel. As the characteristic impedance of the line depends on the capacitance of the tunable capacitor, its value varies with the permittivity of the fluids inside the microchannel.

As a proof-of-concept, two inkjet-printed microstrip line prototypes of this topology were fabricated with the dimensions listed in Table 4.4. Figure 4.22c shows the photo of the fabricated microstrip line 2 that features only minor dimension differences in the height of the embedded microfluidic channel and the width of the signal line, comparing to line

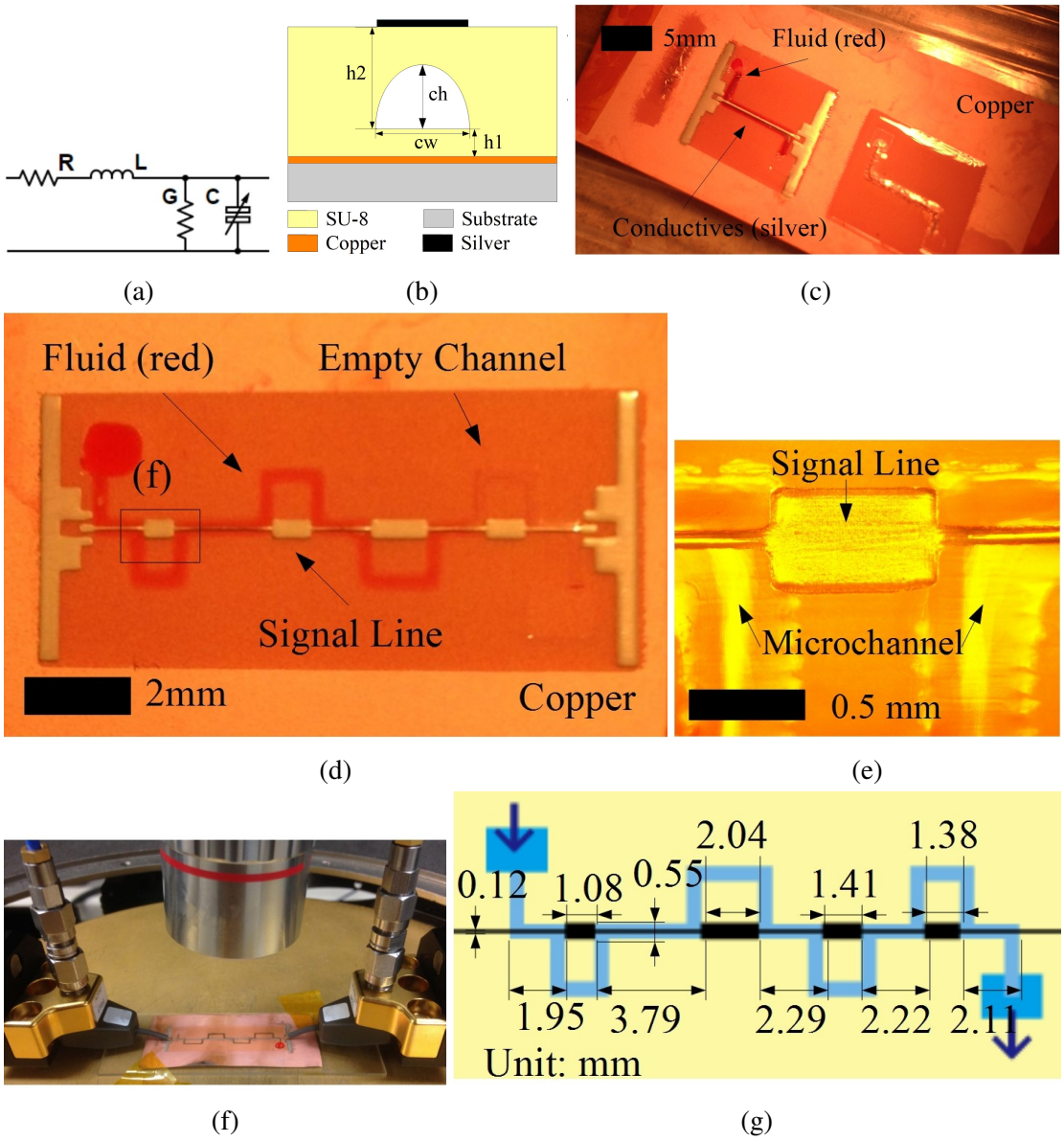

Figure 4.22: Fully inkjet-printed microfluidics sensors.
(a) The equivalent circuit of the proof of concept fully inkjet-printed liquid-reconfigurable microstrip line. The variable capacitance stems from the varying permittivity of the liquid inside the microfluidic channel. (b) A sketch of the cross-section view of the liquid-reconfigurable microstrip line. (c) A photo of the proposed fully inkjet-printed liquid-reconfigurable microstrip line prototype. (d) A photo of the fully inkjet-printed low-pass filter-based microfluidics sensor prototype. (e) Enlarged under-telescope view of the zone within the rectangle in (d). (f) A photo of measuring the sensor with a probe station. A red-dyed water drop was deposited to the inlet of the channel to fill the channel through the capillary effect. Two ground-signal-ground (GSG) probes were in contact with the sensor prototype and were connected to a VNA via SubMiniature version A (SMA) cables. (g) A schematic of the topology of the low-pass filter-based microfluidics sensor along with dimensions.

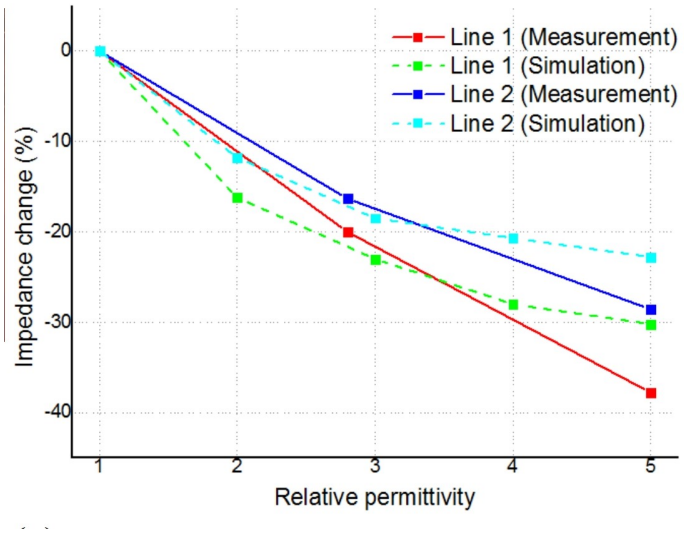

(a)

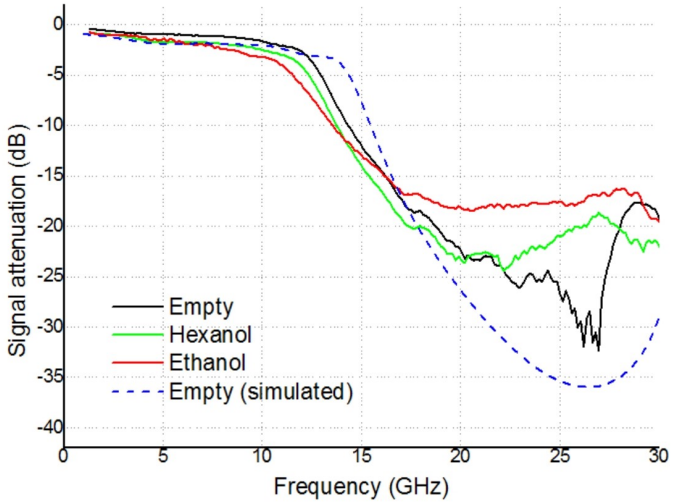

(b)

Figure 4.23: Measured and simulated results of the sensors in Figure 4.22. (a) Impedance vs. "liquid" permittivity relationship (simulated and measured) for the two fully inkjet-printed liquid-reconfigurable microstrip line prototypes in Table. 4.4, effectively defining the sensor sensitivity. (b) Measured signal attenuation when different fluids are fed to the channel as well as for an empty channel along with the simulated attenuation for an empty channel.

1. Microstrip line 1 was initially designed (empty channel) for a 50 Ohm characteristic impedance, which is the most common/reference impedance value in microwave designs. For the different filling liquids with a range of relative permittivities, the impedance can be tuned to as low as 31 Ohm (38% shift) as shown in Figure 4.22d. Similarly, microstrip line 2, which has an 87 Ohm default impedance, can be tuned down to as low as 67 Ohm (23% shift) with various liquids, as clearly shown in Figure 4.22d. Due to its larger channel height and wider signal line width, Microstrip line 1 is more sensitive to different fluids inside the channel compared with line 2. This liquid-reconfigurable microstrip topology could be potentially utilized in numerous applications including reconfigurable impedance matching in communication systems as well as wireless biosensing and water quality monitoring.

Table 4.4: Dimensions of the two embedded-microfluidics liquid-reconfigurable microstrip line prototypes in Figure 4.22b

Name	Channel height (*ch*)	Channel width (*cw*)	Substrate height		Signal line width
			bottom (h1)	top (h2)	
line 1	50 μm	600 μm	11 μm	66 μm	0.32 mm
line 2	30 μm	600 μm	11 μm	66 μm	0.12 mm

Based on the above introduced liquid-reconfigurable impedance-tunable microstrip line topology, a step impedance low pass filter was built alternating high- and low-impedance transmission line sections. Figure 4.22e and 4.22f shows photos of a fabricated prototype and Figure 4.22g lists the dimensions of the structure. This low pass filter would allow the propagation of low-frequency signals (under 13 GHz, passband), while attenuating signals at higher frequencies (stopband). The amount of attenuation strongly depends on the characteristic impedance of the transmission line sections, which varies for different fluids inside the channel. As a consequence, the fluid permittivity can be effectively sensed through the amount of the signal attenuation at higher frequencies while the signal attenuation at lower frequencies (passband) can be used as a calibration. The measured signal attenuation (or insertion loss, S21) (Figure 4.22g), matches the electromagnetic simulation results and demonstrates an excellent sensitivity as high as four dB/ϵ_r. The signal attenu-

ations values of the sensor when filling the channel with hexanol and ethanol featuring a relative permittivity difference of only 2.2 can be easily distinguished by a larger than 2dB difference, thus verifying the potential applicability of this inkjet-printed sensor topology to various fluid sensing applications, such as laboratory analysis, wireless liquid quality monitoring and distributed healthcare.

4.8 Summary

This chapter discusses several microfluidics-embedded microwave components for tunable RF electronics and liquid sensing application. The microwave structures introduced in this chapter are compared in Table 4.5. Three types of antennas (patch antenna[88], loop antenna[90], and slot waveguide antenna[113]) and three types of resonators (split ring resonator[89], slot resonator[114], and T resonator[91]) are studied as their resonant frequency can shift with dielectric permittivity of the liquid. Reconfigurable antennas are especially interesting as they can adapt to changing system requirements or environmental conditions, thus save space and expense for extra components. By embedding microfluidics channels to different antennas, a microfluidics-enabled reconfigurable antenna can be built, featuring low cost, high power handling capability, and high flexibility. A higher sensitivity is usually associated with a stronger E field and a larger volume of liquid. Therefore, resonators, especially the ones with slots, feature a very high sensitivity (e.g., 44% frequency shift from empty to water-filled channel) and are excellent candidates for wireless sensing. Besides resonant-based structures, a liquid-reconfigurable microstrip line along with a step impedance low pass filter based on the microstrip line is presented, showing the potential of embedding microfluidics in various structures to enable high reconfigurability[115].

Table 4.5: Comparison of microfluidics-based microwave structures demonstrated in Chapter 4

Structure	Design	Frequency	Shift (empty to water-filled)	Comment
Antennas	Coplanar patch	3.8 GHz	13%	
	Loop and balun	2.4 GHz	7%	Non-slot based tuning
	Slot waveguide	12.5 GHz	7%	wearable application
Resonators	Split ring	2.4 GHz	28%	Temperature sensor practice
	Dual-spiral slot	3.9 GHz	44%	Flexiblity tests
	Dual T	4.0/6.0 GHz	39/43%	Liquid calibration practice
Transmission	Microstrip line	wideband	-	Impedance reconfigurable
	Step impedance filter	13 GHz	-	Attenuation reconfigurable

CHAPTER 5

RFID PLATFORMS FOR MICROFLUIDIC SENSING

Radio-frequency identification (RFID) using backscattering electromagnetic signals can be used to realize wireless communication between the reader and the RFID tag for identification, tracking, and sensing applications, such as airport baggage tracking, access control, payments, and library book management. This chapter focuses on microfluidics sensing applications as RFID can enable real-time wireless sensing at a low cost which plays an essential role in distributed health care, food quality sensing, and ubiquitous environmental monitoring. Depending on its power source used to transmit electromagnetic waves, an RFID tag is classified either as an active tag (local battery), or a passive tag (interrogation with reader's radio waves). Due to the absence of the battery, passive tags have a much longer lifespan and are of special interest. Section 5.1 shows an interesting approach to combine wireless electrical sensing and comprehensive chemical sensing using passive RFID. Designs for RFID tags with IC components removed, known as chipless RFID tags, are then researched as they can further reduce the cost effectively. Both frequency modulated and phase modulated chipless RFID can be combined with microfluidic sensing as discussed in section 5.2.1 and section 5.2.2, respectively.

5.1 RFID-based Comprehensive Sensing Platform: Smart Test Strip

By combining RFID and paper-microfluidics technologies, a low-cost first-of-its-kind platform for comprehensive liquid sensing, the "smart test strip", is presented, which enables portable wireless real-time liquid sensing with handhold devices (e.g. cell phones), and integration of various multifunctional electrical and chemical sensors, for numerous Lab-On-Chip (LOC) applications including manufacturing control, environmental monitoring, and point-of-care medical diagnostic.

Test strips are widely used in chemical and biomedical assays in virtually every scenario from industrial manufacturing control to personal healthcare, as they are typically disposable, lightweight and easy to use. In order to enhance the functionality of test strips, in 2007, Whitesides and colleagues developed paper-microfluidics[63]. They patterned the channel and divided the paper into different functional areas, by printing hydrophobic walls on paper. Since then, paper-microfluidics and paper-based microfluidic analytical devices (uPAD) have been in the spotlight as they enable the integration of multiple chemical tests into a single strip[64, 65, 66] at a very low cost due to the additive manufacturing methods used[67, 68]. The more sensors the sensing platform includes, the more effective and comprehensive information about the tested liquid the tester can learn. It is natural to investigate whether it would be possible to integrate more sensors in a cost-effective way within these small test strips.

Recently, the number of electrical and electrochemical liquid sensors has grown significantly, as these sensors can easily turn the liquid information into electrical signals, which can be easily transmitted and recorded[116, 117]. Of special interest are the permittivity and conductivity values of the liquid under test, which effectively disclose contents' information. For example, fat content in milk[12] and fermentation of wines[13] can be easily monitored by the permittivity value, while the contamination of ground water can be detected by an abnormal conductivity value[14]. By embedding the microfluidic channel into the electrical circuits, various microfluidics sensors have been developed to enable real-time monitoring[20, 117, 114]. Combining passive Radio-frequency identification (RFID) technologies, the sensing information obtained from microfluidics sensors can be sent out wirelessly while eliminating the need for power / batteries [118, 119, 120]. Simply, a small RFID chip and an antenna can constitute a well-functioning passive RFID tag commonly used in tracking, locating and recently sensing applications. This light-weight low-cost and compact approach happen to be in the same route as μPAD, so it is natural to combine these two technologies to build a new generation of wireless comprehensive sensors - the smart

test strips.

This section presents the integration of paper-microfluidics chemical sensors and RFID-enabled wireless electrical sensors for comprehensive liquid sensing for the first time. On one side, regular paper-microfluidics chemical sensors usually use a specific chemical reagent in each sensor to detect a specific content, such as glucose or protein[64, 65, 66]. On the other side, electrical sensors sense liquid's information, such as conductivity or permittivity, which is a composite result of all liquid's contents[20, 121, 117, 114]. The smart test strip can obtain information from both (individual/composite), which allows for more degrees of monitoring, increases the information capacity, and significantly saves tester's time and effort. Compared with traditional sensors or sensing platforms, this new system can provide comprehensive information in a wireless and portable approach, which improves the efficiency drastically and enables next-generation liquid sensing.

5.1.1 System Overview

The smart test strips system consists of various smart strips and one reader as shown in Figure 5.1. Within every individual test strip, there are multiple chemical sensors, such as pH, glucose and protein, which are divided in different sections and deposited with different reagents that react with the testing content and produce colorful compounds. Based on the color intensity, the concentration of the chemical content under test can be detected. Various researchers in the chemical and biomedical area have reported numerous sensors of this type [63, 64, 65]. In addition to the chemical sensors, multiple electrical sensors, such as permittivity sensors, conductivity sensors, and temperature sensors, can be embedded within the test strips taking advantage of their inherent property to easily translate the liquid's information to a resistance or capacitance change. The RFID chip then digitizes the resistance or capacitance to a binary signal, which is afterwards transmitted back through the antenna to the reader/gateway employing backscattering techniques. The chemical sensors obtain information about specific and/or expected chemical substances

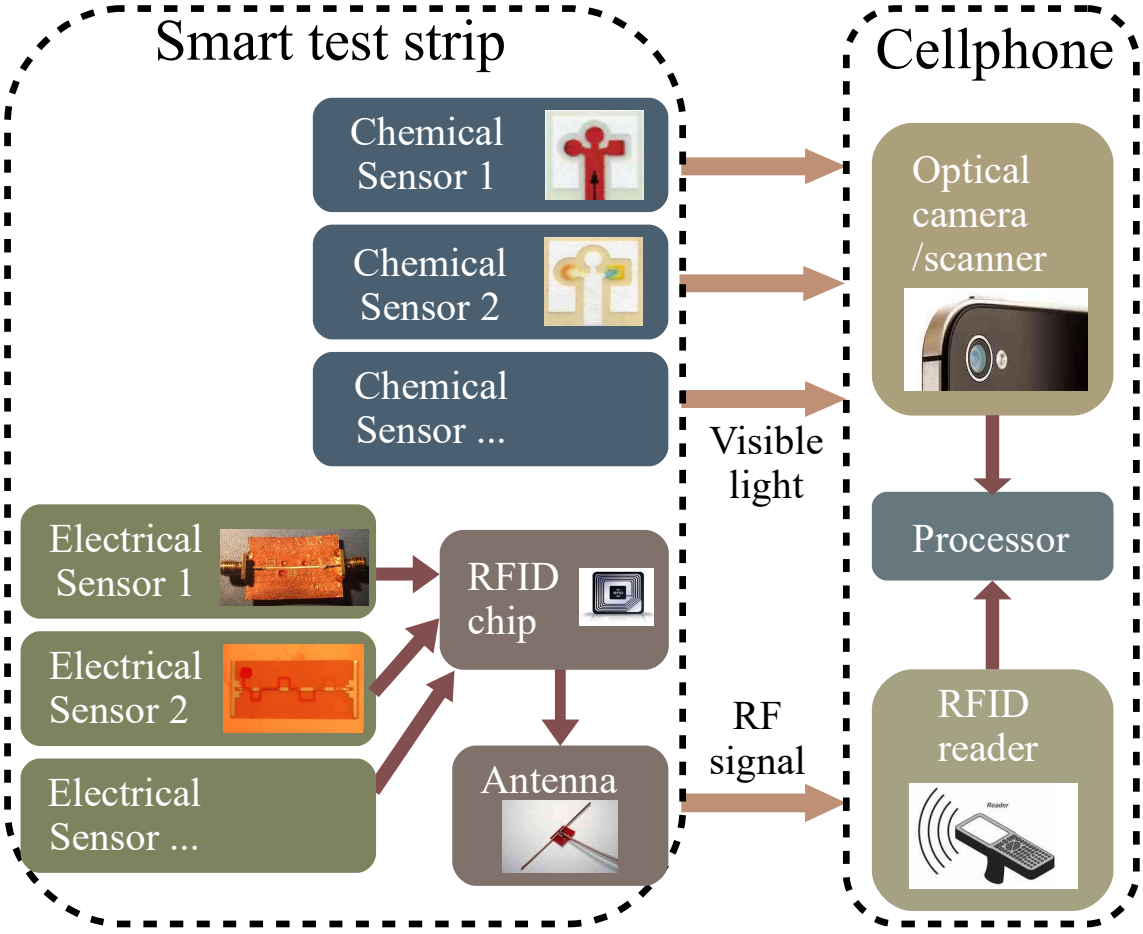

Figure 5.1: A block diagram of the smart test strips system-level operation principle.

within the liquid under test, while the electrical sensors provide the comprehensive overall status including the composite effect of all contents.

A proof-of-concept prototype of the smart test strip platform with two electrical sensors, three chemical sensors, and an antenna, is shown in Figure 5.2a and another realization of the same system topology including an electrical sensor, a chemical sensor and an antenna operating in lower frequencies is shown in Figure 5.2b. The smart test strip can also be realized on off-the-shelf chemical sensors such as the PH strip shown in Figure 5.3a, with the cross-section view of the microfluidic channels demonstrated in Figure 5.3b. When a drop of liquid reaches the opening of the stand-alone channel, the channel imbibes the liquid because of the capillary effect. Afterwards, the liquid goes through the electrical

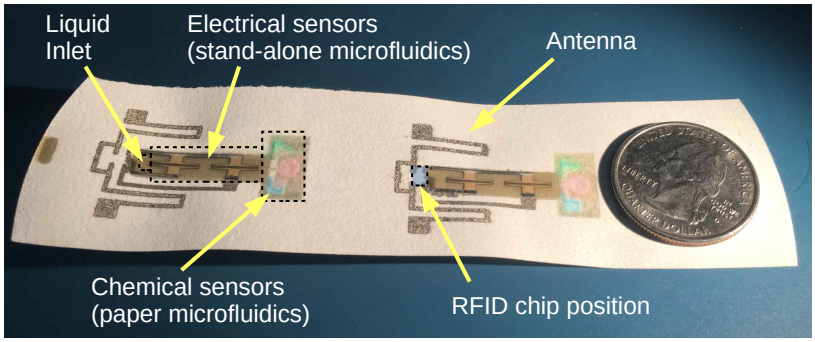

(a)

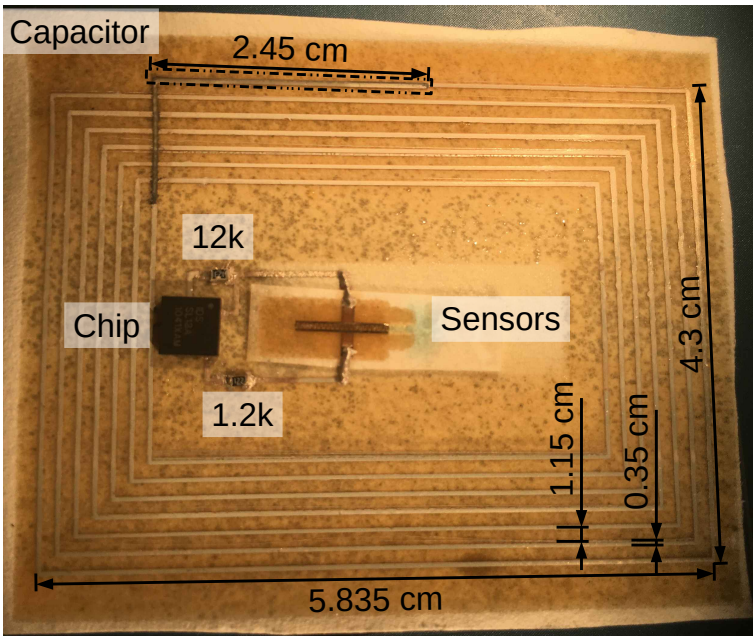

(b)

Figure 5.2: A photo of fabricated smart test strip prototypes working at (a) wireless and (b) near-field communication (NFC) frequencies.

sensors inside the stand-alone channel and then comes to the paper-microfluidics to interact with the chemical reagents.

On the reader side, portable devices, such as cell phones, can perform the reading easily: the phone cameras can be used to digitize the intensity of color of each chemical sensor[101]; the antenna on the phone can transmit and receive the RFID backscattering signal in the meantime. The phone can then send the signal to an off-site laboratory for analysis by a trained professional or immediately filter it through preset criteria in the phone and directly return the testing conclusions.

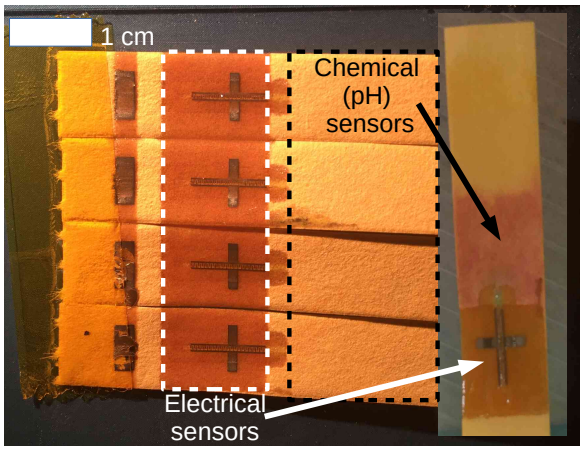

(a)

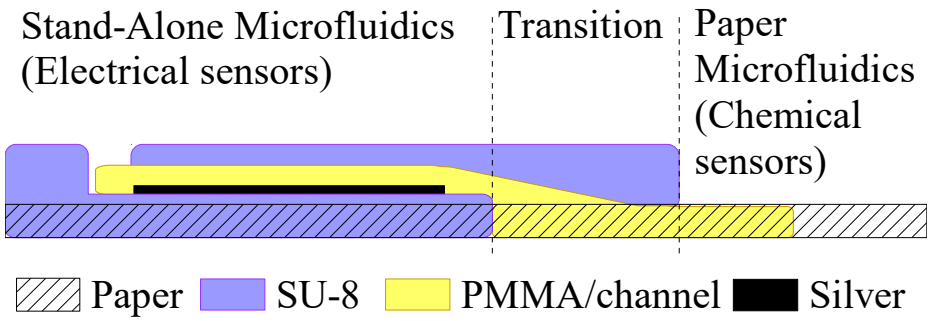

(b)

Figure 5.3: (a) A photo of multiple smart electrical sensors integrated on pH test strips along with an inserted photo (right) of one pH smart strip tested by vinegar confirming the unaffected good performance of the chemical sensor. (b) A drawing of the cross-section view of the smart test strip channel topology.

As inexpensiveness, scalability, and disposability are key requirements to ensure the ubiquitousness of the smart test strips, additive manufacturing techniques with adequate resolution would be among the best fabrication solutions. To the best of author's knowledge, inkjet-printing is the only AM tool that can facilitate the fabrication of all three parts of the smart test strip, (microfluidics, paper microfluidics, and RFID tags) easily and cost-effectively, so it is one of the best candidates for the fabrication of the smart test strips. Compared with fabricating these three parts separately and assembling afterwards, the fully inkjet-printing process can effectively eliminate the equipment cost, while saving time and space of assembly. Section 3.1.5 describe the fabrication techniques enabling the low-cost on-the-demand fabrication of the smart test strip sensing platform.

5.1.2 Sensor on Strip

Microfluidics-based electrical sensors have been developed for different applications, such as temperature sensing[117], heavy-metal ion monitoring[122], and glucose concentration detection[25]. Most of them take advantage of the permittivity or conductivity of different liquids by comparing either the current-voltage (I-V) curves or the frequency responses.

IDE structures

Figure 5.4a shows an electrical sensor on a smart test strip that can enable multiple sensing functions. Interdigitated electrodes (IDEs) were used in this prototype as they effectively increase the surface (sensing) area of the electrodes without increasing the total sensor area. The microfluidic channel is placed right on the top of the IDEs to maximize the sensitivity.

The equivalent circuit of the IDE structure is shown in Figure 5.4c; the measured impedance can be approximated by a parallel RC circuit. On the one hand, the total resistance (R_{total}) can be modelled as two resistors in parallel: a constant resistor (R_0) due to the filter paper and a varying resistor (R) due to the liquid inside the channel. Thus, the relation between the varying resistivity (ρ) and the measured/sensed resistance (R_{total}) can be seen in

$$R_{total} = \frac{1}{\frac{1}{R} + \frac{1}{R_0}} \approx R = \frac{d_{eff}}{A_{eff}} \times \rho. \tag{5.1}$$

where d_{eff} and A_{eff} are the effective distance and cross-section surface area between the two gap-separated interdigitated electrodes, while ρ is the resistivity value of the liquid in the channel. In most cases, R_0 is very large, so the approximation in (5.1) is valid and the measured resistance (R_{total}) is linearly proportional to the resistivity (ρ) of the liquid inside the channel. On the other hand, similarly, the total capacitance (C_{total}) can be calculated through the parallel combination of two capacitors: a constant capacitor (C_0) due to the filter paper and a varying capacitor (C) due to the liquid inside the channel. The relation

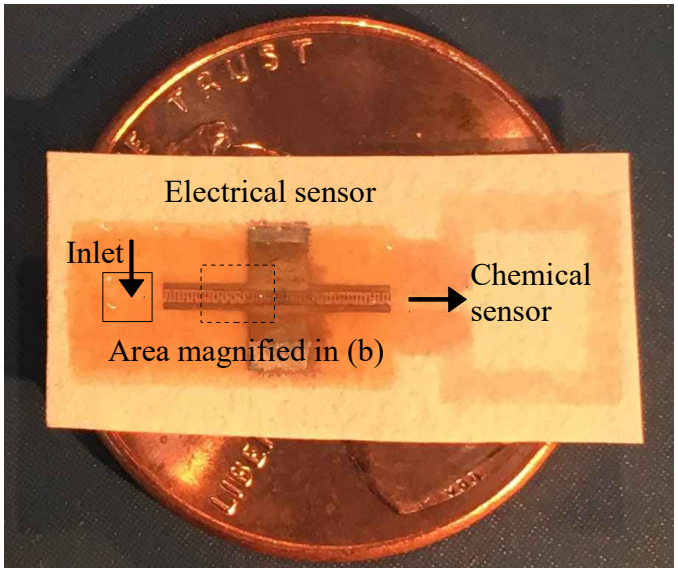

(a)

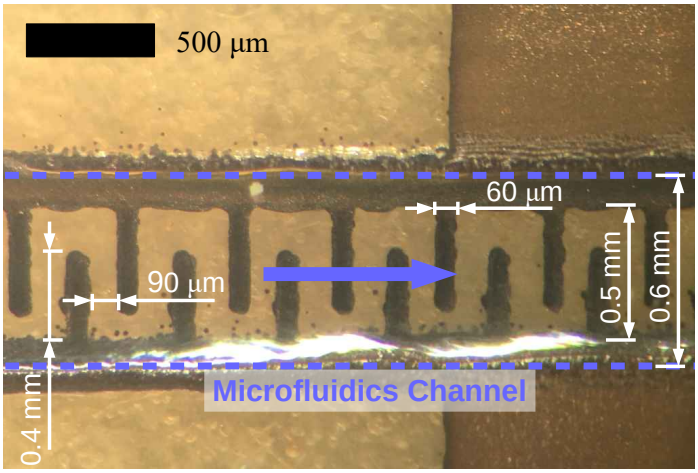

(b)

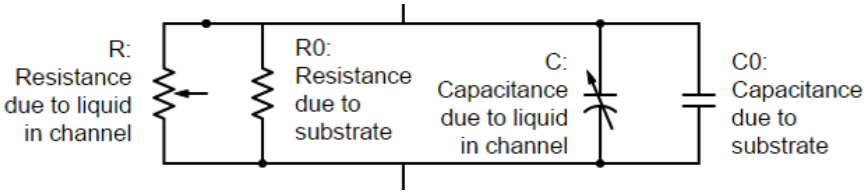

(c)

Figure 5.4: (a) A photo of a printed sensor prototype compared to an 1-cent coin. (b) Magnified view of the interdigitated electrode (IDE) structure in the dashed square in (a). (c) Equivalent circuit of the IDE sensors.

between the varying permittivity (ϵ_r) and the detected capacitance (C_{total}) can be calculated applying the parallel-plate capacitor model and is given by

$$C_{total} = C + C_0 \approx \frac{A_{eff} \times \epsilon_0}{d_{eff}} \times \epsilon_r + C_0. \tag{5.2}$$

ϵ_r is the relative permittivity of the tested liquid, while ϵ_0 is the free space permittivity. With the approximation in (5.2), the measured/sensed composite capacitance (C_{total}) is linearly proportional to the relative permittivity (ϵ_r) inside the channel.

To simplify the real-time measurements and avoid dealing with complex impedances, the IDE structure can be treated as either a resistor or a capacitor: in the case that the tested liquid has a relatively high conductivity or DC voltage is applied ($R_{total} << \frac{1}{\omega \times C_{total}}$, where ω is the measurement radial frequency), the imaginary part of the impedance can be neglected and the IDE structure can be seen as a simple resistor; otherwise, if the tested liquid is non-conducting and AC voltage is applied, the IDE structure can be approximated by a capacitor.

Resistivity-based Sensing

Resistivity-based sensors are widely used in electrochemical sensing, especially for ion detection. In water quality testing, resistivity values usually imply the salinity[123], which has a large impact on plant's growth and agriculture, as high-salinity water would dehydrate and kill the plants. Moreover, the conductivity of the water is strongly related to the ion concentration. For example, sea water's conductivity is one million times higher than that of deionized water, and the conductivity of various aqueous sodium chloride (NaCl) solutions with different concentrations are shown in Table 5.1. Therefore, resistivity-based sensors play an essential role in water quality test kits and are of significance in the smart test strips.

An IDE-based resistivity sensor was simulated by COMSOL Multiphysics modeling software and measured with an Agilent U1733C handhold LCR meter on the probe station

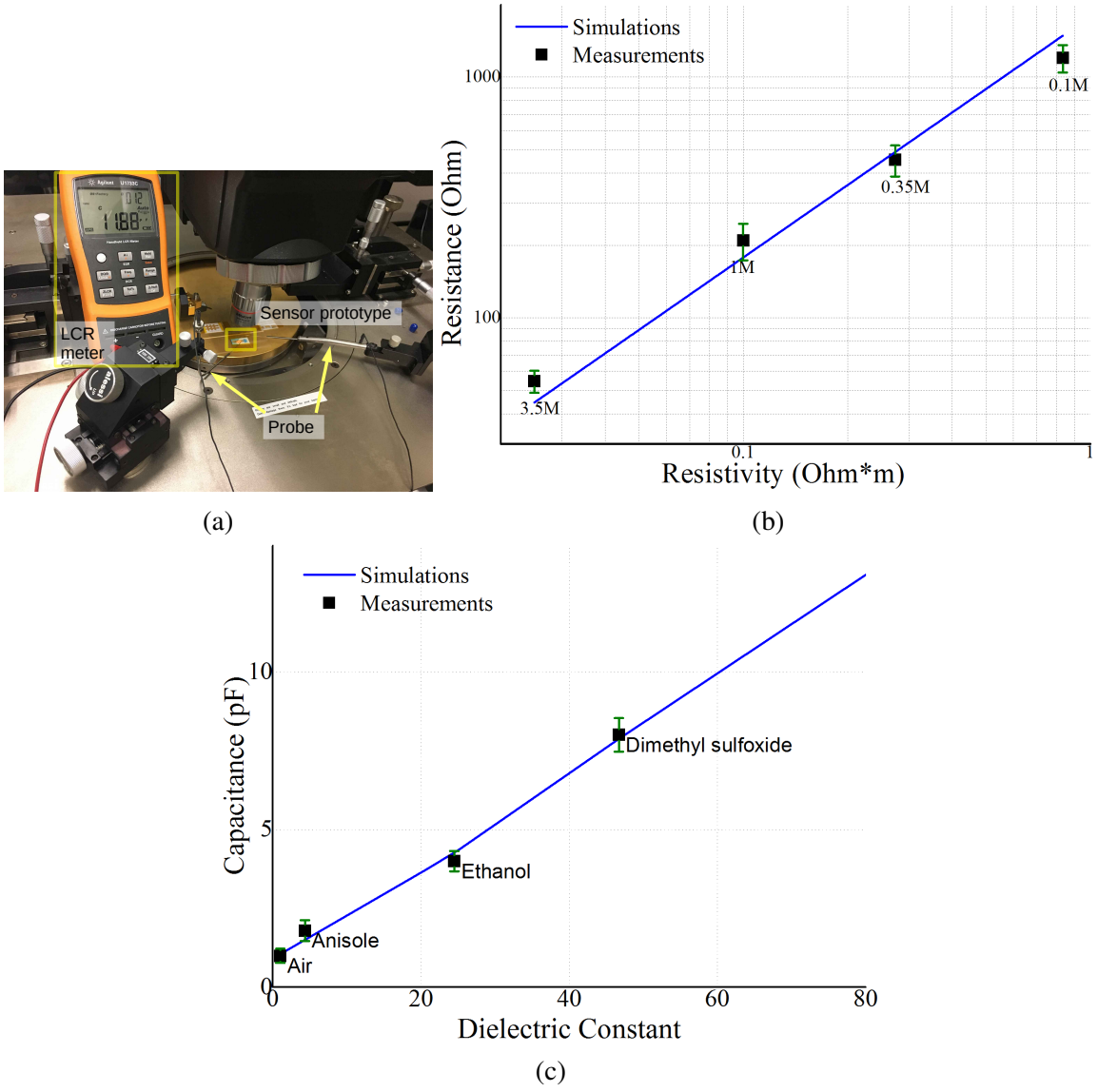

Figure 5.5: (a) Measurement setup for the microfluidic sensor testing. (b) Simulated and measured the average resistance of the sensor for filling liquids with different concentration (resistivity), along with the error bars showing the standard deviations of 20 replicas that were measured ten times each. (c) Simulated and measured average capacitance of the sensor for filling liquids with different dielectric constants, along with the error bars showing the standard deviations of 20 replicas that were measured ten times each.

Table 5.1: Conductivity of different sodium chloride (NaCl) aqueous Solutions for Various Concentrations[124]

Concentration (Mol/L)	Conductivity (S/m)
0	5.5e-6
0.10	1.2
0.35	3.7
1.0	10
3.5	40

with a parallel RLC setting as shown in Figure 5.5a. The LCR meter was connected to two probes, which were calibrated with open and short circuits before performing the measurement. The simulated resistance of the sensor (the simulated results were derived from the complex impedance of the equivalent circuit shown in Figure 5.4c) versus resistivity of the liquid inside the microfluidic channel is shown in Figure 5.5b, along with measurement results for various sensor-filling aqueous solutions of sodium chloride featuring a sensitivity of 1782 $\Omega/(\Omega \cdot \mathrm{m})$, which is superior compared to subtractively manufactured IDE sensors[125]. The concentration of the sodium chloride in the water can be easily determined from the measurements.

Permittivity-based Sensing

The values of permittivity (also called dielectric constant in some cases) of the liquids in the natural environment vary widely, as shown in Table 5.2. Mixtures of two or more fluids can feature a wide range of continuous permittivity as a function of the mixing ratios [126]. Similarly, the permittivity of the solution varies depending on its concentration[11]. Thus, if a device is capable of detecting small changes in the permittivity values of a liquid, it may deduce a significant amount of information about it.

Similar to the resistance-based sensing, the relationship between the measured capacitance and the liquid's permittivity was simulated by the COMSOL modeling software and measured with the LCR meter at 1 kHz with the results displayed in Figure 5.5c. The sensor prototype was characterized by 4 different materials (air and three organic fluids) filling

Table 5.2: Dielectric constant of air and three organic fluids at 1 kHz and room temperature[127]

Name	Dielectric constant (ϵ_r)
Air	1.00
Anisole	4.33
Ethanol	24.3
Dimethyl sulfoxide	46.7
Deionized water	80.0

the microfluidic channel with the respective dielectric constants shown in Table 5.2, featuring an excellent sensitivity of 15%/ϵ_r (or 0.15 pF/ϵ_r), which enables the sensing of very small liquid content changes and is superior compared to subtractively manufactured IDE sensors[125, 128]. For example, the permittivity of ethanol and water mixtures is varying by 5.5 for every 10% weight mixing ratio difference at room temperature, according to [9]. Therefore, if the prototyped sensor is used in alcohol/wine testing, the sensitivity would be 8.25%/wt.%, which means 1% of mixing ratio changes will lead to 8.25% capacitance variation, given that the measured sensitivity is 15%/ϵ_r.

5.1.3 Wireless Interrogation

RFID technologies could potentially revolutionize the efficient wireless interrogation of the smart strip sensors. As the smart test strips are designed to work with portable devices, such as cell phones, that read the RFID while scanning the color of a chemical sensor at the same time, a small reader range ($<$ 20 cm) would be required, which fits very well with the use of passive RFID's, that can be woken up / interrogated with very low power levels while eliminating the need for batteries. Recently, new RFID sensor chips enabling the Internet of Things (IoT) were invented at both academia[129, 130] and industry, while new RFID chips at HF and UHF band that have multiple external pads for resistivity reading have been on the market, such as Melexis MLX90129, TI RF430FRL, AMS SL13A, and SL900A. With the help of those chips, the capacitance and resistance sensing values can be

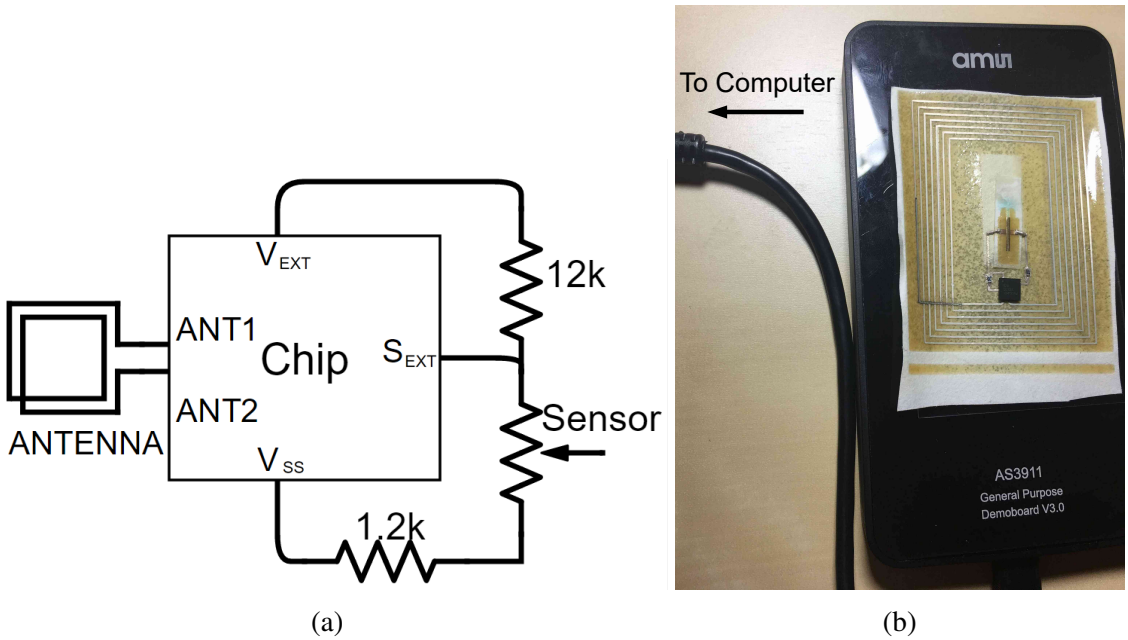

(a) (b)

Figure 5.6: (a) The schematic of the external circuit to the RFID chip. (b) A photo of the measurement setup of a smart test strip with an NFC RFID reader.

easily converted to binary code and sent to the reader through the use of antennas. Typical smart test strip configurations allow for the easy and direct integration of the antennas on the filter paper, which largely simplifies the process and decreases the resulting cost.

Wireless System Realization and Testing

For proof-of-concept purposes, a smart test strip was designed with a coil antenna working at 13.56 MHz, an AMS SL13A RFID chip, two resistors and a resistivity sensor, as shown in the Figure 5.2b. 13.56 MHz wireless configurations were chosen due to the widely-available off-the-shelf RFID / Near Field Communication (NFC) chips and due to many existing phones being equipped with the NFC capability for applications such as mobile payments. The schematic of the external circuit connected to the chip is shown in Figure 5.6a. A coil antenna with a capacitive structure at the end was designed with Ansoft HFSS to resonate at 13.56 MHz. The coil in Figure 5.2b features a size similar to credit cards, while in space-constrained scenaria, more miniaturized antennas operating in higher frequencies can be used. By harvesting RF power from the reader, the chip can supply 3.4-V output voltage (at V_{EXT}) to the sensor circuit. The ADC circuit in the

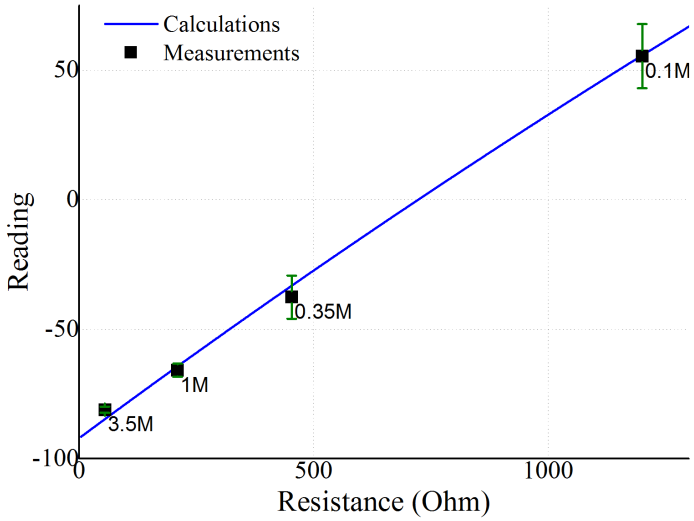

Figure 5.7: Calculated wireless reading of the smart test strip prototype in an NFC chip configuration along with measured values for sodium chloride aqueous solutions of different concentrations, along with the error bars showing the standard deviations of measuring the sample for 20 times.

chip (at S_{EXT}) can convert voltage values between 300 mV and 600 mV to 10-bits digits, therefore two resistors (12 kΩ and 1.2 kΩ, respectively) were used to divide the output power appropriately to the sensor. Figure 5.6b shows the measurement setup for the wireless interrogation of the test strip. The strip was read by an AMS AS3911 general purpose NFC reader in a 1-cm distance and the connected computer decoded the NFC signals into a unitless numeric sensing readout from -100 to 60 as shown in Figure 5.7. Firstly, various voltages were applied to S_{EXT} and respective readings were recorded to calculate the curve in Figure 5.7, which demonstrates the performance of the RFID tag platform. Then the IDE-based resistivity sensor was added and sodium chloride aqueous solutions with four different concentrations were filled to test the performance of the integrated system. For the above mentioned configuration, the sensor can sense the resistance change of the sensor from 0 to 1300 Ω, with an average minimal detectable resistance change (sensing resolution) of 1.33 Ω, demonstrating an excellent wireless sensing capability of the smart test strip.

Extension to Wireless Frequencies

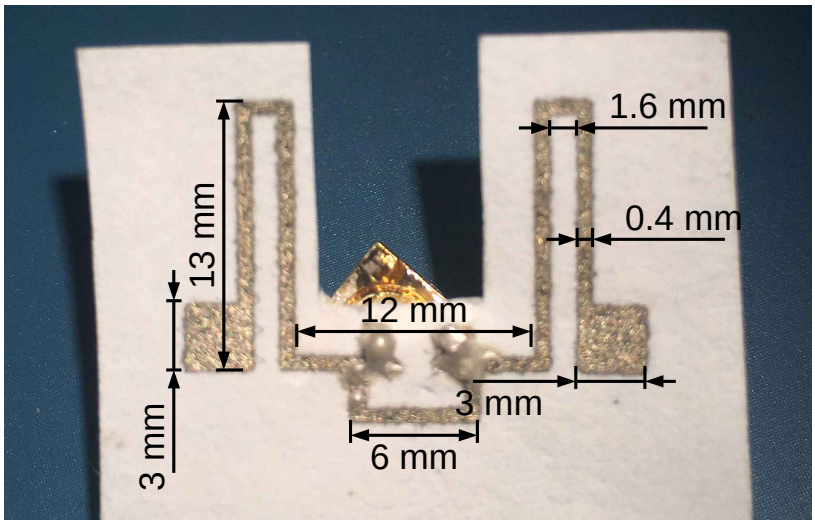

Figure 5.8: Inkjet-printed meander-line dipole antenna on filter paper for wireless smart test strips.

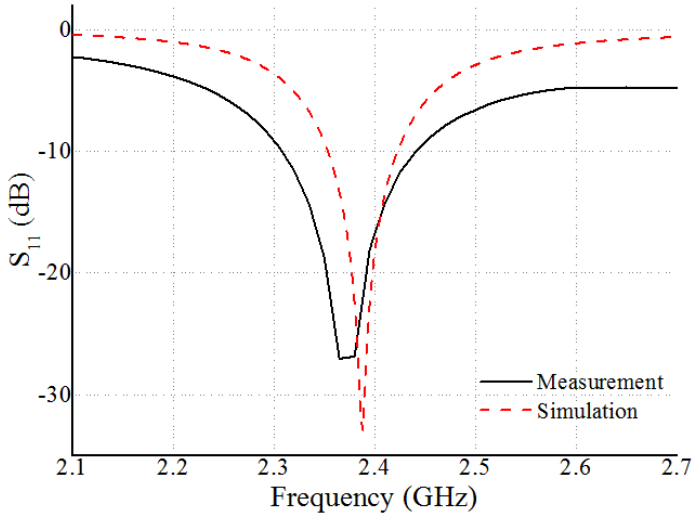

Figure 5.9: Simulated and measured return loss (S11) of the inkjet-printed dipole antenna on filter paper.

Wireless frequencies, e.g., 2.4 GHz, feature a great potential for the smart test strip, as they have excellent compatibility with existing cell phone antennas as well as better compactness compared to NFC frequencies. However, limited choices of off-the-shelf RFID sensor chips operating at 2.4 GHz were observed. Here, an inkjet-printed tag antenna on filter paper operating around 2.4 GHz is presented to demonstrate the potential of operating the smart test strips at wireless frequencies. A meander line dipole antenna, as shown in

Figure 5.8, was designed due to its inherent miniaturization properties thus enhancing flexibility and wearability. The antenna was simulated by a full-wave simulator (Ansoft HFSS) and was measured by a Rhode and Schwartz ZVA-8 Vector Network Analyzer (VNA) with results shown in Figure 5.9. A good impedance matching with a maximum gain of 1.3 dBi was observed, which is comparable to other inkjet-printed antennas on paper substrates[104] and verifies the feasibility of smart test strips operating at wireless frequencies.

5.2 Chipless RFID Configuration

As mention before, the cost of ICs dominates the cost per each RFID tag while most of the system cost is spent on the tags, thus making it a major concern in the design and adoption of a low-cost RFID system. In addition to manufacturing costs, regardless of active or passive tags, the ICs in the tags need a certain power to "wake up", which further complicates the design of RFID systems and imposes limitations on their uses. In addressing the above-mentioned problems, researchers have proposed various designs on RFID tags with the IC components removed — chipless RFID tags. Being cost-effective and straightforward in design, chipless RFID tags have drawn a significant amount of attention from researchers as evidenced in [131, 132, 133, 134].

5.2.1 Frequency Modulation: Encodable Chipless RFID

The microfluidics-based encodable chipless RFID tags operate as shown in Fig. 5.10. Compared to conventional chipless RFID's, an encoding/tunable multiresonator component is integrated and is the key component of the system. Multiresonators, such as multiple spiral resonators, are commonly embedded in chipless RFIDs due to their inherently simple geometry along with an excellent frequency-coding capability [131, 133]. The key of the real-time encoding mechanism is to shift the resonant frequency of the spiral resonator in a chipless RFID, and this can be done by changing on-the-fly the resonator's capacitance in the following way: By embedding a microfluidic channel in the spiral's gap between adja-

cent turns, the capacitance of the gap can be tuned by altering the status ("filled"/"unfilled") of the microfluidic channel, due to the large difference in the relative permittivity between air and water (1 and 80 respectively)[135]. Given that the resonant frequency shifts in response to status changes in the microfluidic channel, the data encoding mechanism was designed in the following way: the original resonant frequency (event "unfilled") represents code '0' and shifted (event "filled") represents code '1'. The chipless RFID is fully inkjet-printed with the process discussed in section 3.1.4 to enable low-cost fast on-demand manufacturing, and fabricated tag can be found in Figure 5.11

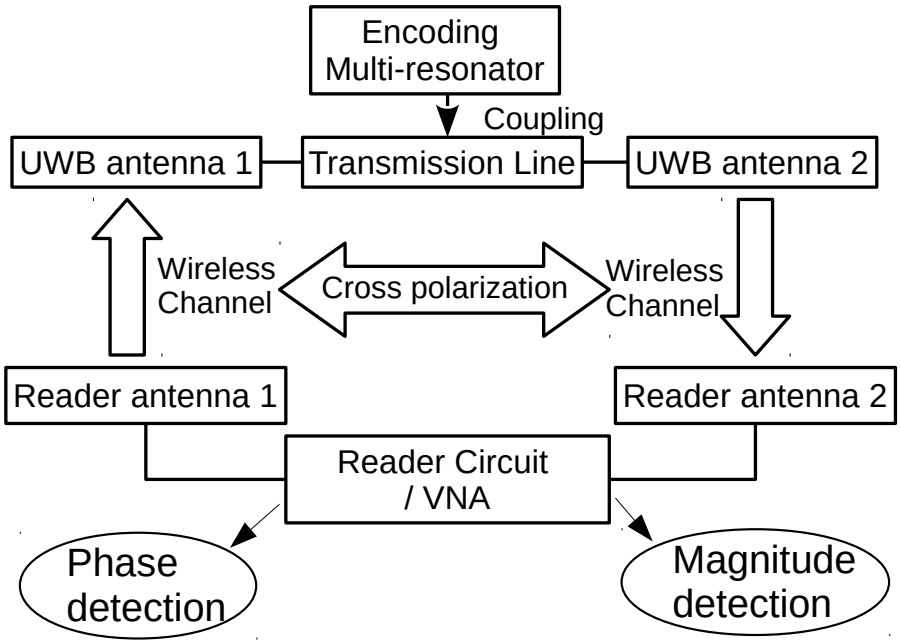

Figure 5.10: Block diagram of the microfluidics-encodable chipless RFID tag operation principle.

Encoding module

The proof-of-concept chipless RFID encoding module in Figure 5.12a consists of three spiral resonators and three microfluidic channels, one on top of each spiral. Multiresonators, especially spiral resonators, are commonly used in chipless RFIDs due to their simple structure and frequency-code capability [131, 133]. By embedding a microfluidic channel in the spiral resonator's gap between adjacent turns, the capacitance of the gap

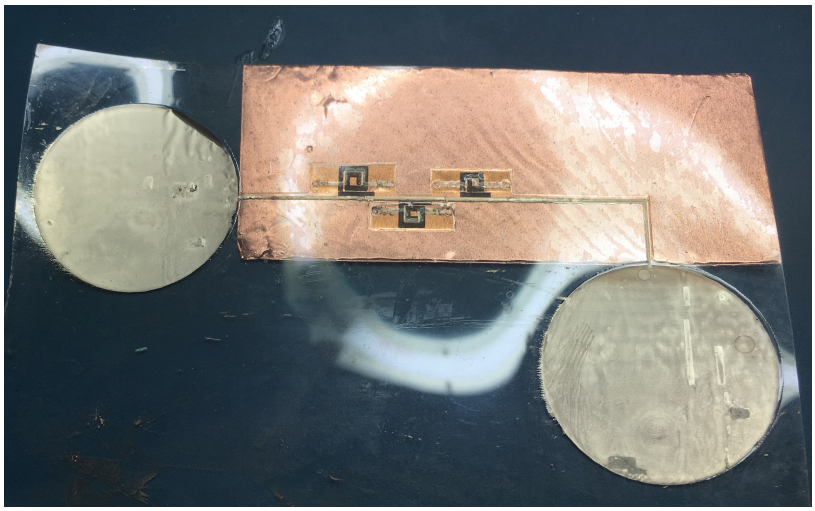

Figure 5.11: Photo of a prototype of all-inkjet-printed microfluidics-encoded chipless RFID tag including the receiving and the transmitting ultrawideband antennas.

can be tuned by changing the status ("filled"/"unfilled") of the microfluidic channel as the relative permittivity of air and water is 1 and 80, respectively[135]. The resonant frequency would shift due to this capacitance change, enabling the encoding mechanism: the original frequency represents code '0' and shifted represents '1'. As the RFID module can be toggled by filling or removing the water (or a different liquid) in the channel, one simple way to achieve that is to cover the prototype with a elastomer adhesive film and press "buttons" in Figure 5.13a and Figure 5.13b. There are numerous other possible passive or active ways to realize this functionality, such as using electrowetting to change the surface tension of liquids or using digital microfluidics to deliver liquid droplets. The three spirals have the sizes of 5 mm by 4.4 mm, 4.4 mm by 4 mm and 4 mm by 3.6 mm with 0.7 mm trace width and 0.3 mm gap between adjacent turns. The signal line width is 0.7 mm, and the embedded microfluidic channels feature 500 μm width and 50 μm height, which requires less than 0.5 μL to fill a whole channel.

To test the encoding capability of the chipless RFID encoding module, the insertion loss (S21) values are measured for all 3-bit code combinations. The measurements agree well with the simulations in the resonant frequencies as shown in Figure 5.14, and the six "code" frequencies of the 3-bit encoding combinations can be found in Table 5.3. In Fig-

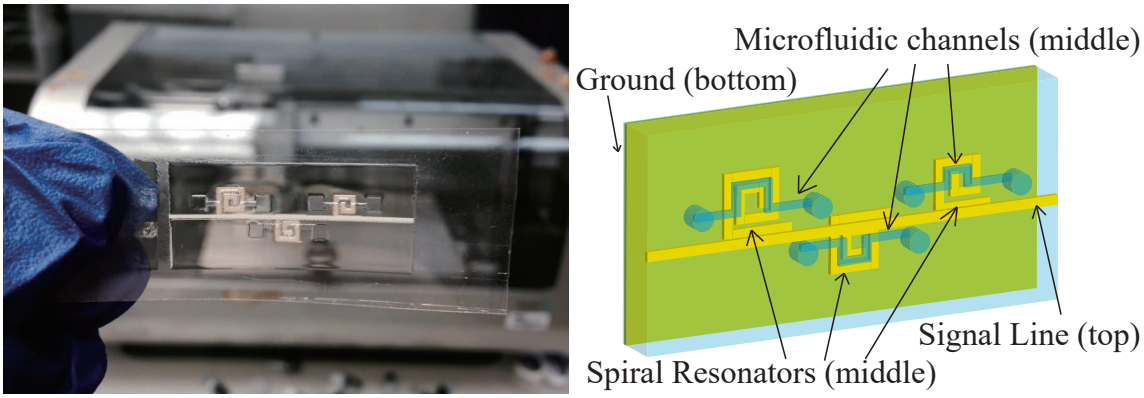

(a) (b)

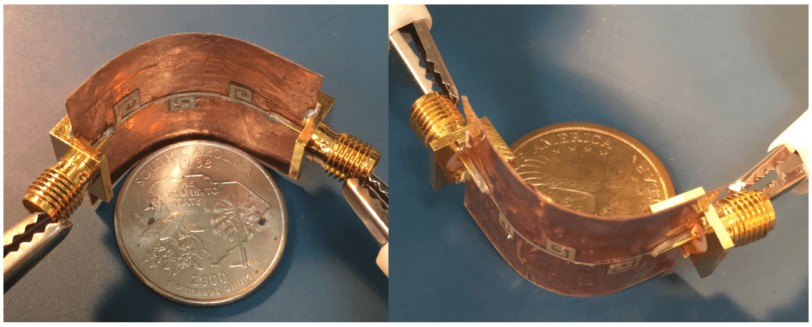

(c)

Figure 5.12: A photo (a) and a drawing (b) of the microfluidics-based tunable chipless RFID encoding module along with two photos of bending in two directions around a dollar coin (13-mm-radius) and a quarter dollar coin (12-mm-radius) in (c).

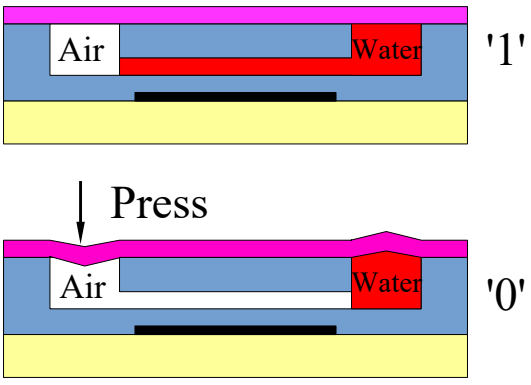

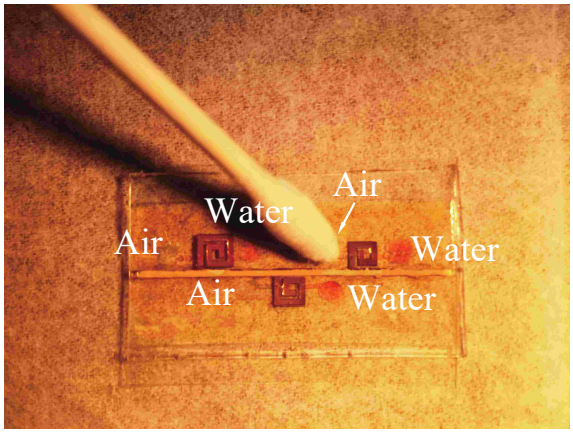

(a) (b)

Figure 5.13: (a) A side view of how to encode the RFID by pressing the "button". (b) A photo of a realization of the above mentioned method by covering the prototype with a Polydimethylsiloxane (PDMS) sheet and pressing the "button" with a cotton swab.

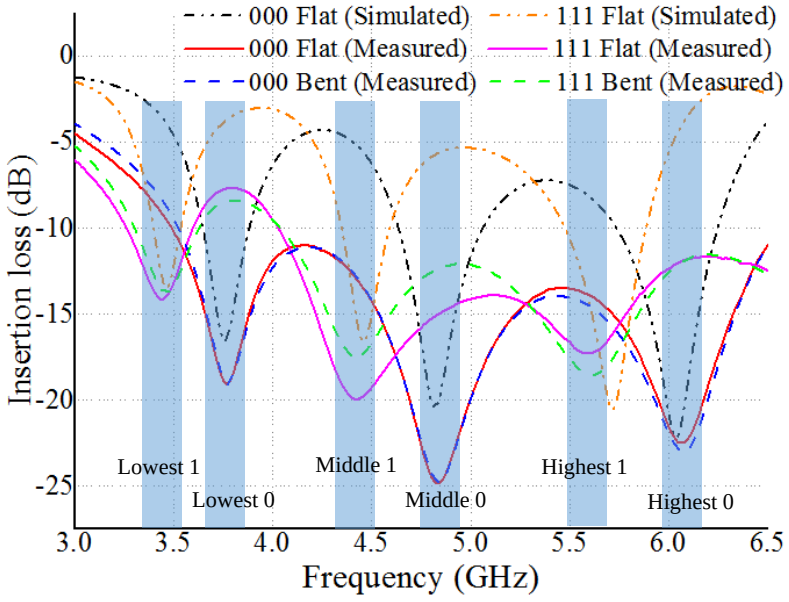

(a)

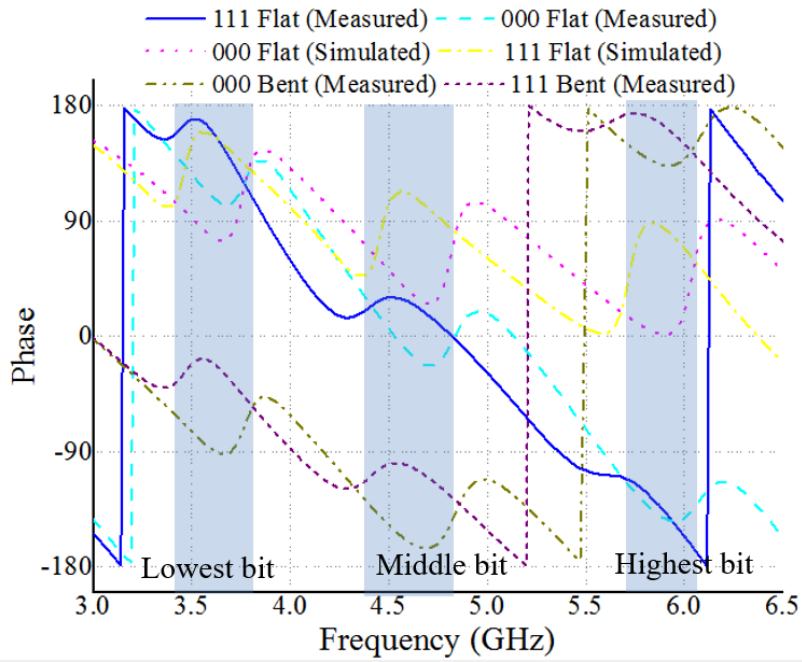

(b)

Figure 5.14: Simulated and measured insertion loss (a) and phase delay (b) values of the prototype for code “000” and “111” configurations in flat or bent for a 30 mm radius.

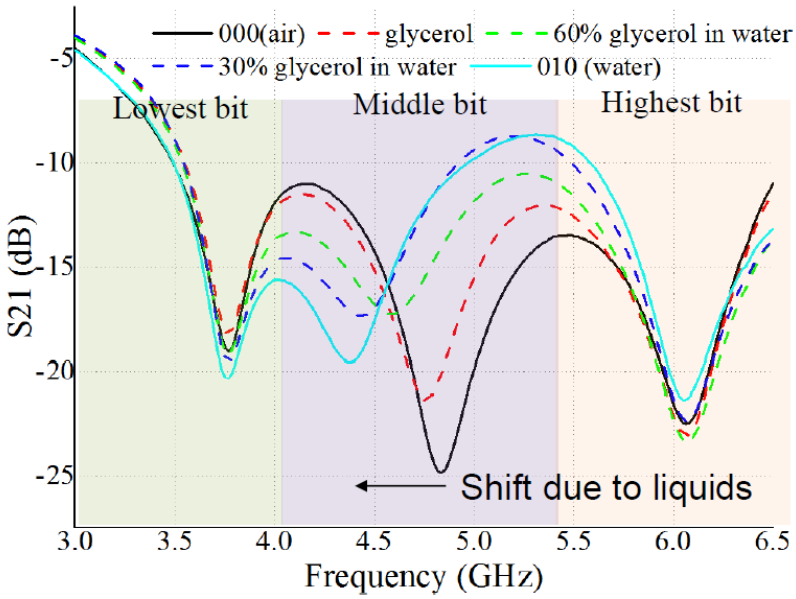

Figure 5.15: Measured the insertion loss values of the prototype with the middle microfluidic channel filled by water glycerol mixtures while other two channels left empty.

Table 5.3: "Code" frequencies for every bit for the proof-of-concept encodable chipless RFID in Figure 5.28

Bit	Code	
	'1'	'0'
Lowest bit	3.44 GHz	3.77 GHz
Middle bit	4.42 GHz	4.84 GHz
Highest bit	5.57 GHz	6.06 GHz

ure 5.16, an at least 8.4 dB insertion loss difference between '0' and '1' can be observed at code '0' frequencies, which facilitates the bit value differentiation. This power difference is smaller at code '1' frequencies, due to the lossy nature of water (especially in higher frequency) selectively filling the microfluidic channels setting the values to '1'. The response at code '1' frequencies can be used as an add-on verification of the bit value, effectively decreasing the bit error rate (BER). Embedding microfluidics in this chipless RFID module empowers the tag to additionally conduct fluidic sensing. Besides magnitude, the phase of the S21 can also show the resonant frequency shift to further increase the reading accuracy. An example can be found in Figure 5.15 in identifying different water-glycerol mixtures

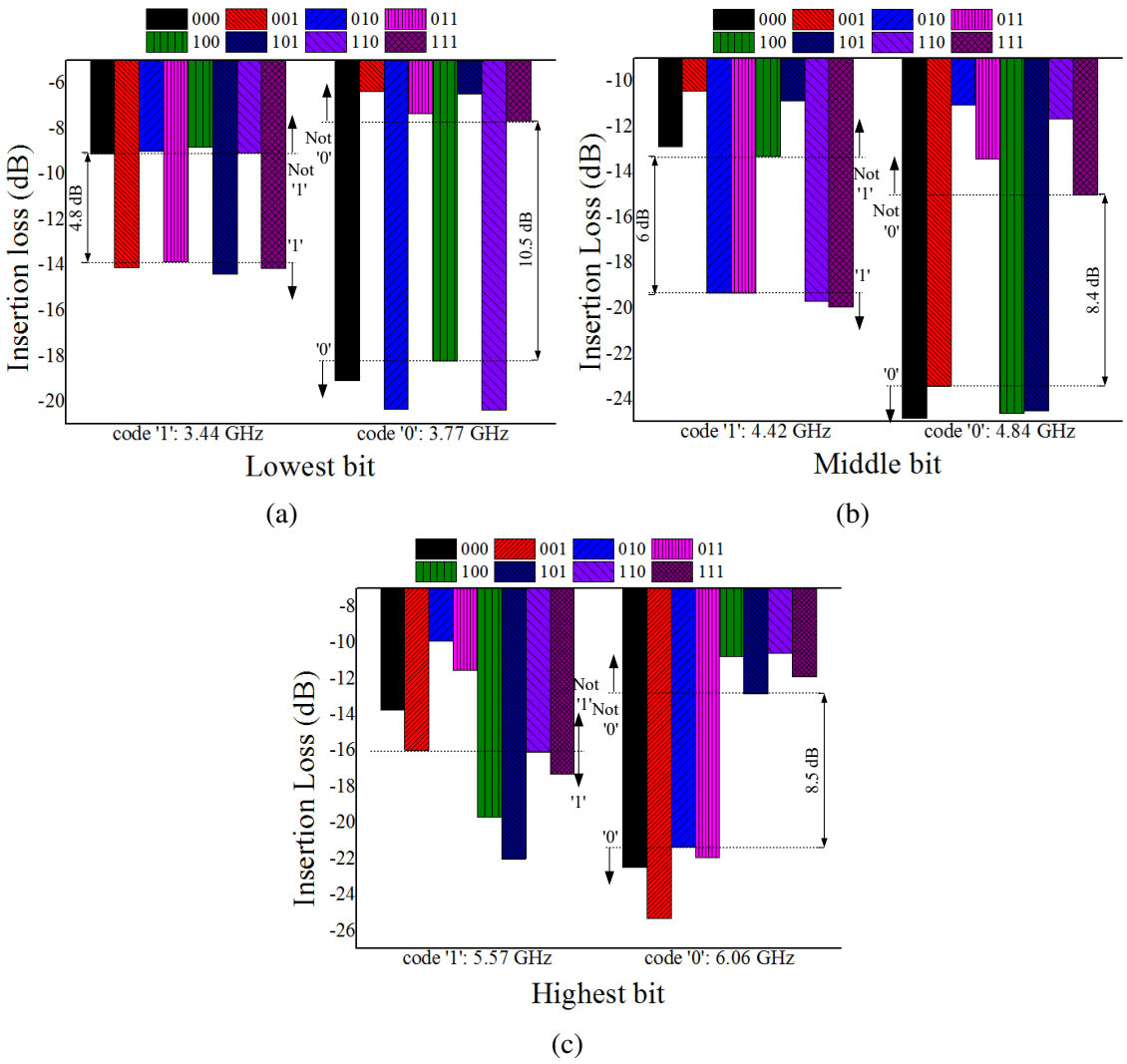

Figure 5.16: Insertion loss of the prototype for various 3-bit code configurations at the coding frequencies of the (a) lowest bit, (b) middle bit and (c) highest bit.

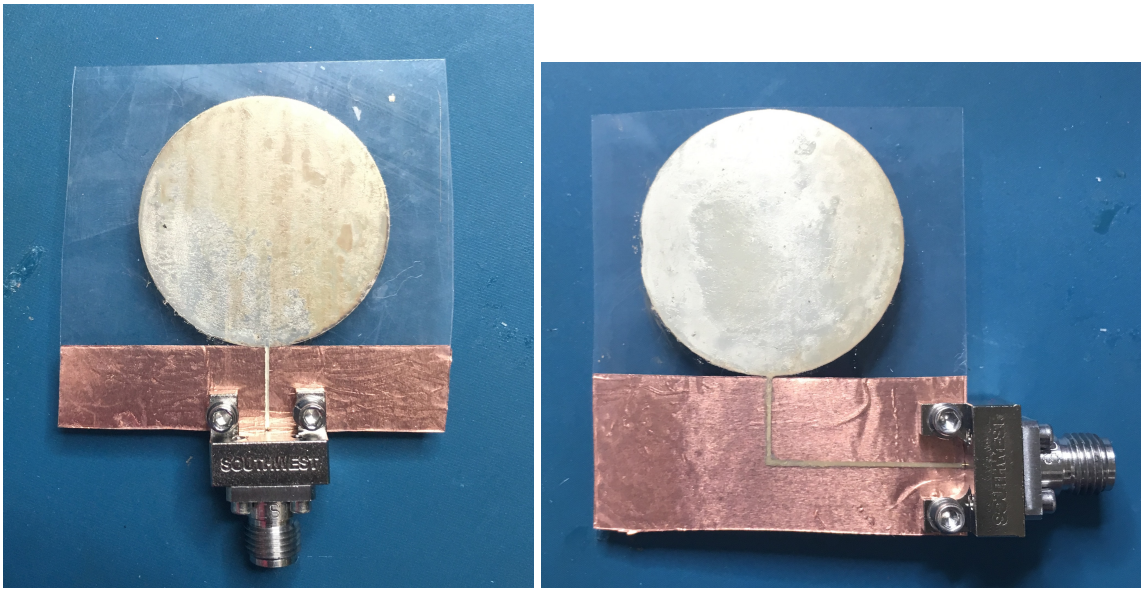

(a) (b)

Figure 5.17: Photos of fabricated UWB monopole antennas for chipless RFID. (a) Monopole antenna 1. (b) Monopole antenna 2.

in a “0X0” configuration with the tested fluid filling only the channel on the middle bit resonator, modifying the resonant frequency of the middle resonator and keeping the other two bits unchanged. As the printed microfluidics and electrodes are extremely thin and the substrate is flexible, the fabricated prototype displays a very stable performance during bending, as shown in Figure 5.14. The prototype can be easily bent for radii down to at least 12 mm without breakage in Figure 5.12c, which enables various wearable and conformal applications.

UWB antenna

Two tag antennas are used to enable an effective wireless interrogation of the multi-resonator-based chipless RFID covering all required ”bit” resonant frequencies. Due to the wide frequency operation range of the multi-resonator encoding module, the tag antennas need to operate at a very large bandwidth: 3 GHz to 6.5 GHz according to the above measurements. Also, in order to minimize the interference between the transmitting and the receiving antennas, they were chosen to be linearly polarized in perpendicular directions due to their different feeding topologies shown in Figure 5.17, thus featuring a relatively high

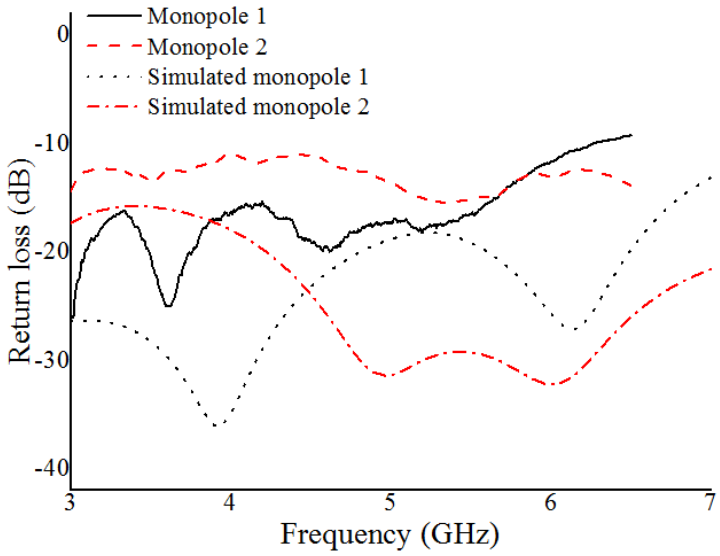

Figure 5.18: The simulated and measured values of S11 of the two ultrabroadband antennas of the chipless tag.

cross-polarized isolation. Moreover, the designated reading direction was perpendicular to the substrate and was aligned with the maximum radiation direction of both antennas. The circular disc monopole antenna topology was chosen as it satisfied the above-mentioned criteria with a simple geometry.

The two 14-mm-radius monopole antennas with perpendicular polarizations were simulated by Ansoft HFSS, prototyped by inkjet-printing technology as shown in Figure 5.17 and then measured with the Rhode and Schwartz ZVA-8 VNA. A 0.4-μm-wide and 9-mm-long impedance transfer microstrip line was added to match both antennas to 50 Ohms. The S11 of the two antennas is shown in Figure 5.18, demonstrating a good radiating performance throughout the whole frequency range of operation. The small differences between the two monopoles can be attributed to the different feeding structures, one of which includes a 90° bend. The gain was measured by two identical horn antenna at a distance of 60 cm. As shown in Figure 5.19, both antennas feature a very wide frequency range of positive gain. The radiation patterns would significantly influence the effective reading area/direction and thus were simulated and measured, as shown in Figure 5.20. A higher than 10 dB cross-polarized isolation in the maximum radiation direction can be easily ob-

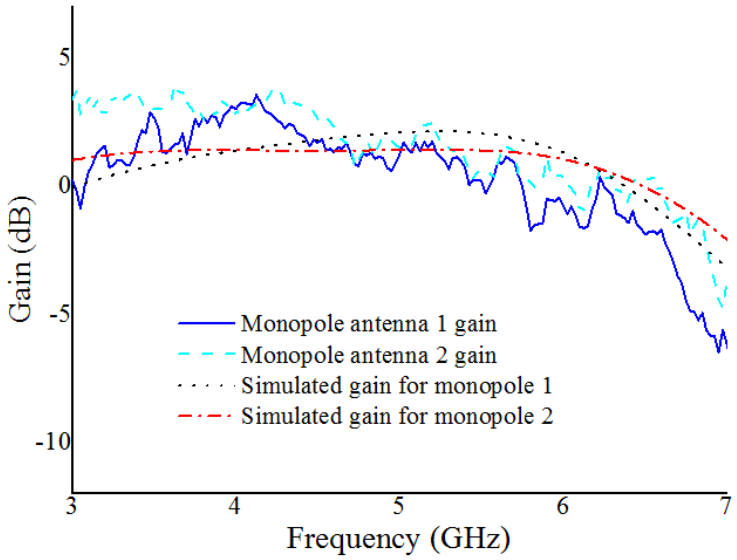

Figure 5.19: The simulated and measured values of the gain of the two ultrabroadband antennas of the chipless tag in the maximum radiation direction.

served.

5.2.2 Phase Modulation: Smart Floating Balls

There are over 80,000 reservoirs in the US, meaning that potential water contamination could have catastrophic health effects. Many reservoirs use floating "shadow balls" to save water by reducing evaporation. What if those floating balls could simultaneously monitor the reservoir water quality and give timely warning? Therefore, we propose the topologies of smart floating balls with spherical antennas on top featuring omnidirectional radiation performance along the plane of water surface along with embedded liquid wireless sensors that are capable of detecting water contamination, such as oil and gas wastewater. These smart floating balls can also be used in other liquid monitoring applications, such as crude leakage in oceans.

The complex dielectric structure shown in Figure 5.21 would be extremely hard to fabricate with any traditional fabrication methods due to the spherical 3D shape, hollow interior and miniaturized microfluidic. However, the complexity of the structure can be easily resolved with a 3D printing technique. The fabrication process contains two steps:

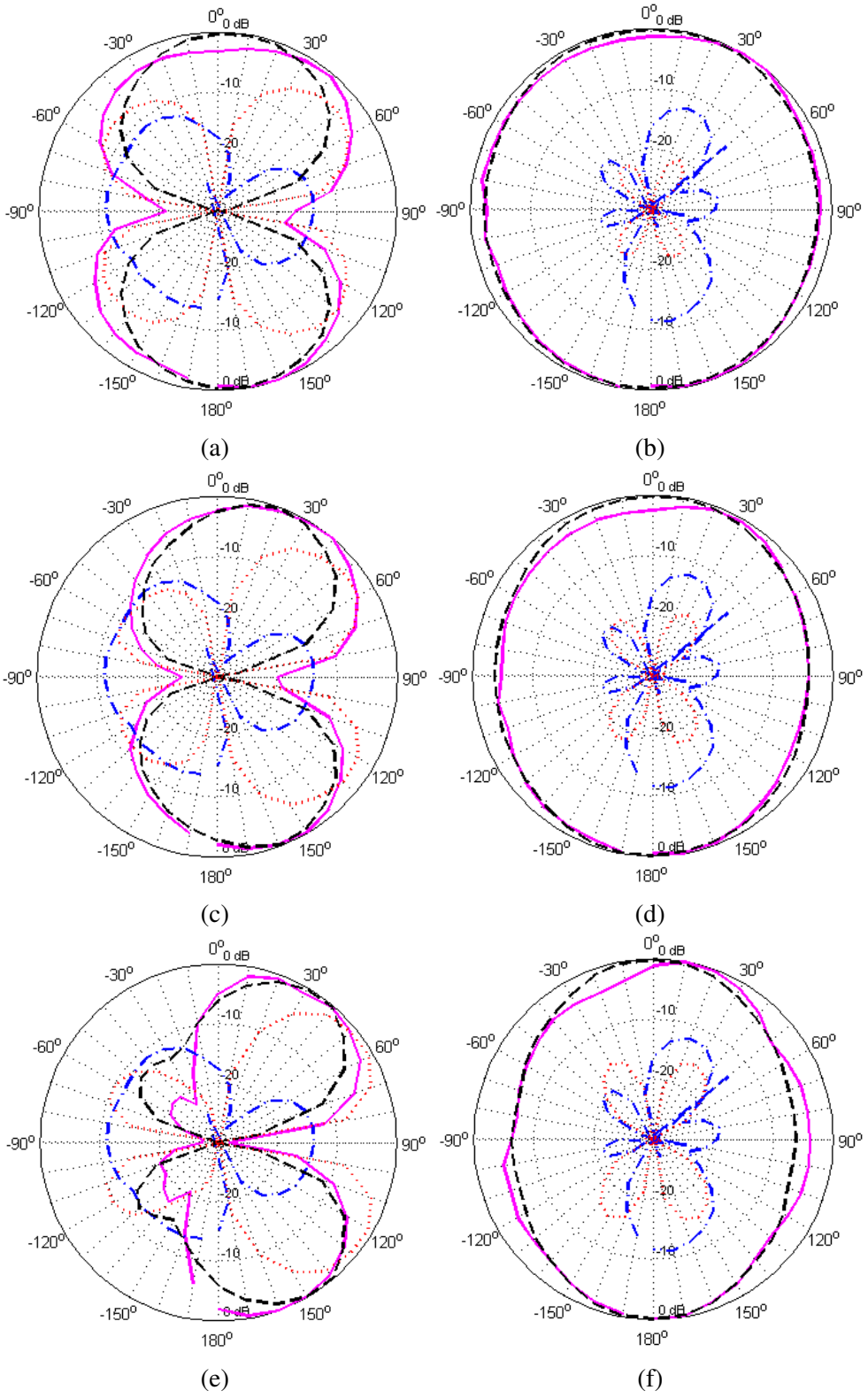

Figure 5.20: Co-polarized and cross-polarized radiation pattern of at 4 GHz, 5 GHz, 6 GHz and 7 GHz. Solid line stands for measured co-polarized radiation pattern; dashed for simulated co-polarized; dash dot for measured cross-polarized; and dot for simulated cross-polarized.

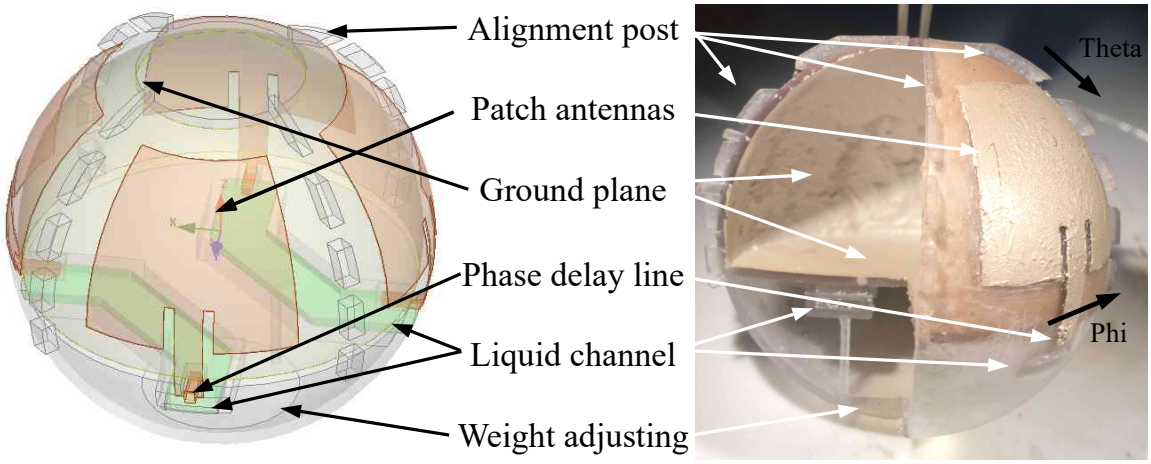

Figure 5.21: A graph of the smart floating ball and a cross-section photo of a proof-of-concept prototype.

printing dielectric structures and then selectively metallizing them. The Form Labs clear resin was used for the dielectric structure, featuring a permittivity around 2.8 and loss tangent around 0.03. The metallization was realized by using the 3D printed stamp method discussed in section 3.2.4. The fabrication of both complex shape smart floating ball and the metallization stamp is carried out by a single low-cost stereolithography (SLA) 3D printer (section 3.2.2), which can largely simplify the process and decrease the cost.

This section demonstrates a smart floating ball consisting spherical antennas and phase delay line sensors, which can be used in the water reservoir to detect the floating water contaminations such as oil and in other liquid monitoring such as crude leakage.

Spherical antennas and Antenna Array

The spherical patch antenna would be an excellent candidate for conformal design and a nearly omni-directional radiation pattern along a plane. In this section, an array of four patch antennas are designed onto a sphere. The spherical patch antennas are 16.2 mm long to work at 5 GHz and 20 mm wide (bottom edge) to enable omni-directional coverage on the water level plane. The bottom edges of the spherical patch antennas overlap with the mid-plane of the sphere to reduce the loss of water and adjust the radiation pattern.

In order to fully characterize the antenna, the two models shown in Figure 5.22 are fabricated and measured with results demonstrated in Figure 5.23 and Figure 5.25, respec-

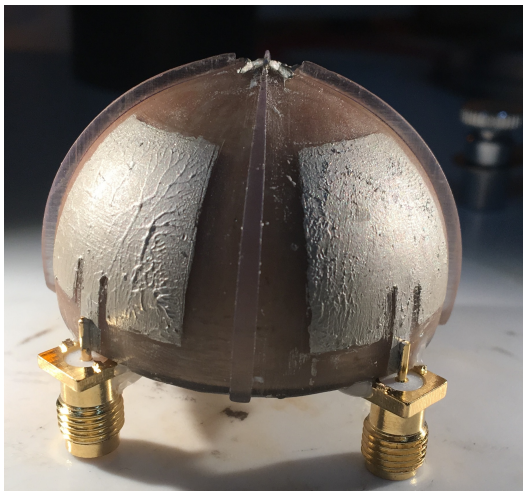

(a)

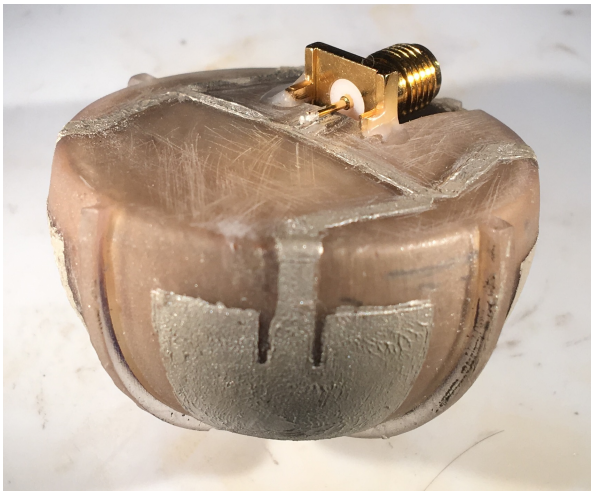

(b)

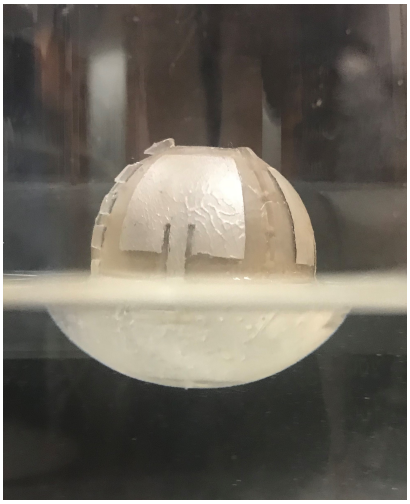

(c)

Figure 5.22: Photos of fabricated prototypes of (a) four spherical patch antennas, (b) a 4×1 patch array around the top hemisphere interconnected with a power splitter on the bottom plane, and (c) a smart floating ball based on the spherical patch antennas floating on water.

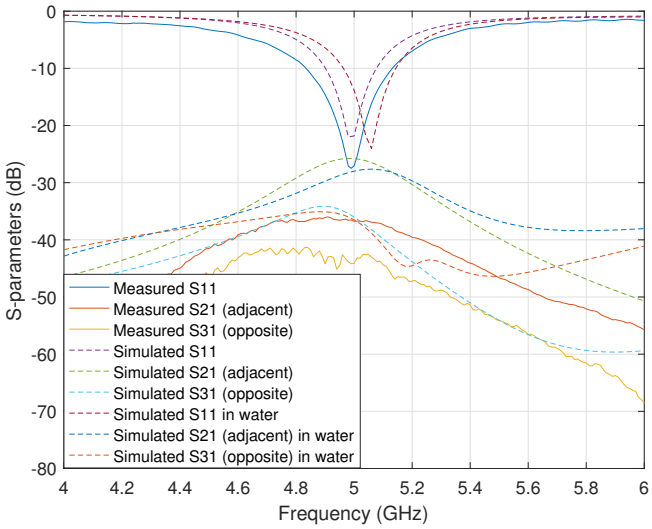

(a)

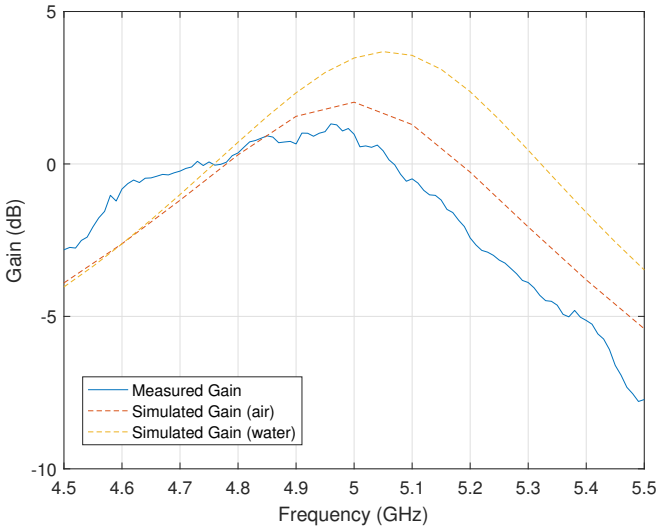

(b)

Figure 5.23: Performance of the four antennas on the sphere. Measured and simulated values in air and simulated values in water for (a) return loss of the antenna and coupling between antennas, (b) gain.

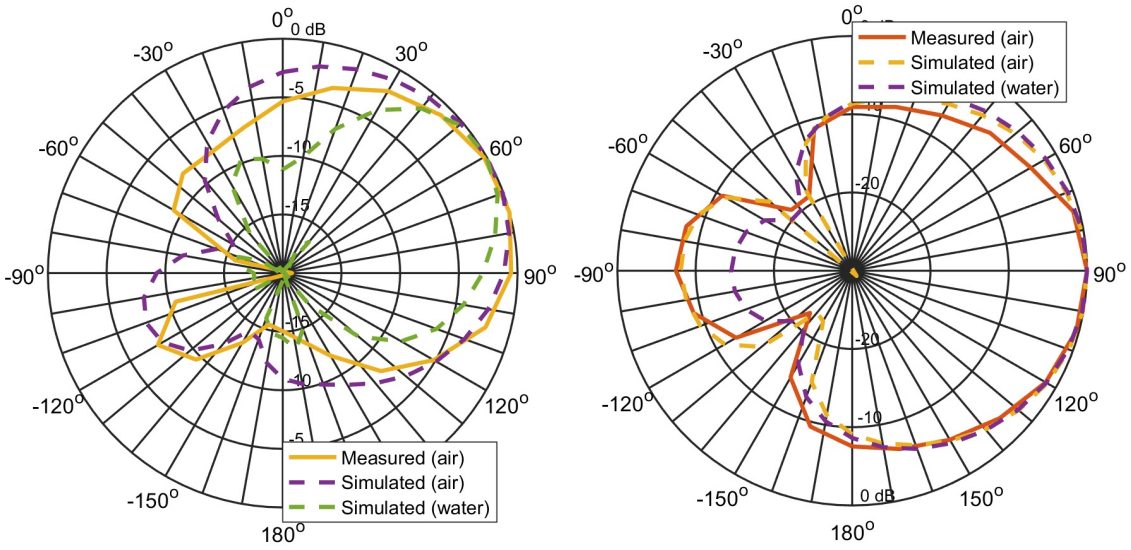

Figure 5.24: Performance of the four antennas on the sphere. Measured and simulated values in air and simulated values in water for normalized radiation pattern (a) in phi=90° and (b) in theta=90°.

tively. Figure 5.23a shows both a great matching of the spherical patch antenna and more than 30 dB isolation with the antennas on the adjacent and the opposite sides. The higher resonant frequency in Figure 5.23a and the higher gain in Figure 5.23b featured by a ball partially submerged in the water are due to the high conductivity of the water that functions as an extended ground plane making the antenna more directive. This can be seen in the radiation patterns in Figure 5.24a and Figure 5.24b as well. To feed the four antennas with an equal phase, a 5-port power spliter is designed with 1.5 mm width for the quarter-wavelength impedance transformer and 0.7 mm width for the 100 Ohm microstrip line as shown in Figure 5.22b. The array is well matched as shown in Figure 5.25a and the measured gain agrees with the simulations as well in Figure 5.25b. Figure 5.26a shows a very good gain for theta from 45° to 75°, which is effectively pointing above the water level and aiming to the shore/dam where the reader can be easily set up. Figure 5.26b shows an omnidirectional gain over the phi direction enabling reliable communication no matter how the ball rotates along phi. This antenna provide a diversity in terms of space/direction which can be used in multiple-input and multiple-output (MIMO) applications.

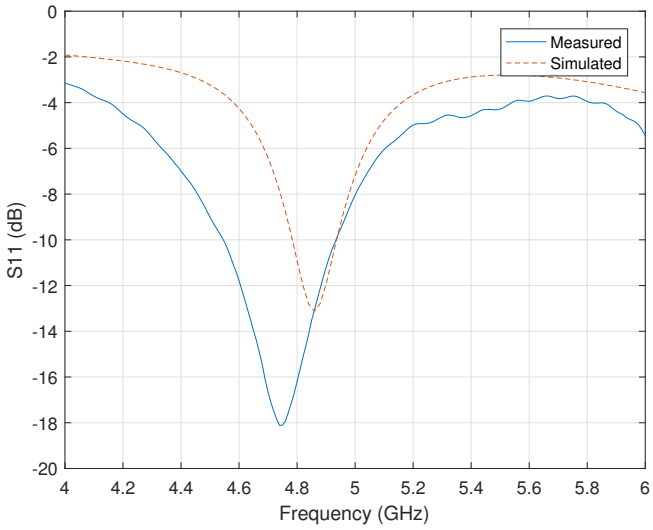

(a)

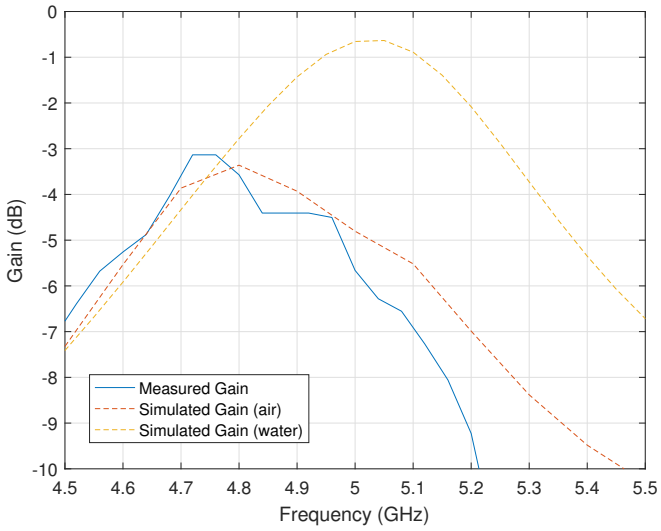

(b)

Figure 5.25: Performance of the antenna array on the sphere. Measured and simulated values in air and simulated values in water for (a) return loss of the antenna and coupling between antennas, (b) gain.

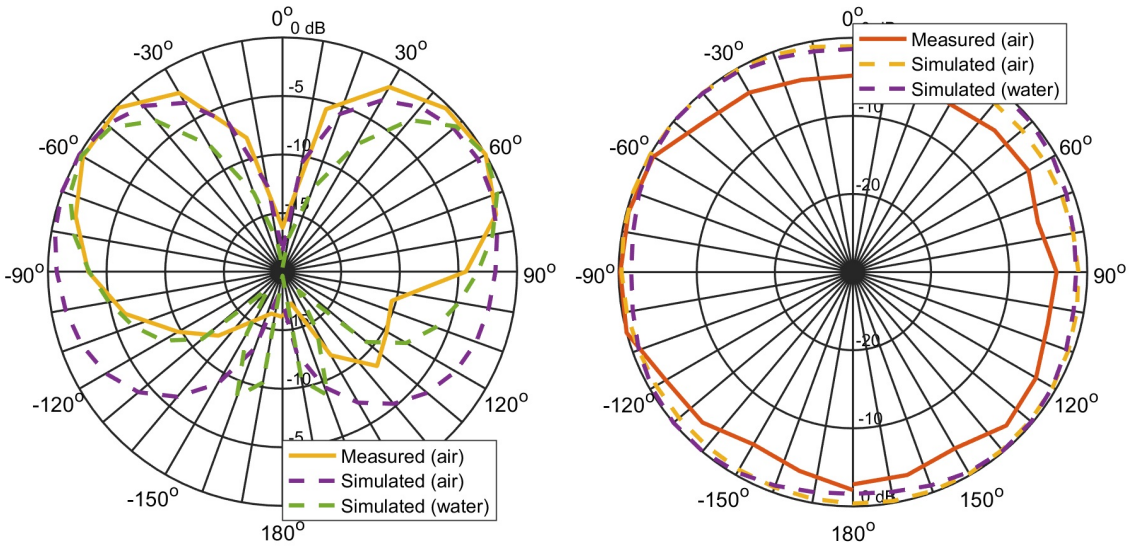

(a) (b)

Figure 5.26: Performance of the antenna array on the sphere. Measured and simulated values in air and simulated values in water for normalized radiation pattern (a) in phi=90° and (b) in theta=90°.

Phase delay line sensor

A liquid-reconfigurable microstrip line topology including a signal line that is 3mm long with a cross section of 1mm × 1mm and a distance of 1.6mm from the horizontal ground plane (Figure 5.27a) is designated as a reconfigurable phase delay line sensor. As shown in Figure 5.27, the topology includes a liquid channel on top of the signal line with 0.5mm distance and a ground plane on the bottom. Typical water contamination liquids, especially organic ones such as oil (relative permittivity: 2.64), have a very low permittivity comparing to water (relative permittivity: 78)[19]. This dramatic change in the permittivity leads to a change of the effective permittivity of the microstrip line and thus additional phase introduced by that line. Figure 5.27c shows the measured values of S11 of the phase delay line with the phase shift being almost linearly proportional to the relative permittivity values (e.g. 30 degrees for an oil-filled channel). Therefore, by using this phase delay line to monitor the permittivity value of the liquid filling the channel, we can monitor if the water is contaminated by the oil or not.

Chipless RFID Operation

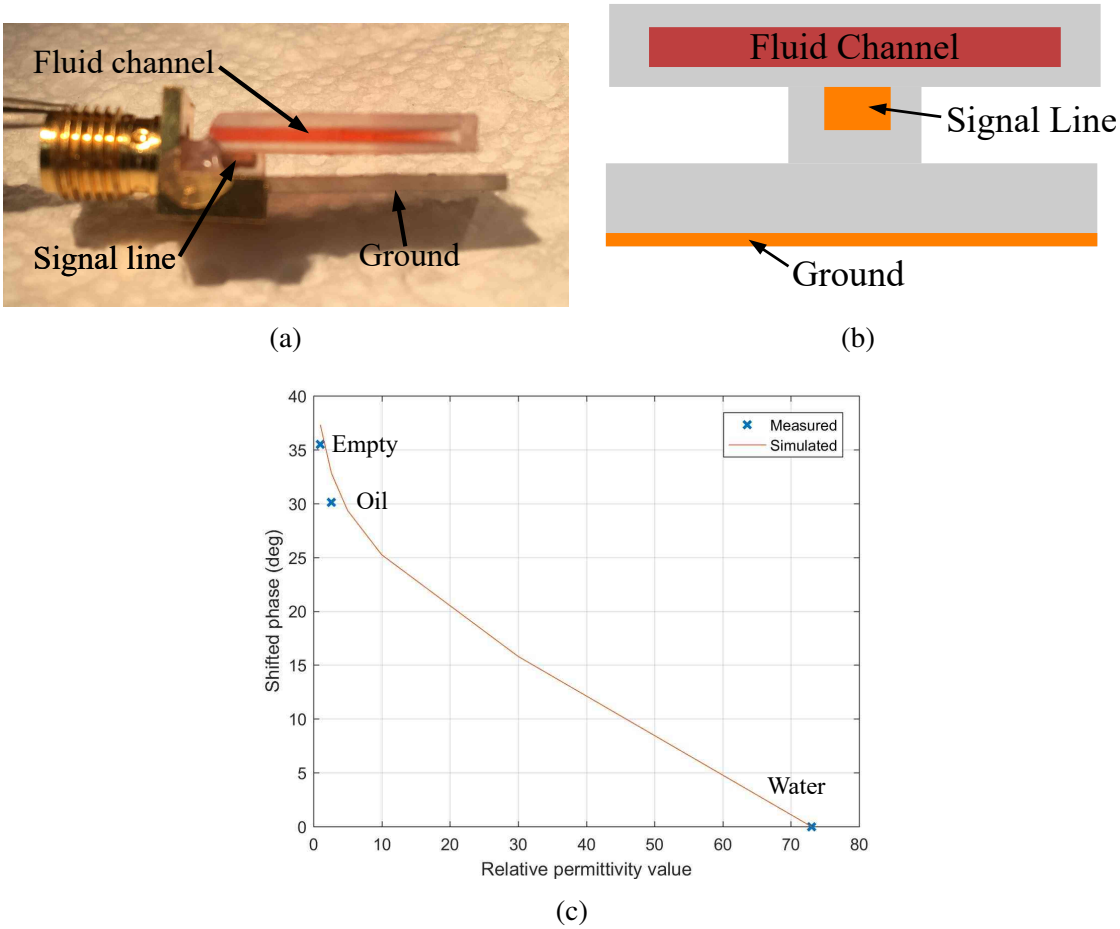

Figure 5.27: (a) A photo of the phase delay line liquid sensor with red dyed water inside the 3D printed microfluidic channel. (b) A cross-section view of the phase delay microstrip line sensor. (c) Measured and simulated phase shift for different permittivity liquids inside the channel.

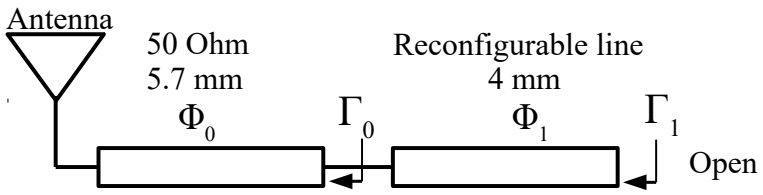

Figure 5.28: Circuit schematic of the chipless RFID.

The spherical patch antenna on the top hemisphere and the phase delay line in the bottom hemisphere serve for communication and sensing purposes, respectively, effectively collecting and transmitting the contamination information in a chipless RFID fashion, as shown in Figure 5.21. By adjusting the weight on the bottom of the ball, as shown in Figure 5.21, the water level is designed to be right above the fluid channel and beneath the antenna feeding microstrip line as shown in Figure 5.22c. In this way, the loss induced by water can be reduced and the contamination on water surface can be easily detected by the phase delay line sensor, that is folded towards the center of the ball so that the sensor is sensitive only to the liquid inside the channel without being sensitive to waves. Phase calibration can be performed effectively by utilizing the phase of the reflection coefficient at the interface between the antenna feeding the 50 Ohm line and the reconfigurable phase delay line as a reference phase[136]. Figure 5.28 shows an example circuit schematic of the equivalent chipless RFID configuration consisting of a reconfigurable phase delay microstrip line that is connected to the spherical patch antenna through a 2.7-mm wide and 5.7-mm long 50 Ohm microstrip line. The phase Φ_0 of the reflection from Γ_0 between the two microstrip lines is not related to the liquid inside the channel while the phase Φ_1 of the reflection from Γ_1 between the phase delay line and the open termination changes with the permittivity of liquid inside of the channel. In this way, by dividing Φ_0 from Φ_1, the phase difference induced by the phase delay line can be calculated.

5.3 Summary

This chapter shows three proof-of-concept RFID sensor tag designs: the "smart test strip", the "encodable" chipless RFID, and the "smart floating balls". The former one uses a passive RFID with chip while the latter two take two different chipless approaches: frequency modulation using a multi-resonantor and phase modulation using a phase delay line, respectively. The former two are accomplished by inkjet-printing, a low-cost additive manufacturing method, which allows for a disposable, lightweight, flexible, scalable, and time-and-effort-efficient fabrication, while the latter one uses 3D printing and a 3D stamp approach for complex 3D shape manufacturing.

The "smart test strip" is a novel low-cost wireless platform for comprehensive next-generation liquid sensing that combines uPAD (paper-microfluidics) and RFID technologies[137]. This platform enables the integration of multiple chemical and electrical sensors, thus multi-functional, highly reliable and comprehensive liquid sensing can be realized. IDEs based on inkjet-printed electrical sensors were presented and evaluated with an excellent capability to distinguish sodium chloride solutions of different concentrations and various organic liquids. Proof-of-concept RFID/NFC tags at 13.56 MHz and 2.4 GHz were designed and an NFC-based smart test strip was measured with a commercial reader featuring 1.33 Ω average minimal detectable resistance change in the range from 0 to 1300 Ω. The proposed smart test strips could find numerous applications, that would include, among others, manufacturing control, water quality monitoring, and point-of-care medical diagnostics.

The "encodable" chipless RFID is a novel way to enable encoding chipless RFID with microfluidics-based tunable multi-resonators on-the-fly[120]. Three microfluidics-based reconfigurable spiral resonators are used to obtain tunable "code" frequencies and encode the RFID with less than 0.5 μL of water per bit. Two inkjet-printed cross-polarized ultra-wideband (UWB) circular disc monopole antennas are utilized to enable wireless opera-

tion. The proposed chipless RFID tag is capable of sensing various fluids (e.g. identifying different water-glycerol mixtures) while featuring a good flexibility. Both the phase and magnitude information of the backscattered signal can be used in identifying the code independently. The proposed encodable chipless RFID tag can be used in various applications, such as Lab-on-Chip (LoC) and Internet-of-Things (IoT).

The "smart floating ball" uses a chipless RFID phase modulation configuration along with spherical patch antennas and phase delay microstriplines that are sensitive to the liquid content[138]. The spherical patch antenna array provides omni-directional gain in the water level plane and can be used in MIMO applications in the water. The phase delay line utilizes a microfluidic channel embedded into the microstripline so that the phase introduced by the line can be reconfigured by the liquid inside the channel. The smart floating ball can monitor reservoir water quality while preserving its original function as a "shadow ball" featuring low-cost, light-weight, and battery-less performance, which are important features for massively scalable "smart" systems.

CHAPTER 6

ORIGAMI ANTENNA TREE RECONFIGURABLE ANTENNAS BASED ON LIQUID METAL ALLOY

Antennas are critical components of communication and radar systems, so their common inability to adjust to new operating scenarios can impose significant limitations on system performance. Reconfigurable antennas, on the other side, can adapt to changing system requirements or environmental conditions; they can eliminate these restrictions and provide additional levels of functionality for any system while adding substantial degrees of freedom and functionality to the communication systems [139]. The need of such reconfigurability can be fulfilled by a single reconfigurable antenna or a platform that integrates multiple antennas. However, the single-platform integration of numerous antennas can be challenging due to high interference. To achieve superior reconfigurability than virtually any single reconfigurable antenna while preventing most interference, this section demonstrates the first antennas "tree" configuration: an integration of antennas that feature reconfigurable capability in all aspects, such as frequency, radiation pattern, and polarization.

Liquid metal alloy (LMA), especially Eutectic Gallium-Indium (EGaIn), features a great potential in reconfigurable electronics due to its non-poisonous, high-conductivity, flow-able and stretchable properties [31]. EGaIn is an alloy with 75%wt Gallium and 25%wt Indium, which features a 15.5 °C melting point and a $29.4 \times 10^{-6}\Omega$*cm resistivity that enables high-performance electronic designs [31]. Due to its liquid nature, LMA ensures a "never-fail" bending and self-healing even if cracks occur under extreme folding conditions, which facilitates the realization of rugged flexible/compressible LMA antennas. The bulk viscosity of EGaIn is 1.9910 mPa*s (twice of water, one 4000th of ketchup), which enabling trouble-less flowing in the channels. With the help of microfluidics, a tool that allows the manipulation of small amounts of liquids, LMA can be transferred within

structures of various shapes[109]. Furthermore, unlike all solid materials, liquid metal is stretchable with literally no failure point and is only limited by the channel's stretchability. This excellent flexibility facilitates bending as much as needed, although it could complicate the accurate control of the mechanical deformations of the antenna structure. Reconfigurable antennas based on LMA are investigated in this chapter, which features minimal interference and maximal reconfigurability in different methods.

As an effective solution for mechanical reconfiguration, origami-based radio frequency (RF) structures have been reported both without and with 3D printing [140, 141], in which the breakage along the fold lines is one of the biggest challenges. As mentioned above, the breakage of metal during bending can be effectively resolved through the use of LMA. Moreover, to reduce the stress of substrates along the fold lines while maintaining the correct structure, a Voronoi topology is introduced to the microwave structures for the first time. A Voronoized shape is an equivalent "skeleton" (frame) of original continuous solid structures using the Voronoi graph of boundary points, which provides a lightweight representation of objects with much less material [142].

The "tree" structure combines LMA microfluidics channels, 3D antenna structures, and origami Voronoi supports, which lead to a rather sophisticated 3D topology, which is hard to fabricate with conventional fabrication methods. However, with 3D printing, the structure can be easily fabricated in a cost efficient and fast prototyping fashion which allows various on-demand antennas to be integrated on the same antennas "tree" within hours.

This chapter presents the first-of-its-kind 3D printed antenna "tree" that can integrate virtually any antenna and is capable of reconfiguring in frequency, radiation pattern and polarization by filling/unfilling the LMA or folding/unfolding the origami scaffolding structure, enabling numerous potential applications including wireless communications, flying and space platforms, collapsible/portable radars, and satellite communications. First, a simple FDM 3D printed LMA reconfigurable helical antenna is studied. Then, an advanced helical and zigzag antenna tree is carried out with SLA printing based on the initial proto-

type. Finally, a “Chinese Fan” bowtie antenna is presented.

6.1 Initial Prototype of Helical Antenna

An axial-mode helical antenna is a 3D directional antenna with circular polarization. The directivity (or maximum gain) of the antenna is closely related to the number of turns of the helix. The mathematical approximation [143] is

$$D_{dB} = 11.8 + 10log(N) + 10log(C^2 S/\lambda^3) \tag{6.1}$$

where N is the number of turns, C is the circumference, S is the spacing between turns and λ is the wavelength. The directivity of the antenna grows with the number of turns as the current in the increased turns would direct the radiation power to the end of the helix (end-fire).

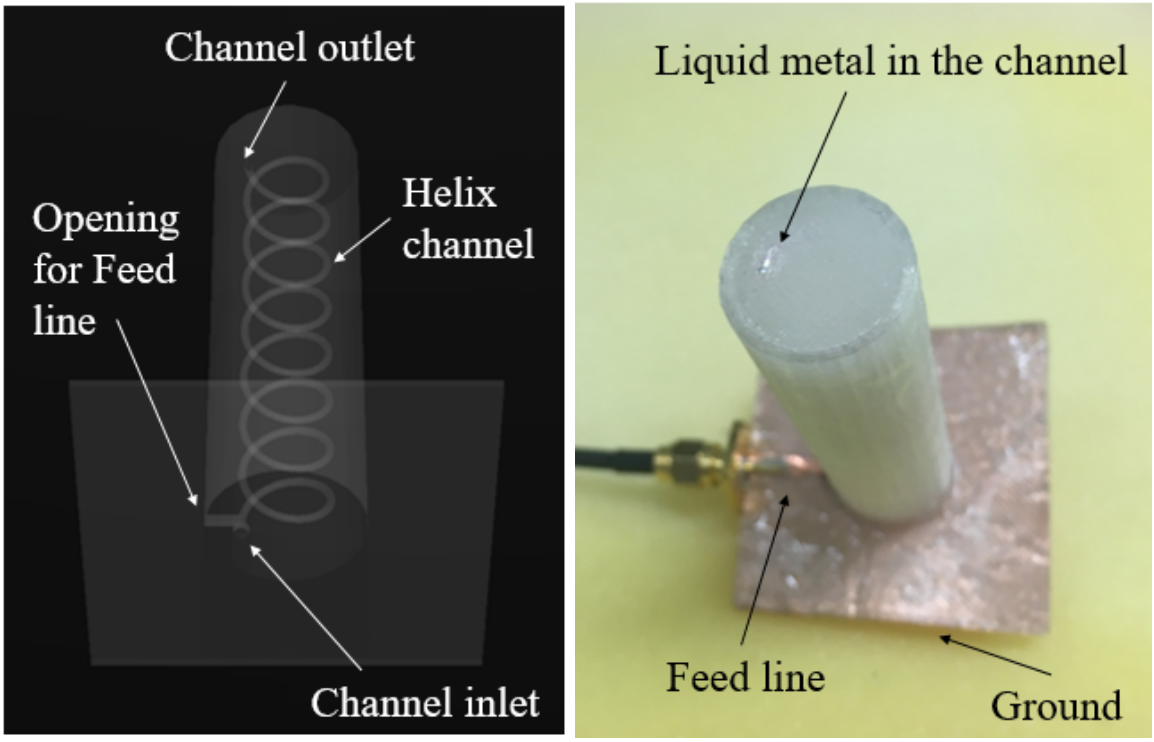

(a) (b)

Figure 6.1: Geometry (a) and photograph of a fabricated prototype (b) of the proposed helical antenna.

In this design, a cylinder on a square base with a helix channel inside is 3D printed, as shown in Figure 6.1. By filling the LMA into the channel from the inlet to the bottom, a helical antenna can be built. Thus, the number of turns is determined by the volume of LMA filled, so the gain of the antenna can be controlled in use. With NinjaFlex ($\epsilon_r = 2.95$ and $tan\delta = 0.06$)[107] used, the helix radius is designed as 5.5 mm with a pitch of 8.7 mm to work at 5 GHz. As the diameter of the channel is only 1 mm, the LMA needed for each turn is only 34.6 μL, which is smaller than a drop of water.

As the impedance of the axial-mode helical antenna is much higher than 50 Ohms, a quarter-wavelength impedance transformer is designed and used with its parameters in Table 6.1. To eliminate the distance between the feedline and the channel inlet, the feed line is designed on the top of the 3D printed base, and the ground is attached on the bottom of the base as a microstrip line.

Table 6.1: Parameters for the feed line for the helical antenna in Figure 6.1

Name	Width (mm)	Length (mm)
Transformer inside the cylinder	1.4	4.5
Transformer outside the cylinder	2.2	4.7
50 Ohms line	3.1	10.3

The helical antenna is simulated and optimized with Ansoft HFSS and measured with a vector network analyzer (VNA) and two horn antennas. In Figure 6.2, the gain at working frequency range is shown with gain at full range inserted. There is an approximate 4 dB gain difference between the 8-turn and 2-turn helical antennas. Therefore the proposed antenna features a good tunability, as the directivity value increased by 1.5 times by changing the volume by 0.2 mL. Figure 6.3a shows that the antenna is well matched and resonant around 5 GHz regardless of the number of turns. The ripples at lower frequency are due to the hole in the ground (channel inlet) and varying impedance of the antenna and the feedline at different frequencies. The simulated radiation pattern in Fig 6.3b also demonstrates the directivity reconfiguration of the proposed antenna.

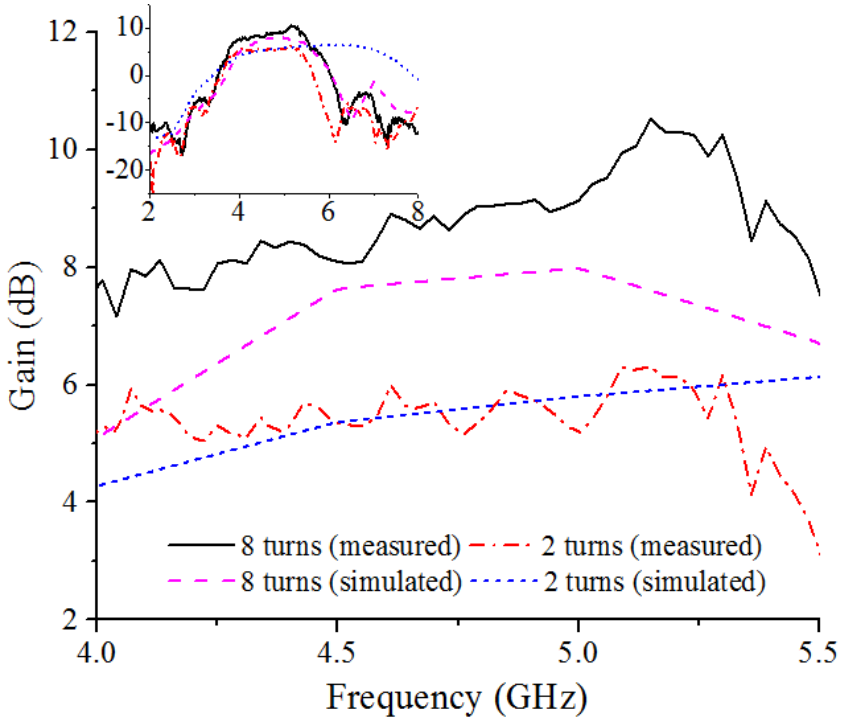

Figure 6.2: Measured and simulated gain value of the helical antenna with different turns of helix filled with LMA.

6.2 Helical and zigzag antenna

Based on the reconfigurable helical antenna in the previous section, a proof-of-concept multiple antenna integrated "antenna tree" can be build by adding another special helical antenna, a zigzag antenna. Figure 6.4 shows the proof-of-concept structure, which can be seen as a tree, while each antenna along with its impedance transformer represents a "branch". All antennas share the same feed, which can be seen as the "root" of the tree, as shown in Figure 6.5b. This antenna tree can be reconfigured in three ways: switching between antennas through the use of microfluidics, tuning the filling volume of LMA, and compressing the origami structure. First, through the use of microfluidics switches, LMA can be easily directed to a specific impedance transformer and antenna while other "branches" are left empty thus preventing any significant interference to the working "branch." In this way, the antennas "tree" can integrate any antenna that can be realized with LMA, while all these antennas can operate independently of each other. As a proof of concept, two "branches",

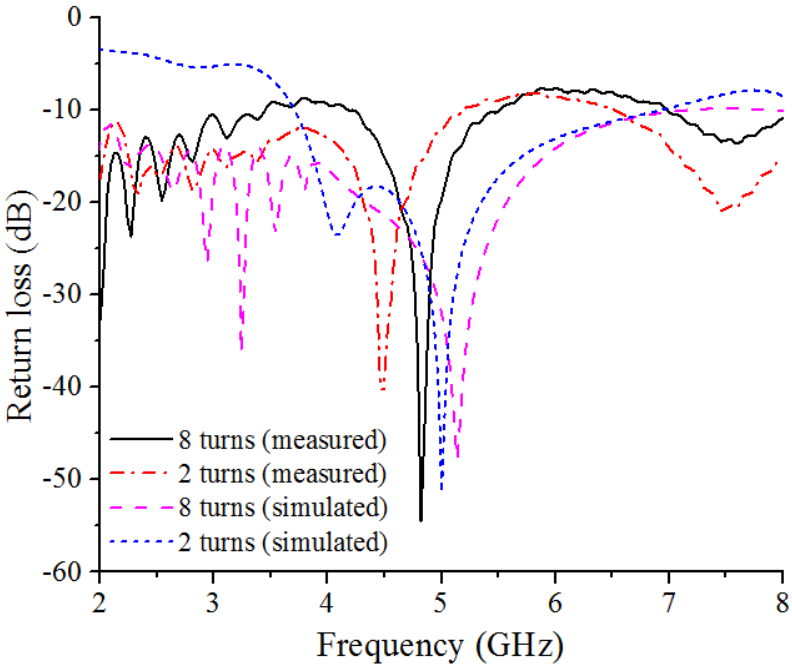

(a)

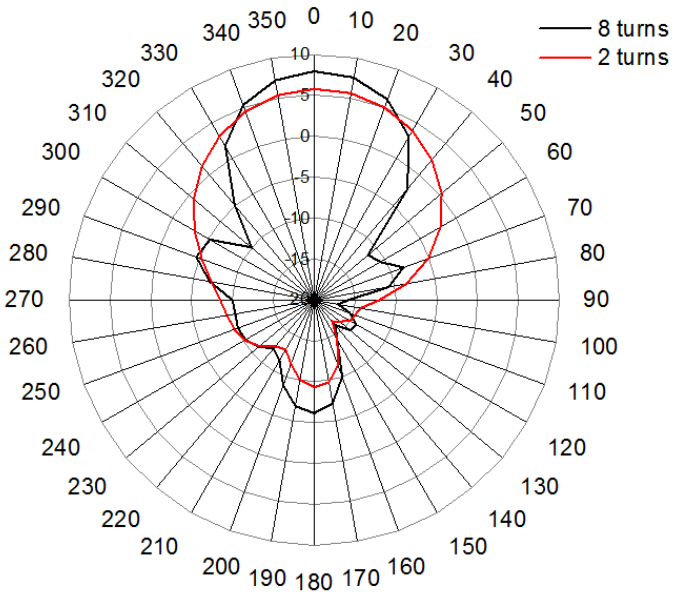

(b)

Figure 6.3: (a) Measured and simulated return loss value and (b) simulated radiation pattern (Unit: dB) of the helical antenna with different numbers of turns of helix filled with LMA.

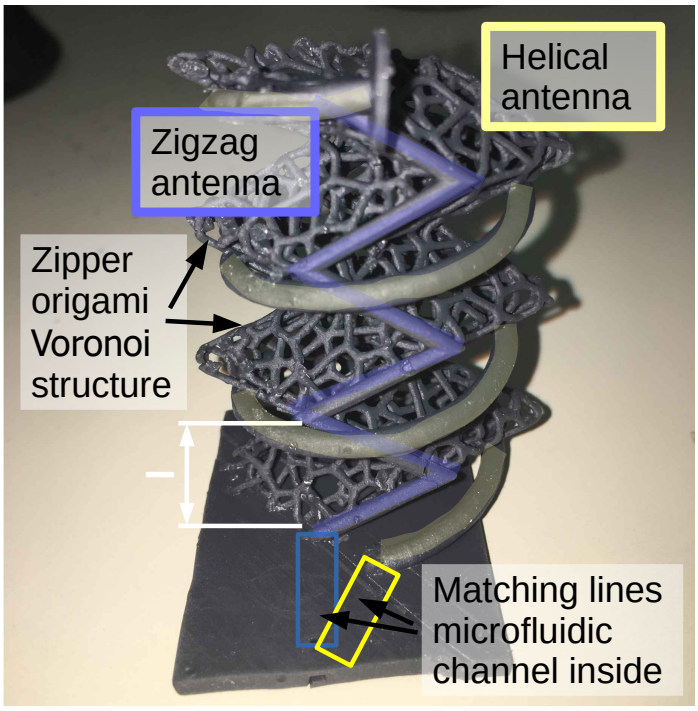

Figure 6.4: A photo of the 3D Printed origami antenna tree. The zigzag antenna and its matching circuit are marked in blue while helical antenna and its matching circuit in yellow.

a zigzag antenna and a helical antenna, are presented as shown in Figure 6.4. Besides switching between the "branches", the proposed configuration can also be used to accurately control the volume of filling LMA (e.g., number of turns), similar to the approach described in section 6.1. For example, for the zigzag and helical antenna, the number of turns of the antenna depends on the volume of LMA, which changing the maximum gain of the antenna. As a result, the gain of the antennas can be tuned [108], by filling different volume. The filling and unfilling of the "branch" can be realized by microfluidics pumps and controlled by microcontrollers.

Without loss of generality and for proof of concept demonstration purposes, a regular helical antenna (circularly polarized) and a zigzag antenna (linearly polarized) were fabricated on the "tree". To obtain different polarization, a regular helical antenna and a zigzag antenna which is a special case of helical antenna with linear polarization, are fabricated in the tree. The two antennas were simulated and optimized with Ansoft HFSS with their dimensions given in Figure 6.5.

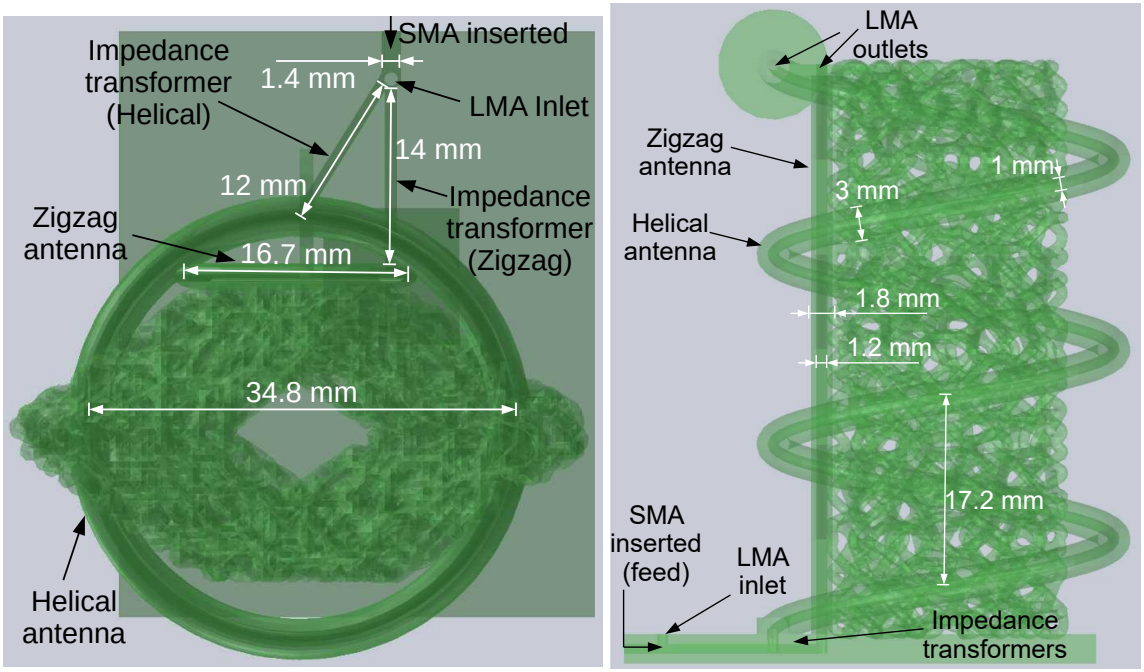

(a) (b)

Figure 6.5: Top view (a) and side view (b) of the 3D model of the proposed "tree" with dimensions. Certain transparency was added to assist understanding of the structure.

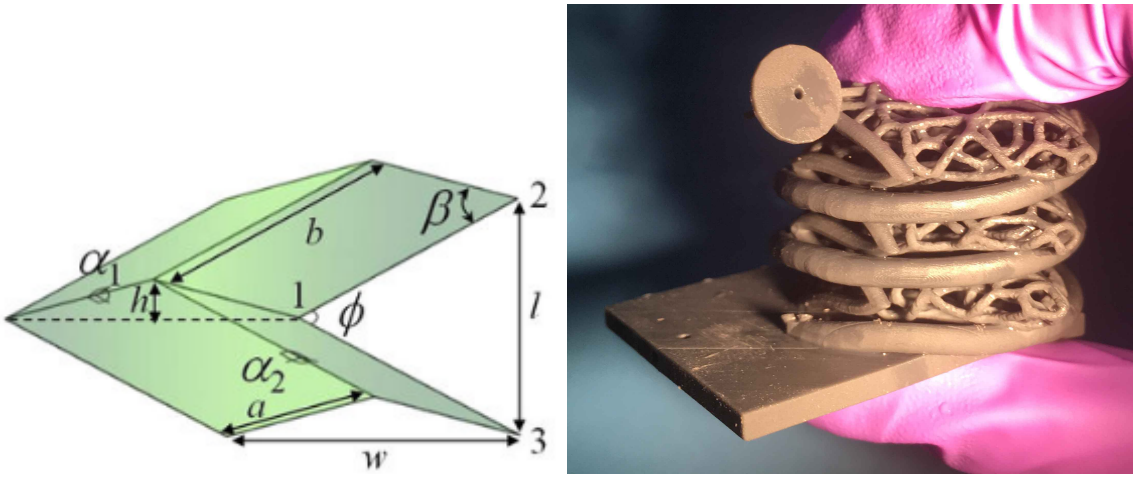

(a) (b)

Figure 6.6: (a) Pattern and parameters of a Miura-ori cell, which is the base for the zipper tube. Reprint from [144]. (b) A photo of a 3D printed zipper-tube in compression.

Table 6.2: Critical angle α and height of each segment for the origami zipper tube in Figure 6.4

Status	$\alpha 1$	l (mm)
Compressed (maximum)	35	7.3
Original	90	17.2
Streched (maximum)	150	23.5

Origami scaffolding with Voronoi

A zipper-tube based scaffolding origami structure is utilized that allows the mechanical reconfigurability of all antennas through mechanical folding and compression. A typical symmetrical unit cell for a zipper-tube is realized by overlapping two symmetry Miura-ori unit cells (Figure 6.6a) along with their edges, and for antennas like zigzag antennas and helical antennas, each zipper segment can be attached to one turn/repeatable element, thus allowing multiple structures to get actuated simultaneously. The height of each segment (l) and the shape of the zipper tube depends on a single critical angle, $\alpha 1$, controlling the compression/stretching status of the "tree" as shown in Table. 6.2 [144], which facilitates the easy tuning of the attached structures. A proof-of-concept three-segment zipper tube origami structure is fabricated to mechanically tune the two "tree" antennas as shown in Figure 6.4.

The dielectric origami and microfluidic structures, as shown in Figure 6.4, are additively manufactured using a stereolithography (SLA) 3D printer, FormLabs form 2, as described in section 3.2.2. FormLabs flexible resin (FLGR02), featuring 80% maximum elongation and great flexibility, was chosen. However, origami structures usually feature hinges with very small bending radius, and the endurance of this material is limited so that the structure may break at hinges after 15-20 times of compression. This issue could not be resolved by simply decreasing the thickness as a thinner wall would largely affect printing performance. Therefore, Voronoi, a topology to reconstruct the model into a skeleton-like structure without changing the macro shape was used to reduce the stress of the material [142] while drastically saving material and production time. Voronoi is texture generated

by randomly selecting seed point and uses the midline between any two adjunct seed as the texture line. Due to the randomness, the structure can be well represented by the texture. After Voronoized the origami structure, more than 200 cycles of compression have been performed, and no breakage was found. Figure 6.6b shows compressing the Voronoized origami zipper tube with two fingers.

Branch No. 1: Zigzag antenna

A zigzag antenna was designed to work at 5 GHz. The prototype was measured with a vector network analyzer (VNA) for the original (uncompressed), maximum compressed and maximum stretched states. The radiation patterns were measured with the setup shown in Figure 6.8. Figure 6.7a shows a good matching for various folding states, which ensures the effective radiation performance of different mechanical reconfiguration states. The respective simulated and measured radiation patterns are shown in Figure 6.9. As the zipper got compressed, the zigzag antenna featured a trend to shift from directional to omnidirectional radiation patterns, and the 3dB beam width (HPBW) increased from 28° (original) to 60° (compressed),

Branch No. 2: Helical antenna

The second antenna is a helical antenna, which features a good impedance matching and a radiation pattern variance for different states of mechanical deformation as shown in Figure 6.7b and Figure 6.10. Similar to the zigzag antenna, when fully compressed, the HPBW of the helical antenna increased from 60° to 90°.

6.3 Bow-Tie "Chinese Fan" antenna

The bow-tie antenna is a simple antenna configuration as well as an extended form of the dipole antennas, which have a wider bandwidth because of the triangle area. The bandwidth of the bowtie antenna depends on the apex angle of the isosceles triangle, as shown in Figure 6.11a. By applying the Chinese fan structure to the bow-tie antenna, the apex angle of the bow-tie antenna can be easily tuned. Therefore, the bandwidth of the bow-tie antenna

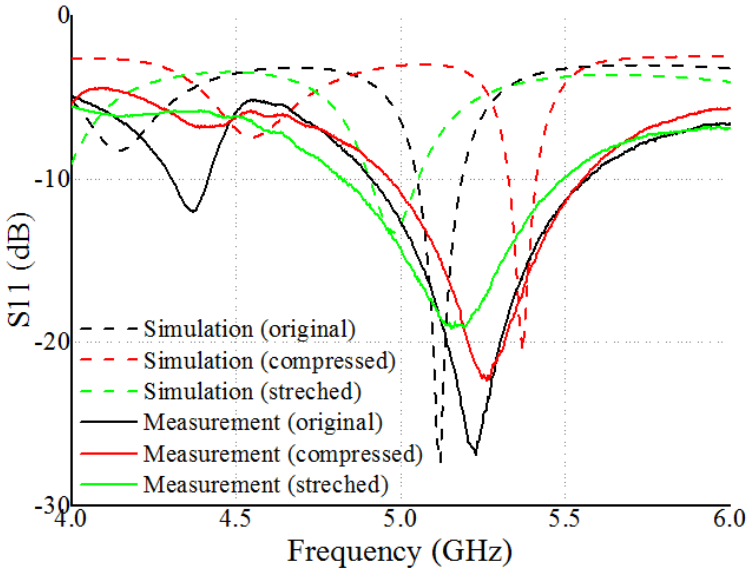

(a)

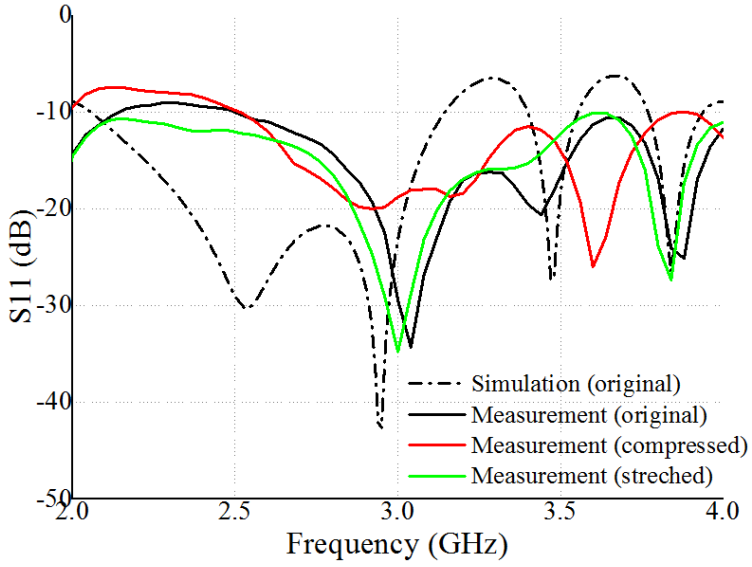

(b)

Figure 6.7: Measured and simulated S11 of the zigzag antenna (a) and the helical antenna (b) under different folding states. The fabricated wall of microfluidics channel is thinner than that in the 3D model which causes the simulated resonant frequencies to be lower than the measured ones.

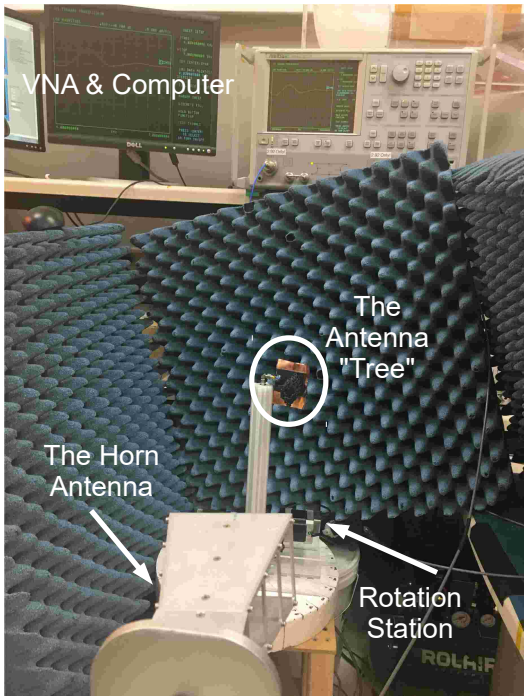

Figure 6.8: Measurement setup for the radiation pattern of the zigzag antenna. A horn antenna and roatation station were used to measure the zigzag antenna.

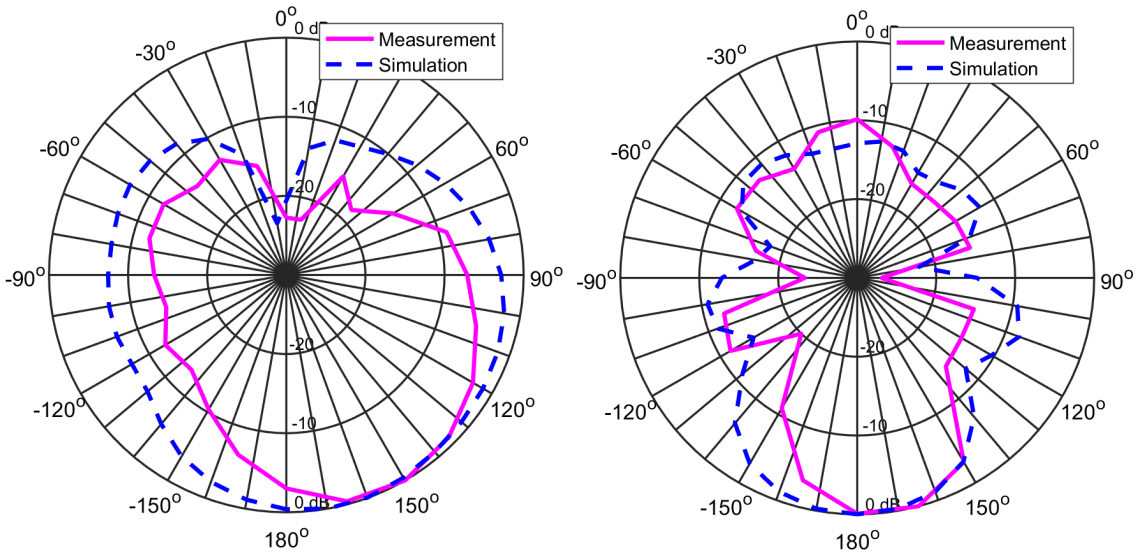

Figure 6.9: Measured and simulated normalized radiation pattern of the compressed (a) and of the original (b) zigzag antenna at 3 GHz.

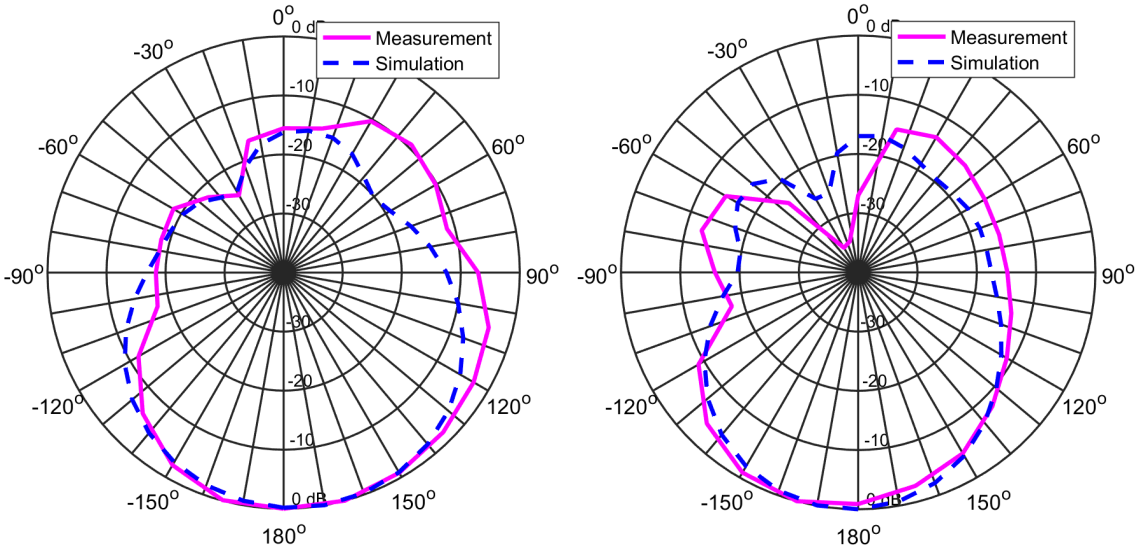

Figure 6.10: Measured and simulated normalized radiation pattern of the compressed (a) and of the original (b) helical antenna at 5 GHz.

can be changed by folding and unfolding the Chinese fan. In the same time, the distance between the two folded triangles can be easily varied by folding the fan sides in different relative angles, so that the resulting capacitance is increasing and the imaginary part of the input impedance is decreasing. That effectively leads to a higher resonating frequency of the structure.

The proposed bow-tie antenna was designed and optimized with Ansoft HFSS simulations with the return loss shown in Figure 6.12 for a 50 Ω. A resonant frequency shift from 896 MHz to 992 MHz can be observed from no compression (80° apex angle) to maximum compression (20°). The bandwidth of the antenna depends on both the real input impedance (imaginary part is 0) and the input impedance slope near that frequency. The -10 dB bandwidth in Figure 6.12 shows the result of both factors. Figure 6.13 shows the slope (the Z_{11} value variance per frequency) from "no compression" to "maximum compression", in which the slope of the real part of input impedance is increased from 0.113 Ω/MHz to 0.149 Ω/MHz (32% increase) while the slope of imaginary part is relatively stable (<7% variance), which generally led to narrower bandwidths for smaller apex angles.

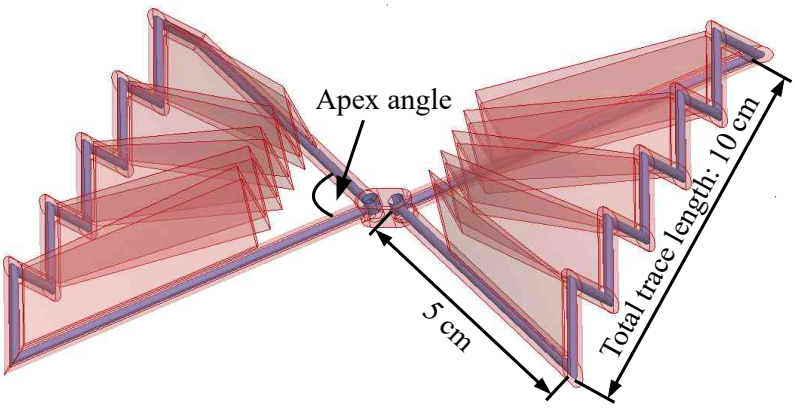

(a)

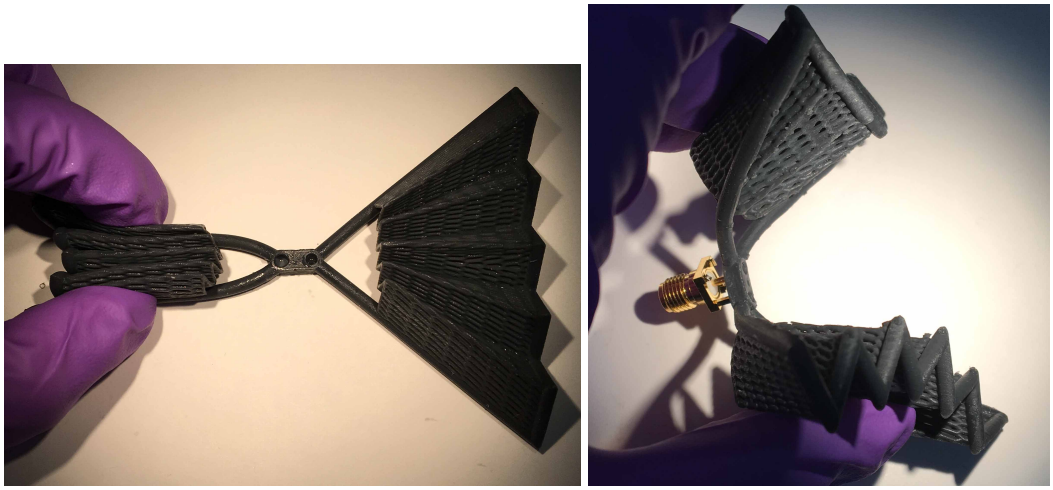

(b) (c)

Figure 6.11: Geometry (a) and photographs of a prototype (b, c) of the proposed "Chinese fan" bow-tie origami antenna. In (a), the red part is the 3D printed origami structure and the blue part stands for the microfluidic channel to contain LMA. In (b), the right fan is in its original state with a 80 degree apex angle and the left fan is compressed by two fingers to achieved a 30 degree apex angle. In (c), the antenna is folded up to show the flexibility.

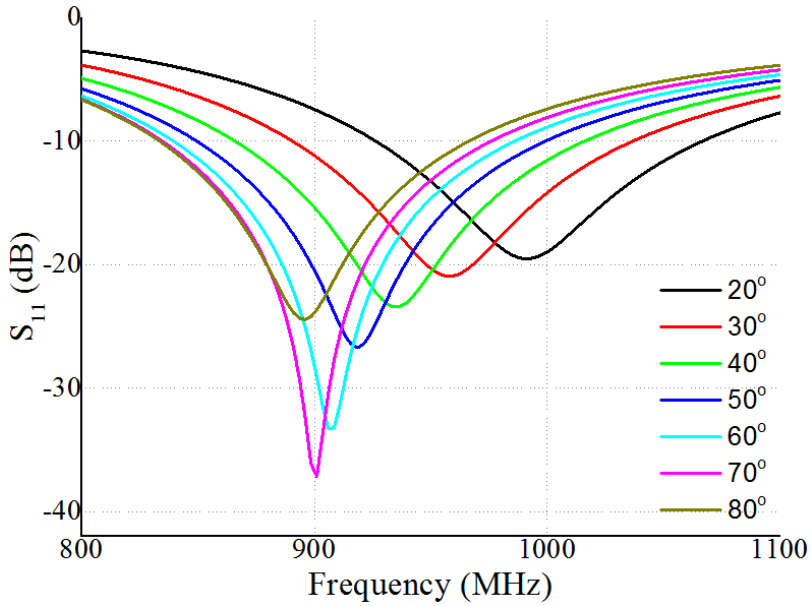

Figure 6.12: S11 of the bowtie antenna for various apex angles.

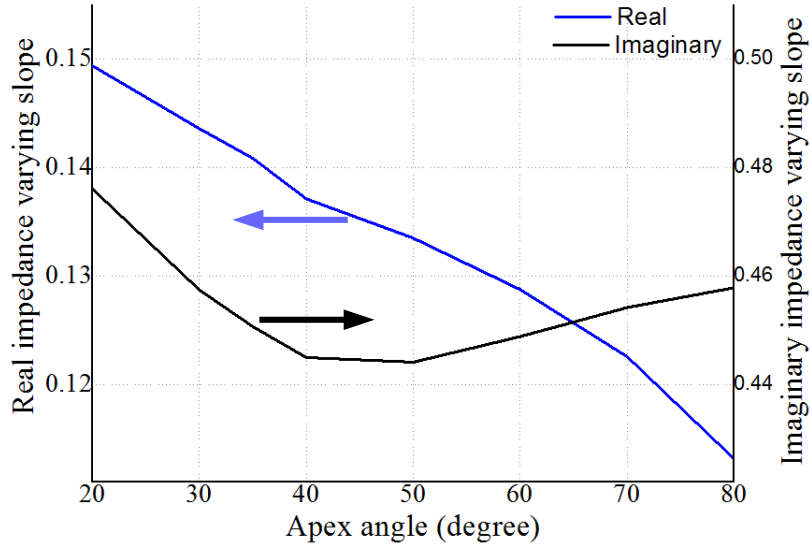

Figure 6.13: The slope, variance of the real part and imaginary part of the antenna input impedance per frequency (Ω/MHz), at the frequency of zero imaginary impedance for various apex angles.

6.4 Summary

This chapter presents the reconfigurable antenna "tree", a novel approach to realize integrated reconfigurable antennas by combining LMA microfluidics and origami structures.

This approach can be realized only through the recent developments in flexible 3D printing technologies that enable the quick prototyping of on-demand 3D foldable/compressible antennas. Three proof-of-concept prototypes are presented. Firstly, a helical antenna with reconfigurable directivity/radiation pattern is designed by changing the number of turns of the helix which can be controlled by the volume of LMA[108]. A more than 4 dB gain increase around 5 GHz is measured with the prototype when the number of turns of helix increases from 2 to 8 (0.2 mL LMA volume change), which demonstrates the reconfigurability of the proposed helical antenna. Secondly, a helical and zigzag antenna is presented, featuring dual-band (3GHz/5GHz) capability and different polarizations (linear/circular) along with varying radiation patterns / 3dB beamwidth (28° to 60° and 60° to 90°) with "tree" compression[145]. An origami structure, the zipper tube, coupled with Voronoi topology implementations is utilized as the scaffolding structure facilitating the mechanical tuning of the radiation pattern while minimizing storage requirements. Thirdly, inspired by Chinese origami fan, a bow-tie antenna featuring a frequency tuning range from 896 MHz to 992 MHz and bandwidth reconfigurability is studied[146]. Overall, this "antenna tree" can effectively adapt to various dynamically changing scenaria and can be potentially applied in wireless communications, flying platforms, collapsible/portable radars, and satellite communications.

CHAPTER 7
CONTRIBUTION AND PUBLICATIONS

7.1 Contribution

This research interfaces additive manufacturing, microfluidics, and microwaves, so the contributions are also listed for the three aspects. Fabrication is the foundation of designs and mainly decides whether the devices can be widely used due to the cost. Microfluidics sensing and reconfigurable electronics are two major applications of these devices, which are essential for the internet-of-things systems.

7.1.1 Fabrication Process

AM process, including both inkjet printing and 3D printing, can facilitate low-cost on-demand environmental-friendly fast prototyping and is one of the keys to ensure the ubiquitousness of the IoT system.

1. Inkjet printing process

    a. Ink characterization

    Two polymer inks, PMMA and SU8, are characterized for the first time. Phenomena such as coffee ring effect of these inks are studied.

    b. Inkjet printing for electronics

    Inkjet printing various silver nanoparticles inks on various substrates, including porous substrates like filter paper and low surface energy substrate like PMMA, are presented for the first time.

    c. Inkjet printing for bonding

Inkjet printing SU8 to precisely bond two substrates, including two PMMA sheets and PMMA with paper, is studied in depth for the first time.

d. Inkjet printing for molding

Inkjet printing molding is presented for the first time that enables fabrication of 2.5D pattern with many thermosetting polymers, including PDMS for soft lithography and microfluidics.

e. Fully inkjet printed microfluidics

The first fully inkjet printing process enables virtually any arbitrary 3D structures including 3D microfluidics, cavities, and overhangs, on virtually any substrates. Comparing to other 3D printing processes, this process enables fabrication of extremely small microfluidics channels that are one-thousandth of other 3D printed channel cross-section areas.

f. Inkjet printed paper microfluidics

The first paper microfluidics process with inkjet printing polymers along with the transition from conventional stand-alone microfluidics to paper microfluidics enables printing various microfluidics structures with the same platform - inkjet printing.

2. 3D printing process

a. 3D dielectric printing

The first attempts at printing microfluidics-based antennas with FDM, SLA printing, which enables fast, low-cost, and on-demand prototypes of 3D reconfigurable electronics.

b. Liquid metal alloy in 3D printed channel

For the first time, the liquid metal alloy is used in a 3D printed dielectric channel as the conductor to enable reconfigurable electronics.

c. Selective metalization of 3D surface

   Two methods, 3D conformal stamp and SAP, are proposed and realized for the first time that can selectively metalize the surface complex 3D shape that can enable complex and conformal 3D electronics.

7.1.2 Microfluidics Sensing

The wireless microfluidics sensors could find numerous applications, that would include but not be limited to, distributed healthcare, lab-on-chip (LoC), manufacturing control, water quality monitoring, and point-of-care medical diagnostics.

1. Passive components

   a. A variety of microwave passive components, including resonators (dual-spiral slot resonators, dual T resonators, and split ring resonators), antennas (patch antenna, loop antenna along with a balun, and slot waveguide antenna), and transmission lines (microstrip line and step impedance low pass filter), are combined with microfluidics and become novel wireless microfluidic sensors. All of them only require a liquid volume less than one drop of water to perform successful sensing.

   b. Resonators shows superior sensitivities compared to the literature, among which the dual-spiral slot resonator features the highest sensitivity as a 44% frequency shift for permittivity from 1 (empty) to 73(water-filled).

2. RFID systems

   a. Comprehensive sensing platform

      The "smart test strip" is the first-of-its-kind platform for comprehensive next-generation liquid sensing that combines uPAD (paper-microfluidics) and RFID technologies. This low-cost wireless platform enables the integration of multi-

ple chemical and electrical sensors. Thus multi-functional, highly reliable and comprehensive liquid sensing can be realized.

b. Frequency modulated chipless RFID

The "encodable" chipless RFID is a novel way to enable encoding chipless RFID on-the-fly, not with a chip but with microfluidics-based tunable multi-resonators.

c. Phase modulated chipless RFID

The "smart floating ball" is the first "shadow ball" that can monitor reservoir water quality while protecting water from evaporation as well as contamination.

7.1.3 Microfluidics-enabled Reconfigurable Electronics

Reconfigurable electronics can easily adapt to changing system requirements or environmental conditions; they can eliminate these restrictions and provide additional levels of functionality for any system while adding substantial degrees of freedom and functionality. Microfluidics structures can replace MEMS in many aspects of reconfigurable electronics, as they feature a much lower cost, a good high-power handling capability, excellent flexibility, and a wider tunable range in many cases.

1. Based on dielectric liquids

   Similar to the microfluidics sensing components, a variety of novel tunable microwave passive components, including antennas, transmission lines, low pass filters based on transmission lines, and resonator-based bandstop filters, are realized with dielectric liquid in the microfluidic channel.

2. Based on liquid metal alloy (LMA)

   a. Reconfigurability based on origami scaffolding and mechanical folding

   For the first time, origami scaffolding structures with Voronoi textures are integrated with the antennas to enable the mechanical compression and stretching

of the antenna; thus the operation (e.g., radiation pattern) changes with the folding.

b. Reconfigurability based on filling volume

   For the first time, the operation of the antenna (e.g., directivity) is controlled by the volume of LMA.

c. Integration of multiple 3D antennas on one "tree"

   Utilizing microfluidics channel, multiple 3D antennas are integrated together and switched by LMA to minimize the interference for the first time.

7.2 Publications and Patents

During four years and eight months' study, I have published 11 papers (three papers as the first author) in top-tier electrical and general-topic journals, 20 papers (11 papers as the first author) in top-tier microwave/sensor conferences, one book chapter, and three patents / provisional patents.

7.2.1 Refereed Journals

J1. Wenjing Su and Manos M. Tentzeris, "Smart Test Strips: Inkjet-printed Paper Microfluidics RFID-based Platforms for Next-Generation Wireless Comprehensive Fluidic Sensing," *IEEE Transactions on Industrial Electronics (TIE)*, 64, no. 9 (2017): 7359-7367.

J2. Wenjing Su, Benjamin S. Cook, Yunnan Fang and Manos M. Tentzeris, "Fully inkjet-printed microfluidics: a solution to low-cost rapid three-dimensional microfluidics fabrication with numerous electrical and sensing applications," *Scientific Reports*, 6 (2016): 35111.

J3. Wenjing Su, Benjamin S. Cook and Manos M. Tentzeris, "Additively Manufactured Microfluidics-Based "Peel-and-Replace RF Sensors for Wearable Applications," *IEEE*

Transactions on Microwave Theory and Techniques (TMTT), vol. 64, no. 6, pp. 1928-1936, June 2016.

J4. Syed Abdullah Nauroze, Jimmy Hester, Bijan Tehrani, Wenjing Su, Jo Bito, Ryan Bahr, John Kimionis, Manos Tentzeris, "Additive Manufactured RF Components and Modules: Towards Empowering the Birth of Cost-efficient Dense and Ubiquitous IoT Implementations," *Proceedings of the IEEE*, 105 (4), 702-722, invited.

J5. Yunnan Fang, Jimmy Hester, Wenjing Su, Justin H. Chow, Suresh K. Sitaraman, and Manos M. Tentzeris, "A bio-enabled maximally mild layer-by-layer Kapton surface modification approach for the fabrication of all-inkjet-printed flexible electronic devices," *Scientific Reports*, 6 (2016): 39909.

J6. Jimmy Hester, Sangkil Kim, Jo Bito, Taoran Le, John Kimionis, Daniel Revier, Christy Saintsing, Wenjing Su, Bijan Tehrani, Anya Traille, Benjamin S Cook, Manos M Tentzeris, "Additively Manufactured Nanotechnology and Origami-Enabled Flexible Microwave Electronics," *Proceedings of the IEEE*, 103, no. 4 (2015): 583-606, invited.

J7. Kenyu Ling, Wenjing Su, Minyeong Yoo, Kyeongseob Kim, Benjamin Cook, Manos M. Tentzeris, and Sungjoon Lim, "Microfluidic Tunable Inkjet-Printed Metamaterial Absorber on Paper," *Optics Express*, vol. 23, Issue 1, pp. 110-120 (2015).

J8. Sungjin Choi, Wenjing Su, Manos M. Tentzeris and Sungjoon Lim, "A Novel Fluid-Reconfigurable Advanced- and Delayed-Phase Line Using Inkjet-printed Microfluidic Composite Right/Left-handed Transmission Line," *IEEE Microwave and Wireless Components Letter (MWCL)*, vol. 25, Issue 2, pp.142-144 (2015).

J9. Chiara Mariotti, Wenjing Su, Benjamin S. Cook, James R. Cooper, Luca Roselli and Manos M. Tentzeris, "Development of Low Cost, Wireless, Inkjet Printed Microfluidic RF Systems and Devices for Sensing or Tunable Electronics," *IEEE Sensors*

Journal, vol no.99, pp.1,1 (2014).

7.2.2 Refereed Conference Proceedings

C1. Wenjing Su, Shicong Wang, Ryan Bahr, and Manos M. Tentzeris, "Smart Floating Balls: 3D Printed Spherical Antennas and Sensors for Water Quality Monitoring", *IEEE International Microwave Symposium (IMS)*, Philadelphia, Pennsylvania, 2018

C2. Wenjing Su, Ryan Bahr, Syed Abdullah Nauroze, and Manos M. Tentzeris,"Novel 3D-Printed "Chinese Fan" Bow-Tie Antennas for Origami/Shape-Changing Configurations", *IEEE Symposium on Antennas and Propagation (APS)*, San Diego, California, 2017

C3. Wenjing Su, Ryan Bahr, Syed Abdullah Nauroze, and Manos M. Tentzeris, "Novel 3D printed Liquid-metal-alloy microfluidics-based zigzag and helical Antennas for Origami Reconfigurable Antenna "Trees"", *IEEE International Microwave Symposium (IMS)*, Honolulu, Hawaii, 2017

C4. Wenjing Su, Zihan Wu, Yunnan Fang, Ryan Bahr, Markondeya Raj Pulugurtha, Rao Tummala, and Manos M. Tentzeris, "3D Printed Wearable Flexible SIW and Microfluidics Sensors for Internet of Things and Smart Health Applications," *International Microwave Symposium (IMS)*, Honolulu, Hawaii, 2017

C5. Wenjing Su, Ryan Bahr, Syed Abdullah Nauroze, Manos M. Tentzeris, "3D Printed Reconfigurable Helical Antenna Based on Microfluidics and Liquid Metal Alloy," *IEEE International Antenna and Propagation Symposium (APS)*, Fajardo, Puerto Rico, 2016

C6. Wenjing Su, Qi Liu, Benjamin S. Cook, Manos M. Tentzeris, "All-inkjet-printed Microfluidics-based Encodable Flexible Chipless RFID Sensors," *IEEE International Microwave Symposium (IMS)*, San Francisco, USA, 2016

C7. Wenjing Su, Chiara Mariotti, James R. Cooper, Benjamin S. Cook, Luca Roselli and Manos M. Tentzeris, "Inkjet-Printed Dual Microfluidic-Based Sensor Integrated System," *The IEEE Sensors*, Busan, Korea, 2015

C8. Wenjing Su, Benjamin S. Cook, James R. Cooper and Manos M. Tentzeris, "Low-cost Flexible All-inkjet-printed Microfluidic Sensor," *The 19th International Conference on Miniaturized Systems for Chemistry and Life Sciences (uTAS)*, Gyeongju, Korea, 2015

C9. Wenjing Su, Benjamin S. Cook and Manos M. Tentzeris, "Low-Cost Microfluidics-Enabled Tunable Loop Antenna Using Inkjet-Printing Technologies," *IEEE European Conference on Antennas and Propagation (EuCAP)*, Lisbon, Portugal, 2015

C10. Wenjing Su, Chiara Mariotti, Benjamin S. Cook, Sunjoon Lim, Luca Roselli and Manos M. Tentzeris, "A Metamaterial-Inspired Temperature Stable Inkjet-Printed Microfluidic-Tunable Bandstop Filter," *European Microwave Conference (EuMC)*, Roman, Italy, 2014

C11. Wenjing Su, Chiara Mariotti, Benjamin S. Cook, Luca Roselli and Manos M. Tentzeris, "A Novel Inkjet-Printed Microfluidic Tunable Coplanar Patch Antenna," *IEEE International Antenna and Propagation Symposium (APS)*, Memphis, USA, 2014

C12. Tong-Hong Lin, Wenjing Su, and Manos M. Tentzeris, "Expand Horizons of Microfluidic Systems: An Inkjet Printed Flexible Energy Autonomous Micropump System for Wearable and IoT Microfluidic Applications," *IEEE International Microwave Symposium (IMS)*, Philadelphia, Pennsylvania, 2018

C13. Ryan Bahr, Abdullah Nauroze, Wenjing Su, and M. M. Tentzeris, "Self-Actuating 3D Printed Packaging for Deployable Antennas," *IEEE Electronic Components and Technology Conference (ECTC) (67th)*, pp. 1425-1430. IEEE, 2017.

C14. Jo Bito, Ryan Bahr, Jimmy Hester, John Kimionis, Abdullah Nauroze, Wenjing Su, Bijan Tehrani, and Manos M. Tentzeris, "Inkjet-/3D-/4D-Printed Autonomous Wearable RF Modules for Biomonitoring, Positioning and Sensing Applications," *SPIE Defense+ Security*, pp. 101940Z-101940Z. International Society for Optics and Photonics, 2017, invited

C15. Syed Abdullah Nauroze, Bijan Tehrani, Wenjing Su, Ryan Bahr, Manos Tentzeris, "An Inkjet-printed Tunable Origami Frequency Selective Surface on Cellulose Paper," *IEEE Symposium on Antennas and Propagation (APS)*, 2017

C16. Bijan Tehrani, Ryan Bahr, Wenjing Su, Benjamin S. Cook and Manos M. Tentzeris, "E-Band Characterization of 3D-Printed Dielectrics for Fully-Printed Millimeter-Wave Wireless System Packaging," *IEEE International Microwave Symposium (IMS)*, 2017

C17. Ryan Bahr, Yunnan Fang, Wenjing Su, Bijan Tehrani and Manos M. Tentzeris, "Novel Uniquely 3D Printed Intricate Voronoi and Fractal 3D Antennas," *IEEE International Microwave Symposium (IMS)*, 2017

C18. Syed Abdullah Nauroze, Jimmy Hester, Wenjing Su, and Manos M. Tentzeris, "Inkjet-printed substrate integrated waveguides (SIW) with "drill-less" vias on paper substrates," *IEEE International Microwave Symposium (IMS)*, San Francisco, USA, 2016

C19. Syed Abdullah Nauroze, John Kimionis, Jo Bito, Wenjing Su, Jimmy G. Hester, Kunal Nate, Bijan Tehrani and Manos M. Tentzeris, "Additive manufacturing technologies for near-and far-field energy harvesting applications," *IEEE Radio and Wireless Symposium (RWS)*, Austin, Texas, 2016

C20. Kenyu Ling, Minyeong Yoo, Kyeongseob Kim, Sungjoon Lim, Wenjing Su, Benjamin Cook, and Manos M. Tentzeris, "Microfluidically tunable paper-based inkjet-printed metamaterial absorber," *International Workshop on Antenna Technology (iWAT)*,

pp. 218-220. IEEE, 2015.

7.2.3 Book Chapter

B1. Bijan K Tehrani, Jo Bito, Jimmy G. Hester, Wenjing Su, Ryan A. Bahr, Benjamin S. Cook, and Manos M. Tentzeris, "Advanced Antenna Fabrication Processes (MEMS/ LTCC/LCP/Printing)," *Handbook of Antenna Technologies (Springer)*, 2015

7.2.4 Patents

P1. Wenjing Su and Manos M. Tentzeris, "Smart test strip platform enabled by fully inkjet-printed microfluidics and Radio-Frequency Identification (RFID) technique," U.S. Patent Application No. 62/487,076, pending

P2. Wenjing Su, Manos M. Tentzeris, "Liquid metal reconfigurable antenna," U.S. Patent Application No. 62/516,293, pending

P3. Wenjing Su, Jiang Zhu, Huan Liao, "Planar RF antenna with duplicated unit cells," U.S. Patent Application No. 15/820,610

REFERENCES

[1] G. M. Whitesides, "The origins and the future of microfluidics," *Nature*, vol. 442, no. 7101, pp. 368–373, 2006.

[2] C. Rivet, H. Lee, A. Hirsch, S. Hamilton, and H. Lu, "Microfluidics for medical diagnostics and biosensors," *Chemical Engineering Science*, vol. 66, no. 7, pp. 1490–1507, 2011.

[3] M. Mehling and S. Tay, "Microfluidic cell culture," *Current opinion in Biotechnology*, vol. 25, pp. 95–102, 2014.

[4] G. Velve-Casquillas, M. L. Berre, M. Piel, and P. T. Tran, "Microfluidic tools for cell biological research," *Nano Today*, vol. 5, no. 1, pp. 28 –47, 2010.

[5] C. Kleinstreuer, J. Li, and J. Koo, "Microfluidics of nano-drug delivery," *International Journal of Heat and Mass Transfer*, vol. 51, no. 23, pp. 5590–5597, 2008.

[6] Y. Song, J. Hormes, and C. S. Kumar, "Microfluidic synthesis of nanomaterials," *Small*, vol. 4, no. 6, pp. 698–711, 2008.

[7] S.-J. Shin, J.-Y. Park, J.-Y. Lee, H. Park, Y.-D. Park, K.-B. Lee, C.-M. Whang, and S.-H. Lee, "on the flyi continuous generation of alginate fibers using a microfluidic device," *Langmuir*, vol. 23, no. 17, pp. 9104–9108, 2007.

[8] D. Psaltis, S. R. Quake, and C. Yang, "Developing optofluidic technology through the fusion of microfluidics and optics," *Nature*, vol. 442, no. 7101, pp. 381–386, 2006.

[9] G. Akerlof, "Dielectric constants of some organic solvent-water mixtures at various temperatures," *Journal of the American Chemical Society*, vol. 54, no. 11, pp. 4125–4139, 1932.

[10] R Behrends, K Fuchs, U Kaatze, Y Hayashi, and Y Feldman, "Dielectric properties of glycerol/water mixtures at temperatures between 10 and 50 C," *The Journal of chemical physics*, vol. 124, no. 14, p. 144 512, 2006.

[11] R. Somaraju and J. Trumpf, "Frequency, temperature and salinity variation of the permittivity of seawater," *IEEE Transactions on Antennas and Propagation*, vol. 54, no. 11, pp. 3441–3448, 2006.

[12] W. Guo, X. Zhu, H. Liu, R. Yue, and S. Wang, "Effects of milk concentration and freshness on microwave dielectric properties," *Journal of Food Engineering*, vol. 99, no. 3, pp. 344–350, 2010.

[13] A Garcia, J. Torres, M De Blas, A De Francisco, and R Illanes, "Dielectric characteristics of grape juice and wine," *Biosystems engineering*, vol. 88, no. 3, pp. 343–349, 2004.

[14] M. Arshad, J. Cheema, and S. Ahmed, "Determination of lithology and groundwater quality using electrical resistivity survey," *International Journal of Agriculture and Biology*, vol. 9, no. 1, pp. 143–146, 2007.

[15] A Catenaccio, Y Daruich, and C Magallanes, "Temperature dependence of the permittivity of water," *Chemical physics letters*, vol. 367, no. 5, pp. 669–671, 2003.

[16] P Petong, R Pottel, and U Kaatze, "Dielectric relaxation of h-bonded liquids. mixtures of ethanol and n-hexanol at different compositions and temperatures," *The Journal of Physical Chemistry A*, vol. 103, no. 31, pp. 6114–6121, 1999.

[17] R. Nigmatullin, M. A.-G. Jafar, N. Shinyashiki, S. Sudo, and S. Yagihara, "Recognition of a new permittivity function for glycerol by the use of the eigen-coordinates method," *Journal of Non-Crystalline Solids*, vol. 305, pp. 96 –111, 2002.

[18] K. Shibata, "Measurement of complex permittivity for liquid materials using the open-ended cut-off waveguide reflection method," in *Microwave Conference Proceedings (CJMW), 2011 China-Japan Joint*, Apr. 2011, pp. 1–4.

[19] V Komarov, S Wang, and J Tang, "Permittivity and measurements," *Encyclopedia of RF and microwave engineering*, 2005.

[20] K. Grenier, D. Dubuc, P.-E. Poleni, M. Kumemura, H. Toshiyoshi, T. Fujii, and H. Fujita, "Integrated broadband microwave and microfluidic sensor dedicated to bioengineering," *IEEE Transactions on microwave theory and techniques*, vol. 57, no. 12, p. 3246, 2009.

[21] S. Liu, I. Ocket, M. Cauwe, D. Schreurs, and B. Nauwelaers, "Sensitivity analysis of broadband on-wafer dielectric spectroscopy of yeast cell suspensions up to 110 ghz," *IEEE Microwave and Wireless Components Letters*, vol. 25, no. 3, pp. 199–201, 2015.

[22] G. Gennarelli, S. Romeo, M. R. Scarfì, and F. Soldovieri, "A microwave resonant sensor for concentration measurements of liquid solutions," *IEEE Sensors Journal*, vol. 13, no. 5, pp. 1857–1864, 2013.

[23] B. Kapilevich and B. Litvak, "Optimized microwave sensor for online concentration measurements of binary liquid mixtures," *IEEE Sensors Journal*, vol. 11, no. 10, pp. 2611–2616, 2011.

[24] H.-J. Lee, H.-S. Lee, K.-H. Yoo, and J.-G. Yook, "DNA sensing using split-ring resonator alone at microwave regime," *Journal of Applied Physics*, vol. 108, no. 1, p. 014 908, 2010.

[25] T. Chretiennot, D. Dubuc, and K. Grenier, "Double stub resonant biosensor for glucose concentrations quantification of multiple aqueous solutions," in *2014 IEEE MTT-S International Microwave Symposium (IMS2014)*, IEEE, 2014, pp. 1–4.

[26] G. M. Rebeiz, *RF MEMS: Theory, design, and technology*. John Wiley & Sons, 2004.

[27] B. A. Cetiner, H. Jafarkhani, J.-Y. Qian, H. J. Yoo, A. Grau, and F. De Flaviis, "Multifunctional reconfigurable MEMS integrated antennas for adaptive mimo systems," *IEEE Communications Magazine*, vol. 42, no. 12, pp. 62–70, 2004.

[28] D. Ramachandran, A. Oz, V. K. Saraf, G. K. Fedder, and T. Mukherjee, "MEMS-enabled reconfigurable vco and rf filter," in *Radio Frequency Integrated Circuits (RFIC) Symposium, 2004. Digest of Papers. 2004 IEEE*, IEEE, 2004, pp. 251–254.

[29] J. Gianvittorio, J Zendejas, Y Rahmat-Samii, and J Judy, "Reconfigurable MEMS-enabled frequency selective surfaces," *Electronics Letters*, vol. 38, no. 25, pp. 1627–1628, 2002.

[30] K. Entesari and A. P. Saghati, "Fluidics in microwave components," *IEEE Microwave Magazine*, vol. 17, no. 6, pp. 50–75, 2016.

[31] M. D. Dickey, R. C. Chiechi, R. J. Larsen, E. A. Weiss, D. A. Weitz, and G. M. Whitesides, "Eutectic gallium-indium (EGaIn): A liquid metal alloy for the formation of stable structures in microchannels at room temperature," *Advanced Functional Materials*, vol. 18, no. 7, pp. 1097–1104, 2008.

[32] S. Cheng, A. Rydberg, K. Hjort, and Z. Wu, "Liquid metal stretchable unbalanced loop antenna," *Applied Physics Letters*, vol. 94, no. 14, p. 144 103, 2009.

[33] J.-H. So, J. Thelen, A. Qusba, G. J. Hayes, G. Lazzi, and M. D. Dickey, "Reversibly deformable and mechanically tunable fluidic antennas," *Advanced Functional Materials*, vol. 19, no. 22, pp. 3632–3637, 2009.

[34] G. J. Hayes, J.-H. So, A. Qusba, M. D. Dickey, and G. Lazzi, "Flexible liquid metal alloy (EGaIn) microstrip patch antenna," *IEEE Transactions on Antennas and Propagation*, vol. 60, no. 5, pp. 2151–2156, 2012.

[35] A. Dey, R. Guldiken, and G. Mumcu, "Wideband frequency tunable liquid metal monopole antenna," in *Antennas and Propagation Society International Symposium (APSURSI), 2013 IEEE*, IEEE, 2013, pp. 392–393.

[36] A. P. Saghati, J. S. Batra, J. Kameoka, and K. Entesari, "A miniaturized microfluidically reconfigurable coplanar waveguide bandpass filter with maximum power handling of 10 watts," *IEEE Transactions on Microwave Theory and Techniques*, vol. 63, no. 8, pp. 2515–2525, 2015.

[37] G. Mumcu, A. Dey, and T. Palomo, "Frequency-agile bandpass filters using liquid metal tunable broadside coupled split ring resonators," *IEEE Microwave and Wireless Components Letters*, vol. 23, no. 4, pp. 187–189, 2013.

[38] J. D. Barrera and G. H. Huff, "A fluidic loading mechanism in a polarization reconfigurable antenna with a comparison to solid state approaches," *IEEE Transactions on Antennas and Propagation*, vol. 62, no. 8, pp. 4008–4014, 2014.

[39] A. A. Gheethan, A. Dey, and G. Mumcu, "Passive feed network designs for microfluidic beam-scanning focal plane arrays and their performance evaluation," *IEEE Transactions on Antennas and Propagation*, vol. 63, no. 8, pp. 3452–3464, 2015.

[40] T. Bhattacharjee, H. Jiang, and N. Behdad, "A fluidically tunable, dual-band patch antenna with closely spaced bands of operation," *IEEE Antennas and Wireless Propagation Letters*, vol. 15, pp. 118–121, 2016.

[41] H Bikas, P Stavropoulos, and G Chryssolouris, "Additive manufacturing methods and modelling approaches: A critical review," *The International Journal of Advanced Manufacturing Technology*, vol. 83, no. 1-4, pp. 389–405, 2016.

[42] A. Woesz, "Rapid prototyping to produce porous scaffolds with controlled architecture for possible use in bone tissue engineering," in *Virtual Prototyping & Bio Manufacturing in Medical Applications*, Springer, 2008, pp. 171–206.

[43] E. Tekin, P. J. Smith, and U. S. Schubert, "Inkjet printing as a deposition and patterning tool for polymers and inorganic particles," *Soft Matter*, vol. 4, no. 4, pp. 703–713, 2008.

[44] A. C. Arias, J. D. MacKenzie, I. McCulloch, J. Rivnay, and A. Salleo, "Materials and applications for large area electronics: Solution-based approaches," *Chemical reviews*, vol. 110, no. 1, pp. 3–24, 2010.

[45] B.-J. de Gans, P. C. Duineveld, and U. S. Schubert, "Inkjet printing of polymers: State of the art and future developments," *Advanced materials*, vol. 16, no. 3, pp. 203–213, 2004.

[46] J. Perelaer, P. J. Smith, E. van den Bosch, S. S. van Grootel, P. H. Ketelaars, and U. S. Schubert, "The spreading of inkjet-printed droplets with varying polymer molar mass on a dry solid substrate," *Macromolecular chemistry and physics*, vol. 210, no. 6, pp. 495–502, 2009.

[47] M. Singh, H. M. Haverinen, P. Dhagat, and G. E. Jabbour, "Inkjet printingprocess and its applications," *Advanced materials*, vol. 22, no. 6, pp. 673–685, 2010.

[48] Z. Zhang, X. Zhang, Z. Xin, M. Deng, Y. Wen, and Y. Song, "Controlled inkjetting of a conductive pattern of silver nanoparticles based on the coffee-ring effect," *Advanced Materials*, vol. 25, no. 46, pp. 6714–6718, 2013.

[49] A. Kamyshny and S. Magdassi, "Conductive nanomaterials for printed electronics," *Small*, vol. 10, no. 17, pp. 3515–3535, 2014.

[50] E. B. Secor, P. L. Prabhumirashi, K. Puntambekar, M. L. Geier, and M. C. Hersam, "Inkjet printing of high conductivity, flexible graphene patterns," *The journal of physical chemistry letters*, vol. 4, no. 8, pp. 1347–1351, 2013.

[51] A. Teichler, J. Perelaer, and U. S. Schubert, "Inkjet printing of organic electronics–comparison of deposition techniques and state-of-the-art developments," *Journal of Materials Chemistry C*, vol. 1, no. 10, pp. 1910–1925, 2013.

[52] *Printed wiring board fabrication*, [online]http://slideplayer.com/slide/1554599/.

[53] *Nano- and microscale fabrication and characterization*, UC Santa Cruz, https://cleanroom.soe.ucsc.edu/lithography.

[54] J. G. Hester, S. Kim, J. Bito, T. Le, J. Kimionis, D. Revier, C. Saintsing, W. Su, B. Tehrani, A. Traille, *et al.*, "Additively manufactured nanotechnology and origami-enabled flexible microwave electronics," *Proceedings of the IEEE*, vol. 103, no. 4, pp. 583–606, 2015.

[55] S. H. Ko, H. Pan, C. P. Grigoropoulos, C. K. Luscombe, J. M. Fréchet, and D. Poulikakos, "All-inkjet-printed flexible electronics fabrication on a polymer substrate by low-temperature high-resolution selective laser sintering of metal nanoparticles," *Nanotechnology*, vol. 18, no. 34, p. 345 202, 2007.

[56] P. Calvert, "Inkjet printing for materials and devices," *Chemistry of materials*, vol. 13, no. 10, pp. 3299–3305, 2001.

[57] G. T. Kovacs, *Micromachined transducers sourcebook*. WCB/McGraw-Hill New York, NY, 1998.

[58] G. Jenkins, Y. Wang, Y. L. Xie, Q. Wu, W. Huang, L. Wang, and X. Yang, "Printed electronics integrated with paper-based microfluidics: New methodologies for next-generation health care," *Microfluidics and Nanofluidics*, vol. 19, no. 2, pp. 251–261, 2015.

[59] A. W. Martinez, S. T. Phillips, G. M. Whitesides, and E. Carrilho, "Diagnostics for the developing world: Microfluidic paper-based analytical devices," *Analytical chemistry*, vol. 82, no. 1, pp. 3–10, 2009.

[60] D. C. Duffy, J. C. McDonald, O. J. Schueller, and G. M. Whitesides, "Rapid prototyping of microfluidic systems in poly (dimethylsiloxane)," *Analytical chemistry*, vol. 70, no. 23, pp. 4974–4984, 1998.

[61] G. M. Whitesides and A. D. Stroock, "Flexible methods for microfluidics," *Physics Today*, vol. 54, no. 6, pp. 42–48, 2001.

[62] A. Waldbaur, H. Rapp, K. Länge, and B. E. Rapp, "Let there be chip–towards rapid prototyping of microfluidic devices: One-step manufacturing processes," *Analytical Methods*, vol. 3, no. 12, pp. 2681–2716, 2011.

[63] A. W. Martinez, S. T. Phillips, M. J. Butte, and G. M. Whitesides, "Patterned paper as a platform for inexpensive, low-volume, portable bioassays," *Angewandte Chemie International Edition*, vol. 46, no. 8, pp. 1318–1320, 2007.

[64] K. Abe, K. Suzuki, and D. Citterio, "Inkjet-printed microfluidic multianalyte chemical sensing paper," *Analytical chemistry*, vol. 80, no. 18, pp. 6928–6934, 2008.

[65] A. K. Yetisen, M. S. Akram, and C. R. Lowe, "Paper-based microfluidic point-of-care diagnostic devices," *Lab on a Chip*, vol. 13, no. 12, pp. 2210–2251, 2013.

[66] Y. Yang, E. Noviana, M. P. Nguyen, B. J. Geiss, D. S. Dandy, and C. S. Henry, "Paper-based microfluidic devices: Emerging themes and applications," *Analytical Chemistry*, 2016.

[67] E. Carrilho, A. W. Martinez, and G. M. Whitesides, "Understanding wax printing: A simple micropatterning process for paper-based microfluidics," *Analytical chemistry*, vol. 81, no. 16, pp. 7091–7095, 2009.

[68] Y. Xia, J. Si, and Z. Li, "Fabrication techniques for microfluidic paper-based analytical devices and their applications for biological testing: A review," *Biosensors and Bioelectronics*, vol. 77, pp. 774–789, 2016.

[69] J. C. McDonald, M. L. Chabinyc, S. J. Metallo, J. R. Anderson, A. D. Stroock, and G. M. Whitesides, "Prototyping of microfluidic devices in poly (dimethylsiloxane)

using solid-object printing," *Analytical chemistry*, vol. 74, no. 7, pp. 1537–1545, 2002.

[70] B. C. Gross, J. L. Erkal, S. Y. Lockwood, C. Chen, and D. M. Spence, "Evaluation of 3d printing and its potential impact on biotechnology and the chemical sciences," *Analytical chemistry*, vol. 86, no. 7, pp. 3240–3253, 2014.

[71] J. L. Erkal, A. Selimovic, B. C. Gross, S. Y. Lockwood, E. L. Walton, S. McNamara, R. S. Martin, and D. M. Spence, "3d printed microfluidic devices with integrated versatile and reusable electrodes," *Lab on a Chip*, vol. 14, no. 12, pp. 2023–2032, 2014.

[72] S. Waheed, J. M. Cabot, N. P. Macdonald, T. Lewis, R. M. Guijt, B. Paull, and M. C. Breadmore, "3d printed microfluidic devices: Enablers and barriers," *Lab on a Chip*, 2016.

[73] P. O'Neill, A. B. Azouz, M. Vazquez, J. Liu, S. Marczak, Z. Slouka, H. C. Chang, D. Diamond, and D. Brabazon, "Advances in three-dimensional rapid prototyping of microfluidic devices for biological applications," *Biomicrofluidics*, vol. 8, no. 5, p. 052 112, 2014.

[74] M. K. Gelber and R. Bhargava, "Monolithic multilayer microfluidics via sacrificial molding of 3d-printed isomalt," *Lab on a Chip*, vol. 15, no. 7, pp. 1736–1741, 2015.

[75] A. I. Shallan, P. Smejkal, M. Corban, R. M. Guijt, and M. C. Breadmore, "Cost-effective three-dimensional printing of visibly transparent microchips within minutes," *Analytical chemistry*, vol. 86, no. 6, pp. 3124–3130, 2014.

[76] A. J. Morgan, L. H. San Jose, W. D. Jamieson, J. M. Wymant, B. Song, P. Stephens, D. A. Barrow, and O. K. Castell, "Simple and versatile 3d printed microfluidics using fused filament fabrication," *PloS one*, vol. 11, no. 4, e0152023, 2016.

[77] A. K. Au, N. Bhattacharjee, L. F. Horowitz, T. C. Chang, and A. Folch, "3D-printed microfluidic automation," *Lab on a chip*, vol. 15, no. 8, pp. 1934–1941, 2015.

[78] R. Sochol, E Sweet, C. Glick, S Venkatesh, A Avetisyan, K. Ekman, A Raulinaitis, A Tsai, A Wienkers, K Korner, *et al.*, "3D printed microfluidic circuitry via multijet-based additive manufacturing," *Lab on a Chip*, vol. 16, no. 4, pp. 668–678, 2016.

[79] A. K. Au, W. Lee, and A. Folch, "Mail-order microfluidics: Evaluation of stereolithography for the production of microfluidic devices," *Lab on a chip*, vol. 14, no. 7, pp. 1294–1301, 2014.

[80] K. Abe, K. Suzuki, and D. Citterio, "Inkjet-printed microfluidic multianalyte chemical sensing paper," *Analytical chemistry*, vol. 80, no. 18, pp. 6928–6934, 2008.

[81] A. W. Martinez, S. T. Phillips, and G. M. Whitesides, "Three-dimensional microfluidic devices fabricated in layered paper and tape," *Proceedings of the National Academy of Sciences*, vol. 105, no. 50, pp. 19 606–19 611, 2008.

[82] W. Wang, S. Zhao, and T. Pan, "Lab-on-a-print: From a single polymer film to three-dimensional integrated microfluidics," *Lab on a Chip*, vol. 9, no. 8, pp. 1133–1137, 2009.

[83] A. Bonyár, H. Sántha, M. Varga, B. Ring, A. Vitéz, and G. Harsányi, "Characterization of rapid pdms casting technique utilizing molding forms fabricated by 3d rapid prototyping technology (rpt)," *International Journal of Material Forming*, vol. 7, no. 2, pp. 189–196, 2014.

[84] E. M. Hamad, S. E. Bilatto, N. Y. Adly, D. Correa, B. Wolfrum, M. J. Schoening, A. Offenhäusser, and A. Yakushenko, "Inkjet printing of uv-curable adhesive and dielectric inks for microfluidic devices," *Lab on a Chip*, vol. 16, no. 1, pp. 70–74, 2016.

[85] G. V. Kaigala, S. Ho, R. Penterman, and C. J. Backhouse, "Rapid prototyping of microfluidic devices with a wax printer," *Lab on a Chip*, vol. 7, no. 3, pp. 384–387, 2007.

[86] K. A. Chan, X. Niu, A. J. de Mello, and S. G. Kazarian, "Rapid prototyping of microfluidic devices for integrating with ft-ir spectroscopic imaging," *Lab on a Chip*, vol. 10, no. 16, pp. 2170–2174, 2010.

[87] *SU-8 2000*, Microchem, www.microchem.com/pdf/SU-82000DataSheet2000_5thru2015Ver4.pdf.

[88] W. Su, B. Cook, M. Tentzeris, C. Mariotti, and L. Roselli, "A novel inkjet-printed microfluidic tunable coplanar patch antenna," in *IEEE Antennas and Propagation Society International Symposium (APSURSI)*, IEEE, 2014, pp. 858–859.

[89] W Su, C Mariotti, B. Cook, S Lim, L Roselli, and M. Tentzeris, "A metamaterial-inspired temperature stable inkjet-printed microfluidic-tunable bandstop filter," in *European Microwave Conference (EuMC), 2014 44th*, IEEE, 2014, pp. 9–12.

[90] W. Su, B. Cook, and M. M. Tentzeris, "A low-cost inkjet-printed microfluidics-based tunable loop antenna feed by microfluidics-based tunable balun," in *The 9th European Conference on Antennas and Propagation (EuCAP 2015) (EuCAP 2015)*, Lisbon, Portugal, Apr. 2015.

[91] W. Su, J. Cooper, B. Cook, M. Tentzeris, C. Mariotti, and L. Roselli, "Inkjet-printed dual microfluidic-based sensor integrated system," in *IEEE SENSORS*, Nov. 2015, pp. 1–3.

[92] B. S. Cook, J. R. Cooper, and M. M. Tentzeris, "An inkjet-printed microfluidic RFID-enabled platform for wireless lab-on-chip applications," *IEEE Transactions on Microwave Theory and Techniques*, vol. 61, no. 12, pp. 4714–4723, 2013.

[93] P. Abgrall, V. Conedera, H. Camon, A.-M. Gue, and N.-T. Nguyen, "Su-8 as a structural material for labs-on-chips and microelectromechanical systems," *ELECTROPHORESIS*, vol. 28, no. 24, pp. 4539–4551, 2007.

[94] B. A. Weisenberg and D. L. Mooradian, "Hemocompatibility of materials used in microelectromechanical systems: Platelet adhesion and morphology in vitro," *Journal of biomedical materials research*, vol. 60, no. 2, pp. 283–291, 2002.

[95] M.-H. Wu, H. Cai, X. Xu, J. P. Urban, Z.-F. Cui, and Z. Cui, "A su-8/pdms hybrid microfluidic device with integrated optical fibers for online monitoring of lactate," *Biomedical Microdevices*, vol. 7, no. 4, pp. 323–329, 2005.

[96] S. Kim, B. Cook, T. Le, J. Cooper, H. Lee, V. Lakafosis, R. Vyas, R. Moro, M. Bozzi, A. Georgiadis, *et al.*, "Inkjet-printed antennas, sensors and circuits on paper substrate," *IET Microwaves, Antennas & Propagation*, vol. 7, no. 10, pp. 858–868, 2013.

[97] J. Lessing, A. C. Glavan, S. B. Walker, C. Keplinger, J. A. Lewis, and G. M. Whitesides, "Inkjet printing of conductive inks with high lateral resolution on omniphobic "rf paper" for paper-based electronics and mems," *Advanced Materials*, vol. 26, no. 27, pp. 4677–4682, 2014.

[98] H. Lee, B. S. Cook, K. Murali, M. Raj, and M. M. Tentzeris, "Inkjet printed high-Q RF inductors on paper substrate with ferromagnetic nanomaterial," *IEEE Microwave and Wireless Components Letters*, vol. 26, no. 6, pp. 419–421, 2016.

[99] S. A. Nauroze, J. G. Hester, B. K. Tehrani, W. Su, J. Bito, R. Bahr, J. Kimionis, and M. M. Tentzeris, "Additively manufactured rf components and modules: Toward empowering the birth of cost-efficient dense and ubiquitous IoT implementations," *Proceedings of the IEEE*, 2017.

[100] S. A. Nauroze, J. Hester, W. Su, and M. M. Tentzeris, "Inkjet-printed substrate integrated waveguides (siw) with "drill-less" vias on paper substrates," in *Microwave Symposium (IMS), 2016 IEEE MTT-S International*, IEEE, 2016, pp. 1–4.

[101] A. W. Martinez, S. T. Phillips, E. Carrilho, S. W. Thomas III, H. Sindi, and G. M. Whitesides, "Simple telemedicine for developing regions: Camera phones and paper-

based microfluidic devices for real-time, off-site diagnosis," *Analytical chemistry*, vol. 80, no. 10, pp. 3699–3707, 2008.

[102] K.-P. Latti, M Kettunen, J.-P. Strom, and P. Silventoinen, "A review of microstrip t-resonator method in determining the dielectric properties of printed circuit board materials," *IEEE Transactions on Instrumentation and Measurement*, vol. 56, no. 5, pp. 1845–1850, 2007.

[103] N. K. Das, S. M. Voda, and D. M. Pozar, "Two methods for the measurement of substrate dielectric constant," *IEEE Transactions on Microwave Theory and Techniques*, vol. 35, no. 7, pp. 636–642, 1987.

[104] L. Yang, A. Rida, R. Vyas, and M. M. Tentzeris, "RFID tag and rf structures on a paper substrate using inkjet-printing technology," *IEEE Transactions on Microwave Theory and Techniques*, vol. 55, no. 12, pp. 2894–2901, 2007.

[105] G. Shaker, S. Safavi-Naeini, N. Sangary, and M. M. Tentzeris, "Inkjet printing of ultrawideband (UWB) antennas on paper-based substrates," *IEEE Antennas and Wireless Propagation Letters*, vol. 10, pp. 111–114, 2011.

[106] I. Gibson, D. W. Rosen, B. Stucker, *et al.*, *Additive manufacturing technologies*. Springer, 2010.

[107] R. Bahr, T. Le, M. M. Tentzeris, S. Moscato, M. Pasian, M. Bozzi, and L. Perregrini, "Rf characterization of 3d printed flexible materials-ninjaflex filaments," in *2015 European Microwave Conference (EuMC)*, IEEE, 2015, pp. 742–745.

[108] W. Su, R. Bahr, S. A. Nauroze, and M. M. Tentzeris, "3d printed reconfigurable helical antenna based on microfluidics and liquid metal alloy," in *IEEE Antennas and Propagation Society International Symposium (APSURSI)*, IEEE, 2016, pp. 1–2.

[109] M. Zandvakili, M. M. Honari, D. Sameoto, and P. Mousavi, "Microfluidic liquid metal based mechanically reconfigurable antenna using reversible gecko adhesive based bonding," in *Microwave Symposium (IMS), 2016 IEEE MTT-S International*, IEEE, 2016, pp. 1–4.

[110] K Li, C. H. Cheng, T Matsui, and M. Izutsu, "Coplanar patch antennas: Principle, simulation and experiment," in *Antennas and Propagation Society International Symposium, 2001. IEEE*, IEEE, vol. 3, 2001, pp. 402–405.

[111] C.-C. Chang, C Caloz, and T Itoh, "Analysis of a compact slot resonator in the ground plane for microstrip structures," in *Asia-Pacific Microwave Conference (APMC)*, IEEE, vol. 3, 2001, pp. 1100–1103.

[112] H. Liu, T Yoshimasu, and L. Sun, "CPW bandstop filter using periodically loaded slot resonators," *Electronics Letters*, vol. 42, no. 6, pp. 352–353, 2006.

[113] W. Su, Z. Wu, Y. Fang, R. Bahr, P. M. Raj, R. Tummala, and M. M. Tentzeris, "3d printed wearable flexible SIW and microfluidics sensors for internet of things and smart health applications," in *Microwave Symposium (IMS), 2017 IEEE MTT-S International*, IEEE, 2017, pp. 1–4.

[114] W. Su, B. S. Cook, and M. M. Tentzeris, "Additively manufactured microfluidics-based "peel-and-replace" RF sensors for wearable applications," *IEEE Transactions on Microwave Theory and Techniques*, vol. 64, no. 6, pp. 1928–1936, 2016.

[115] W. Su, B. S. Cook, Y. Fang, and M. M. Tentzeris, "Fully inkjet-printed microfluidics: A solution to low-cost rapid three-dimensional microfluidics fabrication with numerous electrical and sensing applications," *Scientific Reports*, vol. 6, p. 35 111, 2016.

[116] Z. Nie, C. A. Nijhuis, J. Gong, X. Chen, A. Kumachev, A. W. Martinez, M. Narovlyansky, and G. M. Whitesides, "Electrochemical sensing in paper-based microfluidic devices," *Lab on a Chip*, vol. 10, no. 4, pp. 477–483, 2010.

[117] C. Mariotti, W. Su, B. S. Cook, L. Roselli, and M. M. Tentzeris, "Development of low cost, wireless, inkjet printed microfluidic RF systems and devices for sensing or tunable electronics," *IEEE Sensors Journal*, vol. 15, no. 6, pp. 3156–3163, 2015.

[118] R. Want, "Enabling ubiquitous sensing with rfid," *Computer*, vol. 37, no. 4, pp. 84–86, 2004.

[119] R. Vyas, V. Lakafosis, A. Rida, N. Chaisilwattana, S. Travis, J. Pan, and M. M. Tentzeris, "Paper-based RFID-enabled wireless platforms for sensing applications," *IEEE Transactions on Microwave Theory and Techniques*, vol. 57, no. 5, pp. 1370–1382, 2009.

[120] W. Su, Q. Liu, B. Cook, and M. Tentzeris, "All-inkjet-printed microfluidics-based encodable flexible chipless rfid sensors," in *2016 IEEE MTT-S International Microwave Symposium (IMS)*, May 2016, pp. 1–4.

[121] S. Bouaziz, F. Chebila, A. Traille, P. Pons, H. Aubert, and M. M. Tentzeris, "Novel microfluidic structures for wireless passive temperature telemetry medical systems using radar interrogation techniques in Ka-band," *IEEE Antennas and Wireless Propagation Letters*, vol. 11, pp. 1706–1709, 2012.

[122] M. Li, H. Gou, I. Al-Ogaidi, and N. Wu, "Nanostructured sensors for detection of heavy metals: A review," *ACS Sustainable Chemistry & Engineering*, vol. 1, no. 7, pp. 713–723, 2013.

[123] J. Bartram and R. Ballance, *Water quality monitoring: A practical guide to the design and implementation of freshwater quality studies and monitoring programmes*. CRC Press, 1996.

[124] V. G. Artemov, A. A. Volkov, N. N. Sysoev, and A. A. Volkov, "Conductivity of aqueous hcl, naoh and nacl solutions: Is water just a substrate?" *EPL (Europhysics Letters)*, vol. 109, no. 2, p. 26 002, 2015.

[125] F. Segura-Quijano, J. Sacristán-Riquelme, J. García-Cantón, M. T. Osés, and A. Baldi, "Towards fully integrated wireless impedimetric sensors," *Sensors*, vol. 10, no. 4, pp. 4071–4082, 2010.

[126] A. Jouyban, S. Soltanpour, and H.-K. Chan, "A simple relationship between dielectric constant of mixed solvents with solvent composition and temperature," *International journal of pharmaceutics*, vol. 269, no. 2, pp. 353–360, 2004.

[127] F. Buckley and A. A. Maryott, *Tables of dielectric dispersion data for pure liquids and dilute solutions*. US Dept. of Commerce, National Bureau of Standards, 1958, vol. 589.

[128] A. V. Rukavina, "Hand-held unit for liquid-type recognition, based on interdigital capacitor," *Measurement*, vol. 51, pp. 289–296, 2014.

[129] A. P. Sample, D. J. Yeager, P. S. Powledge, A. V. Mamishev, and J. R. Smith, "Design of an rfid-based battery-free programmable sensing platform," *IEEE Transactions on Instrumentation and Measurement*, vol. 57, no. 11, pp. 2608–2615, 2008.

[130] Z. Qi, Y. Zhuang, X. Li, W. Liu, Y. Du, and B. Wang, "Full passive uhf rfid tag with an ultra-low power, small area, high resolution temperature sensor suitable for environment monitoring," *Microelectronics Journal*, vol. 45, no. 1, pp. 126–131, 2014.

[131] S. Preradovic, I. Balbin, N. C. Karmakar, and G. F. Swiegers, "Multiresonator-based chipless rfid system for low-cost item tracking," *IEEE Transactions on Microwave Theory and Techniques*, vol. 57, no. 5, pp. 1411–1419, 2009.

[132] S. Preradovic and N. C. Karmakar, "Design of fully printable planar chipless rfid transponder with 35-bit data capacity," in *Microwave Conference, 2009. EuMC 2009. European*, IEEE, 2009, pp. 013–016.

[133] D. Girbau, J. Lorenzo, A. Lázaro, C. Ferrater, and R. Villarino, "Frequency-coded chipless rfid tag based on dual-band resonators," *IEEE Antennas and Wireless Propagation Letters*, vol. 11, pp. 126–128, 2012.

[134] L. Yang, R. Zhang, D. Staiculescu, C. Wong, and M. M. Tentzeris, "A novel conformal rfid-enabled module utilizing inkjet-printed antennas and carbon nanotubes for gas-detection applications," *IEEE Antennas and Wireless Propagation Letters*, vol. 8, pp. 653–656, 2009.

[135] S. Druart, D. Flandre, and L. A. Francis, "A self-oscillating system to measure the conductivity and the permittivity of liquids within a single triangular signal," *Journal of Sensors*, vol. 2014, 2014.

[136] M. Schüßler, C. Mandel, M. Maasch, A. Giere, and R. Jakoby, "Phase modulation scheme for chipless rfid-and wireless sensor tags," in *Microwave Conference, 2009. APMC 2009. Asia Pacific*, IEEE, 2009, pp. 229–232.

[137] W. Su and M. M. Tentzeris, "Smart test strips: Next-generation inkjet-printed wireless comprehensive liquid sensing platforms," *IEEE Transactions on Industrial Electronics*, vol. 64, no. 9, pp. 7359–7367, 2017.

[138] W. Su, S. Wang, R. Barh, and M. Tentzeris, "Smart floating balls: 3d printed spherical antennas and sensors for water quality monitoring," in *2018 IEEE MTT-S International Microwave Symposium (IMS)*, May 2018, pp. 1–4.

[139] J. T. Bernhard, "Reconfigurable antennas," *Synthesis lectures on antennas*, vol. 2, no. 1, pp. 1–66, 2007.

[140] X. Liu, S. Yao, S. V. Georgakopoulos, B. S. Cook, and M. M. Tentzeris, "Reconfigurable helical antenna based on an origami structure for wireless communication system," in *2014 IEEE MTT-S International Microwave Symposium (IMS2014)*, IEEE, 2014, pp. 1–4.

[141] J. Kimionis, A. Georgiadis, M. Isakov, H. J. Qi, and M. M. Tentzeris, "3d/inkjet-printed origami antennas for multi-direction rf harvesting," in *2015 IEEE MTT-S International Microwave Symposium*, IEEE, 2015, pp. 1–4.

[142] D. Attali and A. Montanvert, "Computing and simplifying 2D and 3D continuous skeletons," *Computer vision and image understanding*, vol. 67, no. 3, pp. 261–273, 1997.

[143] C. A. Balanis, *Antenna theory: Analysis and design*. John Wiley & Sons, 2005, vol. 1.

[144] C. Lv, D. Krishnaraju, G. Konjevod, H. Yu, and H. Jiang, "Origami based mechanical metamaterials," *Scientific reports*, vol. 4, 2014.

[145] W. Su, S. A. Nauroze, B. Ryan, and M. M. Tentzeris, "Novel 3d printed liquid-metal-alloy microfluidics-based zigzag and helical antennas for origami reconfig-

urable antenna treesi," in *Microwave Symposium (IMS), 2017 IEEE MTT-S International*, IEEE, 2017, pp. 1–4.

[146] W. Su, R. Bahr, S. A. Nauroze, and M. M. Tentzeris, "Novel 3d-printed chinese fani bow-tie antennas for origami/shape-changing configurations," in *Antennas and Propagation & USNC/URSI National Radio Science Meeting, 2017 IEEE International Symposium on*, IEEE, 2017, pp. 1245–1246.